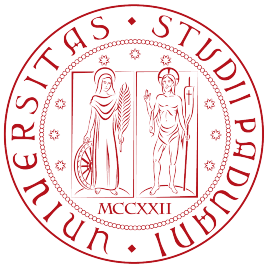

Università degli Studi di Padova

School of Engineering
Department of Industrial Engineering
Master of Science in Aerospace Engineering

SCALING OF HYBRID ROCKET MOTORS WITH SWIRLING OXIDIZER INJECTION

Candidate
Enrico Paccagnella

Advisor
Prof. Daniele Pavarin

Co-advisor
Prof. Arif Karabeyoğlu

Academic Year 2014–2015

Try to comprehend
a little more each day.
Have holy curiosity.
— Albert Einstein

Acknowledgements

I would like to remember all the people who have helped me during the research and the writing of this thesis, with suggestions, criticisms and observations, or only being by my side.

Foremost, I would like to express my sincere gratitude to my advisor Prof. Daniele Pavarin and to my co-advisor Prof. Arif Karabeyoğlu, for their excellent guidance and because without them none of this would have been possible.

I would also like to thank Francesco Barato and Marta Lazzarin, for their continuous support and patience during all the time of my research.

I would like to thank my mother, who always does everything possible to help me and to give me invaluable advices, and during the writing of this thesis even more. I would like to thank my father, who is a precious reference, and I know that he is always there for me. I would also like to thank my brothers, because in their own way, with a bit of good fraternal competition, they have spurred me to get to this point.

I would also like to thank my friends, the old and the new ones, who helped me relaxing and having fun during my thesis period.

Finally, I would like to thank Carlotta, that is always by my side and has constantly encouraged me to do my best, without stopping to believe in me.

Abstract

Hybrid rockets are an attractive alternative to solid and liquid rockets for their unique features, in a world becoming more careful about safety, costs and environmental impact. Hybrid motors show several advantages, like safety, operational reliability, throttling capabilities, environmental friendliness and low costs. Unfortunately hybrid motors suffer also of some disadvantages, the main of which is the low regression rate. International researches are mostly focussed on finding a solution to this issue, to develop a really competitive hybrid rocket. After presenting the hybrid combustion process, that is based on the formation of a turbulent boundary layer, and analysing the Marxman's regression rate theory, several possible methods, proposed to increase the low regression rate, are described.

The present research focuses on the use of a swirling oxidizer injection, in a hybrid motor with a classical cylindrical solid fuel grain with a circular port, i.e. a side burning grain. The conducted study is mainly a numerical analysis, that pays a particular attention on the scaling behaviour of this particular configuration of hybrid rocket motor, in relation to the variation of the geometric swirl number and of the oxidizer mass flux. The obtained results demonstrate that this technology ensures an increase of the regression rate and of the performance of the hybrid motor, compared to the axial injection. Possible drawbacks, like the chocking effect of the rotational flow field and the resultant torque applied to the motor axis, are also considered and studied.

Sommario

I razzi ibridi sono un'alternativa interessante ai razzi solidi e liquidi per le loro caratteristiche uniche, dal momento che l'attenzione si sta spostando verso la sicurezza, i costi e l'impatto ambientale. I motori ibridi presentano diversi vantaggi, come ad esempio la sicurezza, l'affidabilità operativa, la modulabilità, il rispetto ambientale e i costi ridotti. Purtroppo sono affetti anche da alcuni svantaggi, il principale dei quali è la bassa velocità di regressione. I ricercatori internazionali stanno studiando una soluzione a questo problema, per poter sviluppare un razzo ibrido che sia realmente competitivo. Dopo aver presentato il processo di combustione ibrida, che si basa sulla formazione di uno strato limite turbolento, e dopo aver analizzato la teoria di Marxman sulla velocità di regressione, vengono descritti diversi metodi possibili, proposti per incrementare la bassa velocità di regressione.

La ricerca presente è focalizzata sull'uso dell'iniezione swirling di ossidante, in un motore ibrido dotato di un grano cilindrico di combustibile solido con una porta circolare. Lo studio condotto è principalmente un'analisi numerica, che si concentra sull'andamento dello scaling di questa configurazione particolare di motore a razzo ibrido, in relazione alla variazione dello swirl number geometrico e del flusso massico di ossidante. I risultati ottenuti dimostrano che questa tecnologia garantisce un aumento della velocità di regressione e delle prestazioni del motore ibrido, paragonato all'iniezione assiale. Sono stati presi in considerazione anche alcuni possibili svantaggi, come ad esempio l'effetto di chocking dell'ugello a cuasa del campo di moto rotazionale e la coppia risultante applicata all'asse del motore.

Table of Contents

List of Figures

List of Tables

Nomenclature

Acronyms

CAMUI	Cascaded multistage impinging-jet
CFD	Computational fluid dynamics
FDNS	Finite difference Navier-Stokes
GAP	Glycidyl azide polymer
GOX	Gaseous oxygen
HTPB	Hydroxyl-terminated polybutadiene
ORBITEC	Orbital Technologies Corporation
PE	Polyethylene
PMMA	Poly methyl methacrylate
RANS	Reynolds-averaged Navier-Stokes
SST	Shear stress transport
VEBH	Vortex end-burning hybrid
VFP	Vortex flow pancake
VHRE	Vortex hybrid rocket engine

Symbols

A	Area
a	Regression rate multiplicative coefficient, speed of sound
a_p	Constant
B	Blowing number
C_f	Skin friction coefficient
c	Constant
c_d	Discharge coefficient
c_p	Specific heat at constant pressure
c_v	Specific heat at constant volume
c^*	Characteristic velocity

D	Mass diffusivity
d	Diameter
Da	Damköhler number
G	Mass flux
h	Enthalpy
h_v	Effective heat of vaporization
I	Moment of inertia
I_{sp}	Specific impulse
k	Thermal conductivity
k_g	Gas phase absorption coefficient
L	Length
L_v	Latent heat of vaporization
Le	Lewis number
M_m	Molecular mass
$\dot{m}$	Mass flow rate
N_{hol}	Number of injector inlet holes
N_p	Particle number density
O/F	Oxidizer to fuel mass ratio
Pr	Prandtl number
$\dot{Q}$	Heat flux
R	Individual gas constant
R_u	Universal gas constant
r	Radius
$\dot{r}$	Regression rate
$\bar{\dot{r}}$	Average regression rate
SA	Swirl angle
SN	Swirl number
Sc	Schmidt number
St	Stanton number
p	Pressure
Re	Reynolds number
T	Temperature, torque
t	Time
v	Velocity
X	Molar fraction
x	Axial position
y	Normal position from the surface
α	Thermal diffusivity, absorptivity

α_p	Soot particle weight fraction
γ	Specific heat ratio
δ	Thermal boundary layer thickness
ε	Emissivity
η	Nondimensional position of the flame y_b/δ, combustion efficiency
μ	Dynamic viscosity
ν	Kinematic viscosity
ϱ	Density
σ	Boltzmann constant
τ	Time scale, shear stress
Φ	General fluid unknown
Φ_b	Velocity ratio v_b/v_e
ω	Angular velocity
$\dot{\omega}$	Angular acceleration

Subscripts and superscripts

ave	Average
ax	Axial injection
b	Burning
c	Chemical, combustion chamber
$conv$	Convective
e	Outer edge of the boundary layer
g	Gas, geometric
hol	Injector inlet holes
i	Internal, initial
inj	Injector outlet hole
f	Fuel, final
max	Maximum
mod	Modified
m	Regression rate exponential coefficient of length
n	Regression rate exponential coefficient of mass flux
o	Oxidizer
opt	Optimum
p	Port
r	Radial direction
rad	Radiative

s	Soot
sim	Simulation
sw	Swirling injection
t	Turbulent, throat
th	Theoretical
w	Wall
x	Local
z	Axial direction, motor axis
ϑ	Tangential direction
0	Initial conditions, without blowing, reference value

Introduction

ROCKET engines can be divided by the system used to produce exhaust matter, and thus thrust. Therefore it is possible to distinguish among three main rocket propulsion systems: *chemical* propulsion, *electrical* propulsion and *nuclear* propulsion [66].

The chemical rocket engine is the most common one and uses a combustion reaction of a propellant as source of energy. The heat released by the chemical process is used to increase the internal energy of the gaseous product, that is later converted into kinetic energy in the nozzle. The phase of the stored propellant is used to identify different types of chemical rockets, i.e. *liquid* (or gaseous) propellant rockets, *solid* propellant rockets and *hybrid* propellant rockets. A liquid rocket uses a propellant stored in a liquid phase in tanks, as shown in figure 1a. The propellant can be either a bipropellant, if oxidizer and fuel are two separated liquids (stored in two different tanks), or a monopropellant, if a single liquid contains both oxidizer and fuel (stored into a single tank). In a solid rocket the propellant is stored in a solid phase inside the combustion chamber, as can be seen in figure 1b. The oxidizer and the fuel are mixed together in the so-called solid grain. A hybrid rocket uses a propellant composed by a liquid phase, stored in a tank, and a solid one, stored in the combustion chamber. In the classical hybrid rocket, shown in figure 1c, the oxidizer is a liquid and the fuel is a solid. In the reverse hybrid, on the contrary, the oxidizer is a solid and the fuel is a liquid. However, research is focussed on the former configuration, mainly because solid oxidizers are less energetic than liquid ones (excluding cryogenic solid oxidizers, that involve storage issues) and because most liquid fuels must be handled with care. In figure 2 some different hybrid rocket motor configurations are schematically represented.

The operation of hybrid rockets is completely different from the one of solid and liquid rockets, even if they appear like an intermediate case, a mixture between the other two technologies. In a liquid rocket both the oxidizer and the fuel are injected in the combustion chamber, where they mix together to form a combustible mixture with a specific O/F ratio dependent on the two mass flows, while in a solid rocket the oxidizer and the fuel are pre-mixed in the solid grain with a fixed mixture ratio.

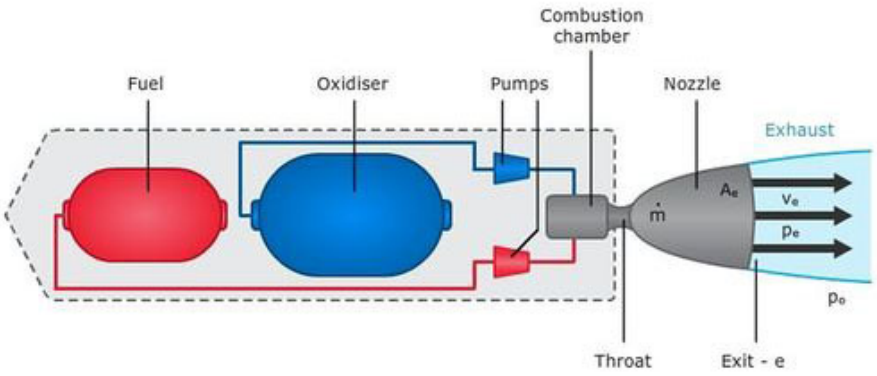

(a) Liquid rocket engine

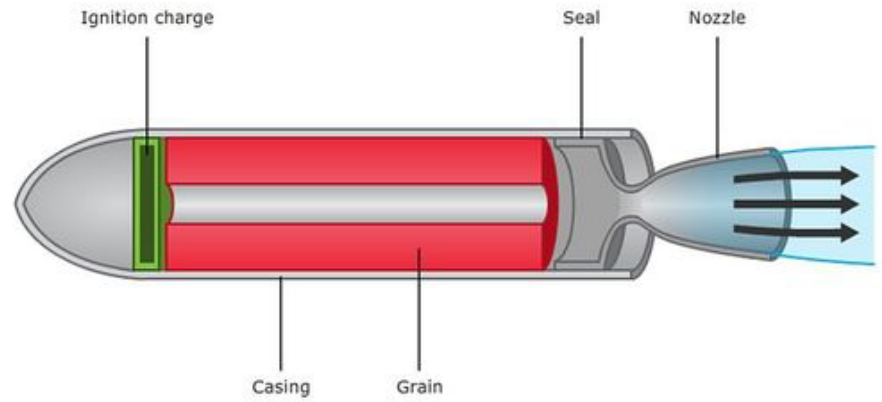

(b) Solid rocket engine

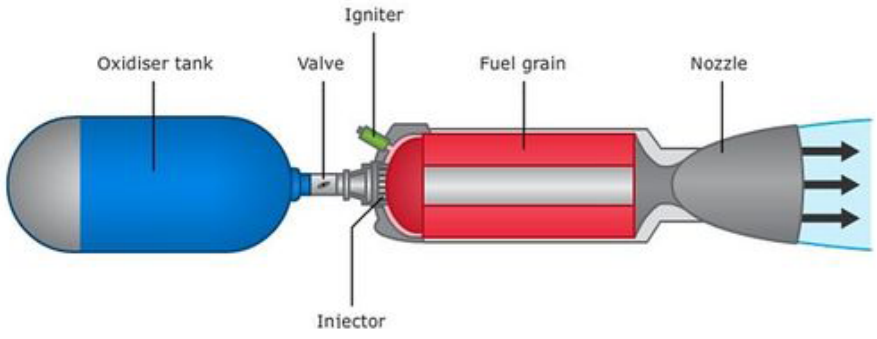

(c) Classical hybrid rocket engine

Figure 1: Schematic of the three different chemical rocket engines

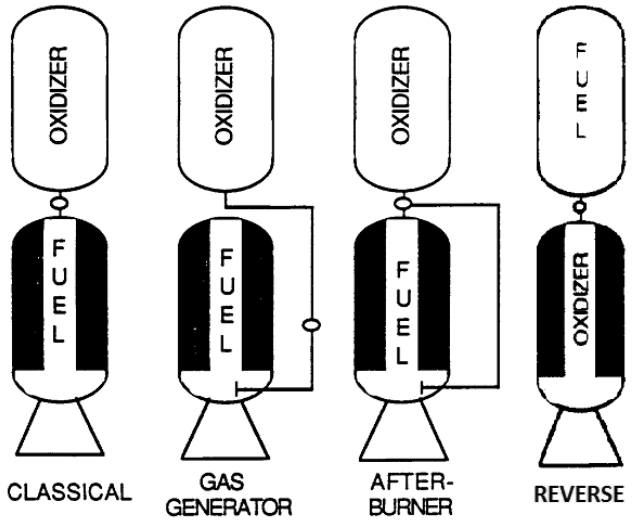

Figure 2: Hybrid rocket motor configurations

In both cases there is a uniform mixture in all the combustion chamber. Instead, in a hybrid rocket the oxidizer and the fuel are injected in the motor from different sides and they burn in a large diffusion flame, as will be explained in more detail later in chapter 1, where the O/F ratio varies along the length of the chamber. This fundamental difference involves a number of distinctive features. Hybrid rockets show several advantages compared to liquid and solid rockets [3, 18]:

- *Safety*: the solid grain is made only of inert fuel. Therefore the fabrication, the transportation, the storage and the handling can be done in complete safety. The oxidizer and the fuel are physically (by distance and phase) separated, thus there is no possibility of an explosion. Moreover, in case of an emergency abort operation, the motor can be stopped only closing the liquid oxidizer valve.

- *Operational reliability*: the combustion is regulated by a large diffusion flame, and hence the motor is less sensitive to grain imperfections and cracks and thus, compared to solid rockets, the possibility of a catastrophic failure is largely reduced. Compared to liquid rockets, only half of the turbo-machinery, tanks and plumbing parts are required.

- *Propulsive performance*: compared to solid rockets the theoretical specific impulse is higher, whereas the theoretical density-specific impulse is greater than the one characterizing liquid rockets. In figure 3 the propulsive performances, in term of specific impulse, of different solid, liquid, and hybrid rockets propellants are compared.

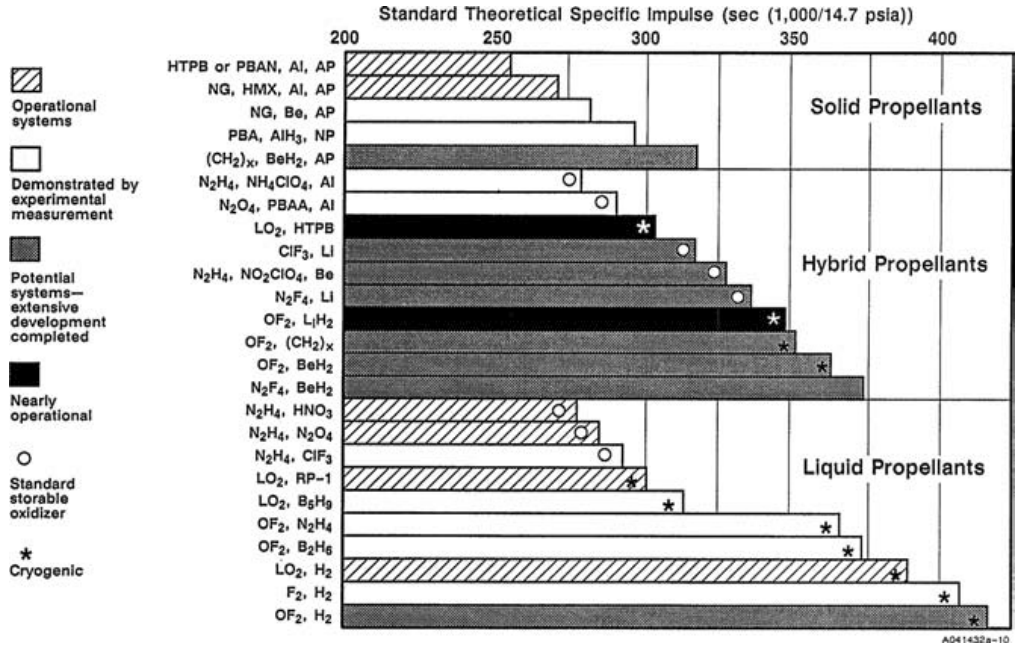

Figure 3: Theoretical specific impulse I_{sp} for different solid, liquid, and hybrid rocket propellants [18]

- *Throttling*: the rocket thrust can be varied in flight, controlling only the flow of the liquid oxidizer through the valve, which is simpler than in liquid rockets where two different liquid flows have to be modulated simultaneously.

- *Stop and restart capability*: the motor can be stopped and restarted many times (if an appropriate ignition system, capable of multiple firings, is provided).

- *Propellant versatility*: the selection of propellants is much greater than with either liquid or solid rockets. Dense metal particles can be added to the solid grain to improve the overall performance, without causing, like in liquid rockets, the formation of slurries. Furthermore, liquid oxidizers are more energetic compared to solid ones.

- *Environmental friendliness*: among the wide propellant choice, it is possible to find several green combinations of oxidizer and fuel.

- *Low cost*: the safe and inert propellant is the key advantage that affects the reducing of the total operational costs, because manufacture of the fuel can be done in a commercial facility that does not require large areas and many buildings for solid-propellant manufacture (as a consequence, the fuel plant can be located at or near the launch site) and also because handling and transport costs are greatly reduced. Moreover, the system can tolerate larger design margins, resulting in lower fabrication costs.

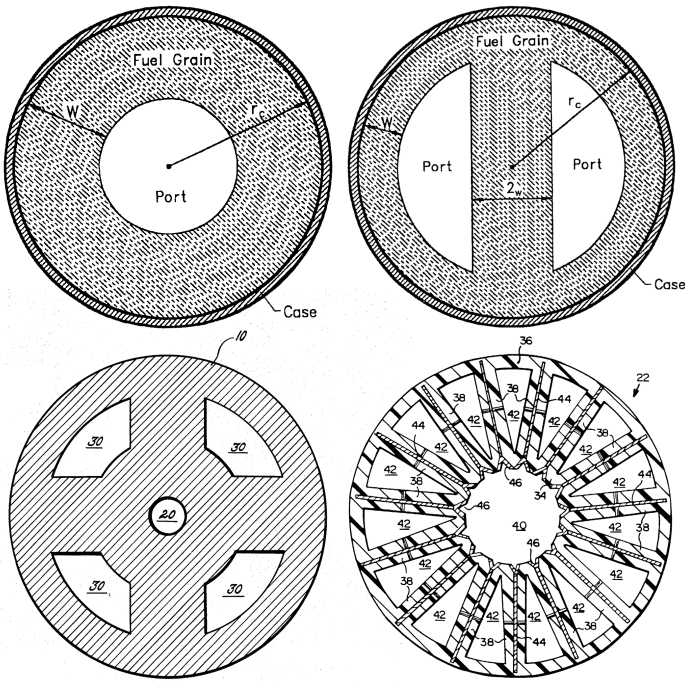

Figure 4: Example of increasing multi-port grain configuration

Unfortunately hybrid rockets also present several disadvantages compared to liquid and solid rockets:

- *Low regression rate*: because of the complex characteristic combustion, hybrid rocket motors suffer of a low regression rate (solid rockets are characterized by a regression rate that is generally one order of magnitude bigger than the one of hybrid rockets using polymeric fuels such as HTPB). Therefore, a large burning area is required to produce the necessary fuel mass flow, and hence the requisite trust. To achieve the desired area, a long combustion chamber could be used, but this would result in a too long motor. This goal can be reached in a better way if multi-port grains are used, as shown in figure 4, that implies some disadvantages like structural issues and increased inert mass (i.e. web supports), increased manufacturing costs, increased injection complexity, port shape changing during the burning time and different regression rate between ports.

- *Fuel residuals*: multi-port grains cannot be completely burned, to avoid the separation of portions of the fuel web supports between the grain ports and the consequent blocking of the nozzle, resulting in a certain quantity of fuel slivers at the end of the combustion time, as can be seen in figure 5.

- *Combustion inefficiency*: the large diffusion flame that controls the combustion process is the cause of a lower mixing of the chemical species involved in

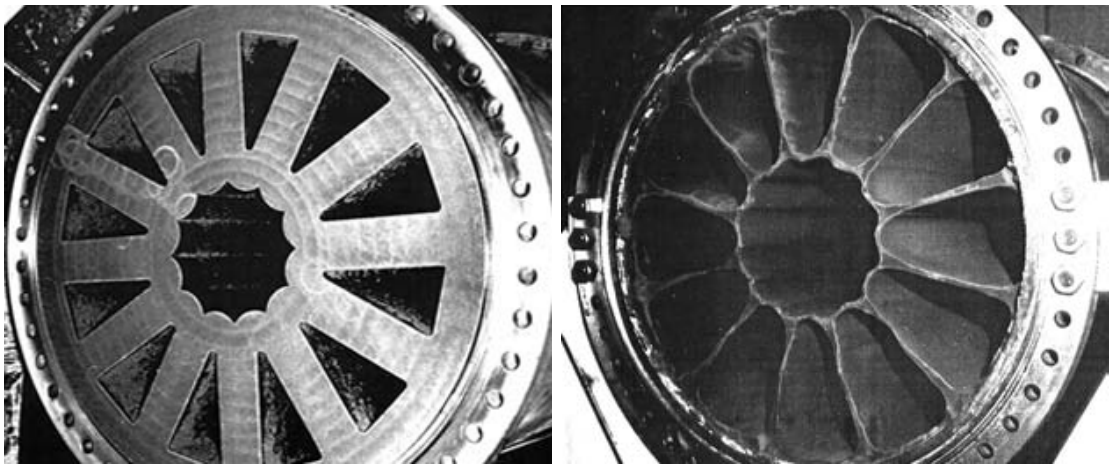

(a) Solid fuel grain before the firing test (b) Solid fuel grain after the firing test

Figure 5: Combustion of the multi-port solid fuel grain of an hybrid rocket motor [3]

the reaction, and thus a lower combustion efficiency, that in turn produces a decrease of the specific impulse compared to the theoretical value. To complete the mixing and the combustion of the reactants, it is possible to use a post-combustion chamber between the fuel grain and the nozzle.

- *Low volumetric loading*: the characteristic low regression rate causes a small web thickness and hence a poor volumetric loading. Moreover, the need for a post-combustion chamber increases the mass fraction losses even more.

- *Mixture ratio shift*: during the burning of a classical cylindrical grain with a circular port, i.e. a side-burning grain, the fuel port area enlarges, causing an increase of the fuel burning surface but also a decrease of the fuel regression rate. These two effects are generally not balanced, normally leading to a decrease in the fuel production rate. Therefore this causes a mixture ratio variation with burning time, and thus generally a decrease in the average specific impulse, as shown in figure 6.

- *Propulsive performance*: compared to solid rockets the theoretical density-specific impulse is lower, whereas the theoretical specific impulse is lower than the one characterizing liquid rockets, as can be seen in figure 3.

- *Slower transient*: ignition transients, as well as the response to throttling, are slower. In most applications, where reproducibility is more important than speed of response, this aspect can be neglected.

Liquid rockets usually have the highest specific impulse, they can be randomly throttled and can be stopped and restarted many times. Solid rockets have a

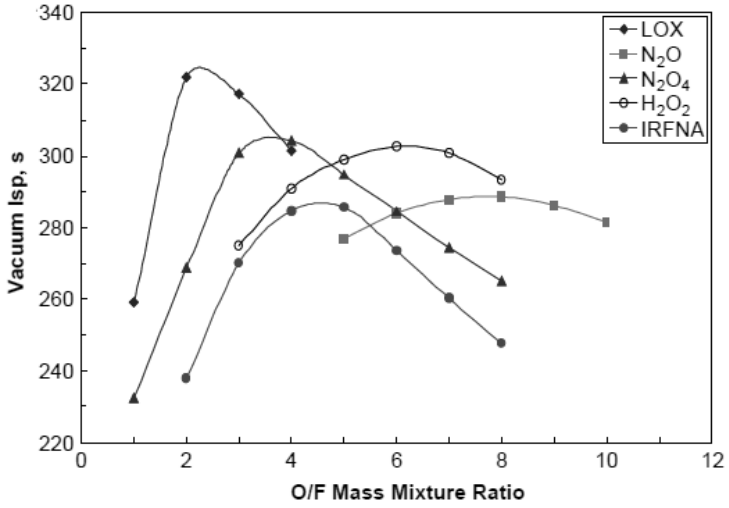

(a) Specific impulse I_{sp}

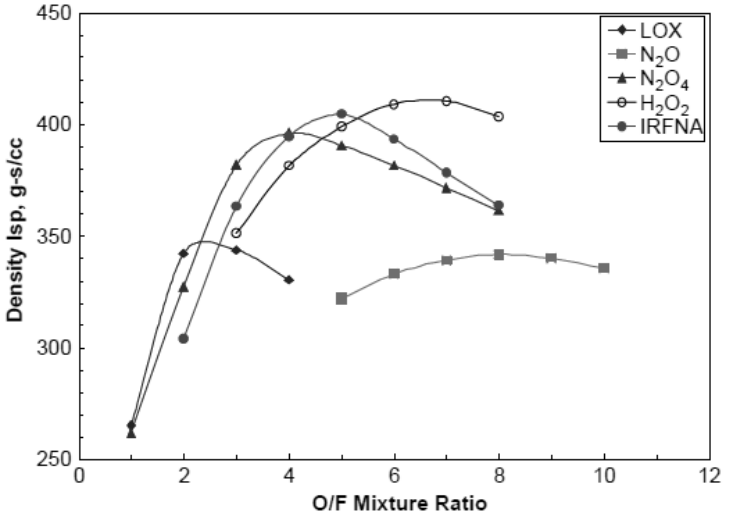

(b) Density specific impulse ϱI_{sp}

Figure 6: Variation of the specific impulse with the mixture ratio, for HTPB solid fuel burning with different oxidizers [18]

simple design, with none or only few moving parts, are ready to operate quickly, and usually have the highest density specific impulse. Hybrid rockets, offering a compromise in performance, have long been considered an intermediate case between the two, without showing a clear advantage. But liquid rockets have a complex and expensive design, with all the plumbing parts. Solid rockets cannot be throttled, or stopped and restarted, and for this type of rockets a failure can be catastrophic, with a larger potential of explosion. Hybrid rockets are an attractive alternative for their unique features, in a world becoming more careful about safety, costs and environmental impact.

Chapter 1

Hybrid Rocket Combustion Theory

The knowledge of the physical processes that occur during the combustion in hybrid rocket motors is necessary in order to have a complete understanding of the parameters that govern the regression of solid fuel grains. This knowledge is required because the regression rate is the key variable to design and optimize the shape of a solid grain, for a given specific impulse and thus a fuel mass, because it defines the internal ballistic characteristics of the motor.

Considering a classical hybrid rocket, the oxidizer is injected into the combustion chamber from the head end of the motor. After ignition, this causes the formation of a boundary layer, that is assumed to be turbulent for the typically high injection velocities and thus the high Reynolds numbers, located over the solid fuel surface. Inside this boundary layer, a macroscopic diffusion flame develops above the solid grain surface, dividing the layer into an oxidizer rich region and a fuel rich zone. The heat released from the combustion increases the temperature of the solid grain, causing its decomposition due to pyrolysis processes. Then, the vaporized fuel is transported to the flame by convection and diffusion, while the gaseous oxidizer is transported to the flame by turbulent diffusion. Here the gases mix together and react, sustaining the combustion. The particular configuration of the hybrid combustion leads to a characteristic self-regulating behaviour: the pyrolyzed fuel mass blocks a portion of the heat transfer to the solid grain surface, that in turn causes a decrease of the regression rate and of the corresponding wall blowing effect, weakening the blocking action, and thus enhancing the heat transfer to the surface, and so on [18].

In figure 1.1 the physical processes involved in the hybrid combustion, as well as the interfacial energy, chemical species and overall mass flux balances are qualitatively represented. The energy flux balance, that can be an useful starting point for an analytical study of the regression rate of hybrid motors, can be divided

into several different terms [18]:

- Term 1: it represents the heat flux transferred from the flame to the solid fuel surface by convection.
- Term 2: it represents the portion of the convected heat lost into the solid fuel by conduction.
- Term 3: it represents the heat flux transferred from the flame to the solid fuel surface by radiation.
- Term 4: it represents the part of the radiated heat lost into the solid fuel by conduction.
- Term 5: it represents the chemical enthalpy transferred to the solid fuel surface by fuel regression.
- Term 6: it represents the chemical enthalpy removed from the solid fuel surface by pyrolysis.
- Term 7: it represents the sensible enthalpy transferred to the solid fuel surface by fuel regression.
- Term 8: it represents the sensible enthalpy removed from the solid fuel surface by pyrolysis.

The chemical species mass flux balance is given by the difference between the species generated on the surface by pyrolysis and the species removed from the surface by bulk motion and diffusion. The fuel mass flux balance implies that the vaporized fuel mass flux is equal to the product of the regression rate and of the fuel density.

1.1 Marxman's Regression Rate Theory

The most important theory of hybrid combustion, explaining the regression rate behaviour, was developed in the early Sixties by Marxman et al., who based their analysis on the turbulent combustion over a flat surface [46–49]. It is assumed that the boundary layer, schematically represented in figure 1.2, is turbulent and that the combustion occurs in a infinitely thin flame zone, the so-called flame sheet approximation, located where the reagents concentration goes to zero. This is an acceptable approximation, even if this is not exact in a turbulent boundary layer, due to the temporal and spatial fluctuations of the flux quantities, as was experimentally observed by Marxman who estimated the flame thickness to be about 10% of the

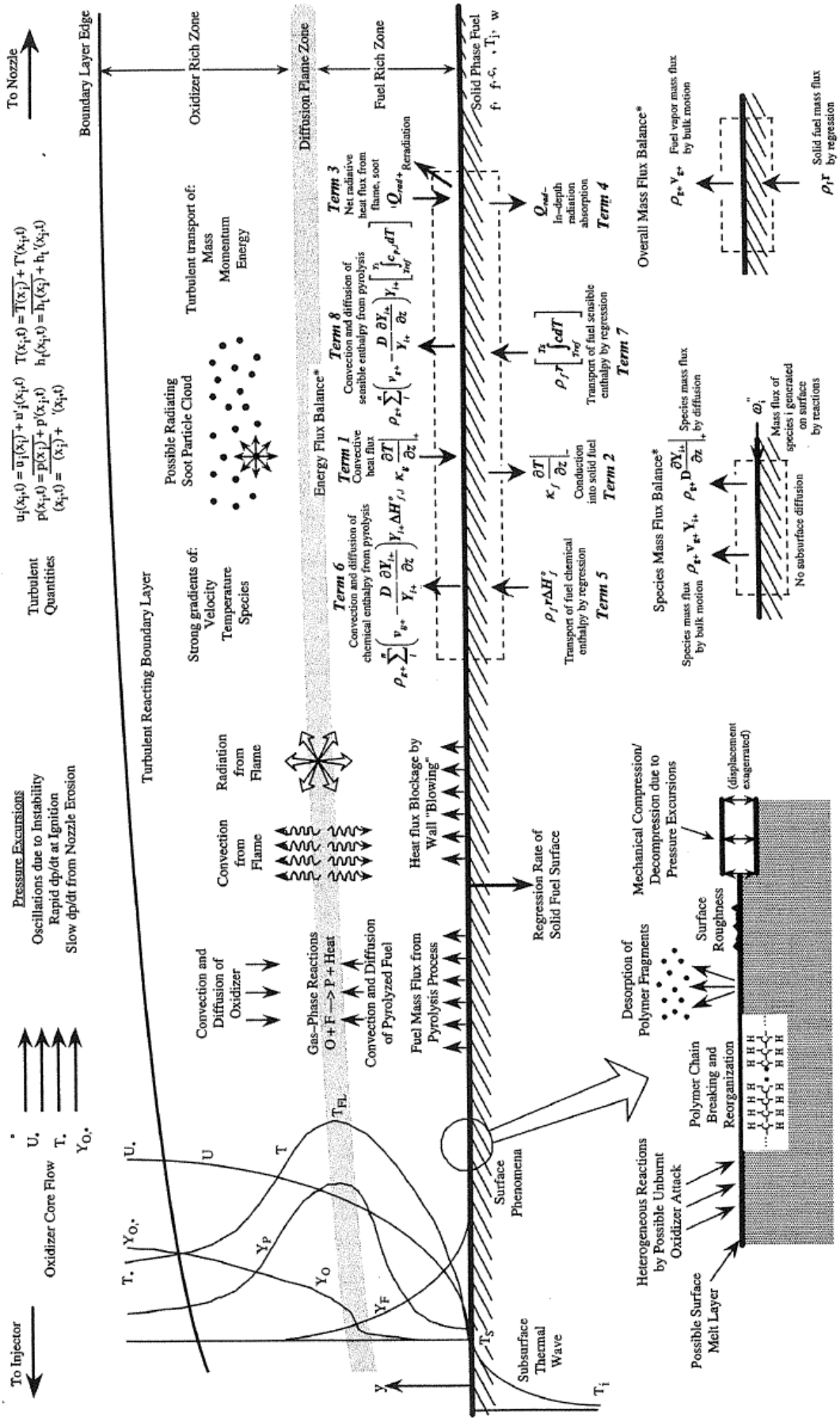

Figure 1.1: Physical model of hybrid rocket combustion [18]

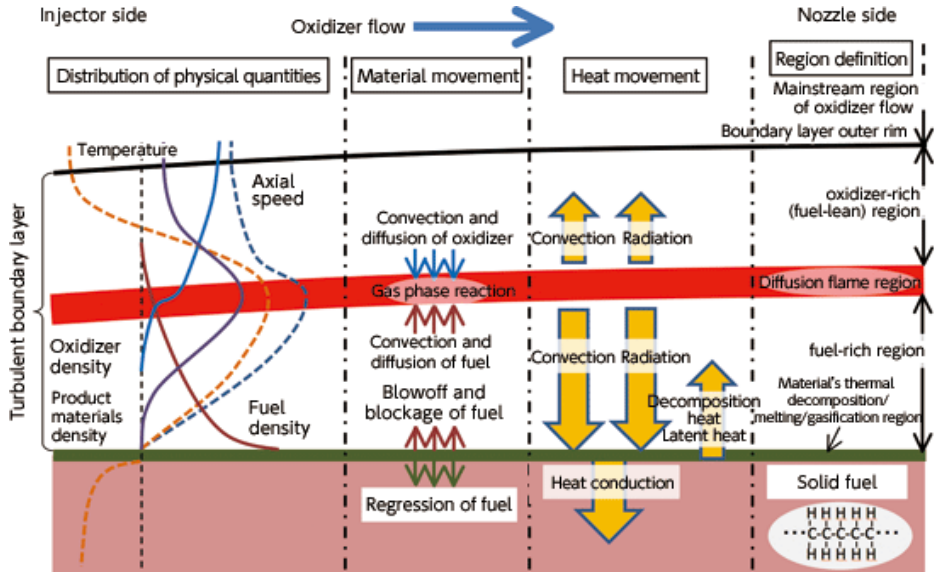

Figure 1.2: Hybrid rocket combustion boundary layer

boundary layer thickness and the flame position to be approximately 10–20% of the boundary layer thickness above the solid fuel surface, not exactly where the concentration of the combustion reactants equals the stoichiometric conditions. For hybrid rocket motor typical operating conditions the chemical reactions rate is much greater than the rate of mixing of the reactants in the turbulent flame, allowing to consider the combustion as controlled by the diffusion and as occurring with an infinite fast rate at the flame [5]. This is represented by a small Damköhler number, that is defined as the ration between the chemical time scale τ_c and the turbulent time scale τ_t:

$$Da = \frac{\tau_c}{\tau_t} \ll 1 \tag{1.1}$$

Assuming for simplicity a slab configuration and a steady state condition, a simplified heat balance at the solid fuel grain surface is the starting point to obtain a correlation for the regression rate:

$$\dot{Q}_w = \dot{m}_f h_v = \dot{r} \varrho_f h_v \tag{1.2}$$

where the effective heat of vaporization h_v is defined as the energy required to heat up the fuel from the initial temperature to the surface temperature plus the latent heat of vaporization L_v:

$$h_v = c(T_w - T_0) + L_v \tag{1.3}$$

The wall heat flux is given by the sum of a convective term and a radiative one, where the latter is usually small compared to the former, and thus is neglected. Another assumption is to set the Prandtl number and the Lewis number, and so

also the Schmidt number, equal to 1, implying that the thermal boundary layer, the momentum boundary layer and the species boundary layer have all the same thickness:

$$Pr = \frac{\text{momentum diffusivity}}{\text{thermal diffusivity}} = \frac{\nu}{\alpha} = \frac{\mu c_p}{k} = 1 \tag{1.4a}$$

$$Le = \frac{\text{thermal diffusivity}}{\text{mass diffusivity}} = \frac{\alpha}{D} = \frac{k}{\varrho c_p} = 1 \tag{1.4b}$$

$$Sc = \frac{\text{momentum diffusivity}}{\text{mass diffusivity}} = \frac{\nu}{D} = \frac{\mu}{\varrho D} = PrLe = 1 \tag{1.4c}$$

Therefore, it is possible to write the expression of the wall heat flux as:

$$\dot{Q}_w = \dot{Q}_{conv} + \cancel{\dot{Q}_{rad}} = -\left(k\frac{\partial T}{\partial y}\right)_w = -\left(\frac{k}{c_p}\frac{\partial h}{\partial y}\right)_w \tag{1.5}$$

The next step is to apply the Reynolds analogy between the solid fuel surface and the flame region, assuming that no chemical reactions occur beneath the flame. It is important to note that the conservation equation in the eulerian form for any fluid unknowns is:

$$\frac{\partial \Phi}{\partial t} + \bar{v} \cdot \nabla \Phi = D_\Phi \nabla^2 \Phi + S_\Phi \tag{1.6}$$

where the first term represents the time variation of the quantity Φ, the second term is the convective transport of Φ, the third term is the diffusion of Φ and the last term represents a source or sink for the quantity Φ. For the Reynolds analogy, since all the fluid unknowns follow a similar equation, also the solutions should be similar, and thus they have the same profile. As a result, only one profile is needed while the others can be obtained from the first, scaling the values accordingly. If the profiles of different variables are similar, the same happens for the derivatives of those profiles [5]. Therefore, the use of the Reynolds analogy permits to obtain the heat flux, that is proportional to the thermal gradient and in turn to the enthalpy gradient, from the shear stress, that is proportional to the velocity gradient:

$$\frac{\dot{Q}_w}{h_b - h_w} = \frac{\tau_w}{v_b - v_w} \tag{1.7}$$

but since the speed at the wall is null for the no-slip condition, the last equation can be written as:

$$\dot{Q}_w = \tau_w \frac{h_b - h_w}{v_b} \tag{1.8}$$

Now it is possible to correlate the wall shear stress τ_w with the skin friction coefficient C_f:

$$\tau_w = \frac{1}{2}\varrho_e v_e^2 C_f \tag{1.9}$$

and substituting this expression in equation (1.8), the following correlation of the wall heat is obtained:

$$\dot{Q}_w = \frac{1}{2}\varrho_e v_e C_f \frac{v_e}{v_b}(h_b - h_w) \tag{1.10}$$

that, using equation (1.2), can be written as:

$$\dot{r}\varrho_f h_v = \frac{1}{2}\varrho_e v_e C_f \frac{v_e}{v_b}(h_b - h_w) \tag{1.11}$$

The enthalpy difference, that from now on will be renamed as Δh, can be generalized removing the assumption that no chemical reactions occurs beneath the flame, because some experiments found a non-negligible presence of oxidizer in this zone, that can lead to chemical reactions at the solid fuel surface, like oxidizer attack at the grain wall:

$$\Delta h = h_b - h_w \tag{1.12}$$

In order to keep into account the vertical flow from the solid grain surface, caused by the blowing of the fuel, it is necessary to introduce the blowing number, which is a non-dimensional parameter that quantifies the mass addition to a boundary layer over a flat plate:

$$B = \frac{\dot{m}_f}{\frac{1}{2}\varrho_e v_e C_f} \tag{1.13}$$

The blowing number describes the different velocity profile and shear stress in the case with blowing, because the addition of the vertical flow increases the thickness of the boundary layer and thus reduces the velocity gradients, leading in turn to a decrease of the shear stress and of the heat flux. Introducing the blowing number, the expression of the mass flux from the wall becomes:

$$\dot{m}_f = \dot{r}\varrho_f = \frac{1}{2}\varrho_e v_e C_f B \tag{1.14}$$

Comparing this last expression with equation (1.11), it is possible to correlate the blowing number, the velocity ratio v_b/v_e and the enthalpy ratio $\Delta h/h_v$:

$$B = \frac{v_e}{v_b}\frac{\Delta h}{h_v} \tag{1.15}$$

Moreover, Marxman was able to express the velocity ratio v_b/v_e as function of the enthalpy ratio $\Delta h/h_v$ and of the mixture ratio at the flame O/F:

$$\Phi_b = \frac{v_b}{v_e} = \frac{O/F\dfrac{\Delta h}{h_v}}{X_{o_e} + (O/F + X_{o_e})\dfrac{\Delta h}{h_v}} \tag{1.16}$$

This means that the blowing number is determined only by the thermochemical properties of the propellant. As can be seen from equations (1.13) and (1.15), that define the blowing number, this quantity has a dual nature: it represents the similarity parameter of a boundary layer with mass flux from the wall, as well as a thermodynamic parameter quantifying the fuel regression, caused by the enthalpy difference between the flame and the solid grain surface. Hence, when the blowing number is constant and the Lewis number is unitary, the momentum profile, the species profile and the enthalpy profile are similar in all the turbulent boundary layer [18]. Furthermore, assuming as a first approximation that the flame is established where the chemical reactants concentration reaches the stoichiometric condition, Marxman obtained the position of the flame, that depends only on the blowing number and on the velocity ratio v_b/v_e, in relation to the thermal boundary layer thickness :

$$\eta_b = \frac{y_b}{\delta} = \left[\frac{\sqrt{1 + 2B\Phi_b\left(1 + \frac{1}{2}B\right)} - 1}{B} \right]^{\frac{1}{n}} \tag{1.17}$$

The introduction of the skin friction coefficient permits to solve a heat transfer problem using the extensive amount of data in the literature on friction in a turbulent boundary layer. The value of the skin friction coefficient in a boundary layer with blowing from the wall is computed from its value in the case without blowing of fuel:

$$C_f = \frac{C_f}{C_{f_0}} C_{f_0} \tag{1.18}$$

that, in turn, is obtained using an empirical correlation, developed for a turbulent incompressible flow over a flat plate:

$$C_{f_0} = 0.06 Re_x^{-0.2} \tag{1.19}$$

where:

$$Re_x = \frac{\varrho_e v_e}{\mu_e} x \tag{1.20}$$

Obviously, the approximation of incompressible flow is an invalid assumption which, however, allowed to simplify the theory in order to obtain a solution. Marxman derived an analytical expression of the ratio C_f/C_{f_0}, that represents the reduction of the skin friction coefficient due to the fuel blowing:

$$\frac{C_f}{C_{f_0}} = \left[\frac{\ln(1+B)}{B} \right]^{0.8} \left[\frac{1 + \frac{13}{10}B + \frac{4}{11}B^2}{(1+B)(1+\frac{1}{2}B)^2} \right]^{0.2} \tag{1.21}$$

This analytical expression, however, can be approximated with a numerical fit, over

a large interval of the blowing number:

$$\frac{C_f}{C_{f_0}} = 1.2B^{-0.77} \quad \text{for } 5 \leq B \leq 100 \tag{1.22}$$

or, using a more accurate expression, later developed by Altman [4]:

$$\frac{C_f}{C_{f_0}} = B^{-0.68} \quad \text{for } 5 \leq B \leq 20 \tag{1.23}$$

At this point all the quantities are known, and so substituting equations (1.18), (1.19), (1.20) and (1.23) in equation (1.14) it is finally possible to obtain an expression for the regression rate:

$$\dot{r}\varrho_f = 0.036\left(\frac{\mu_e}{x}\right)^{0.2}(\varrho_e v_e)^{0.8}B^{0.32} \tag{1.24}$$

that, introducing the local mass flux G, can be written as:

$$\dot{r}\varrho_f = 0.036\left(\frac{\mu_e}{x}\right)^{0.2}G^{0.8}B^{0.32} \tag{1.25}$$

Combining all the terms that are constant as a first order approximation, the last equation becomes:

$$\dot{r} = a_1 G^{0.8} x^{-0.2} \tag{1.26}$$

Moreover, averaging the regression rate expression over the solid grain length and the burning time, we obtain the space-time averaged form of the regression rate law:

$$\bar{\dot{r}} = aG_o^n L^m \tag{1.27}$$

where the oxidizer mass flux is defined as:

$$G_o = \frac{\dot{m}_o}{A_p} \tag{1.28}$$

The values of the coefficient a and of the exponents n and m are obtained through experimental data, because are different from the ones predicted by the theory developed by Marxman, considering all the assumptions and approximations introduced to obtain a solution.

1.1.1 Considerations on the Regression Rate Equation

Analysing equation (1.25), (1.15) and (1.16), it is possible to notice that the blowing number, and thus the regression rate, is proportional to the enthalpy ratio

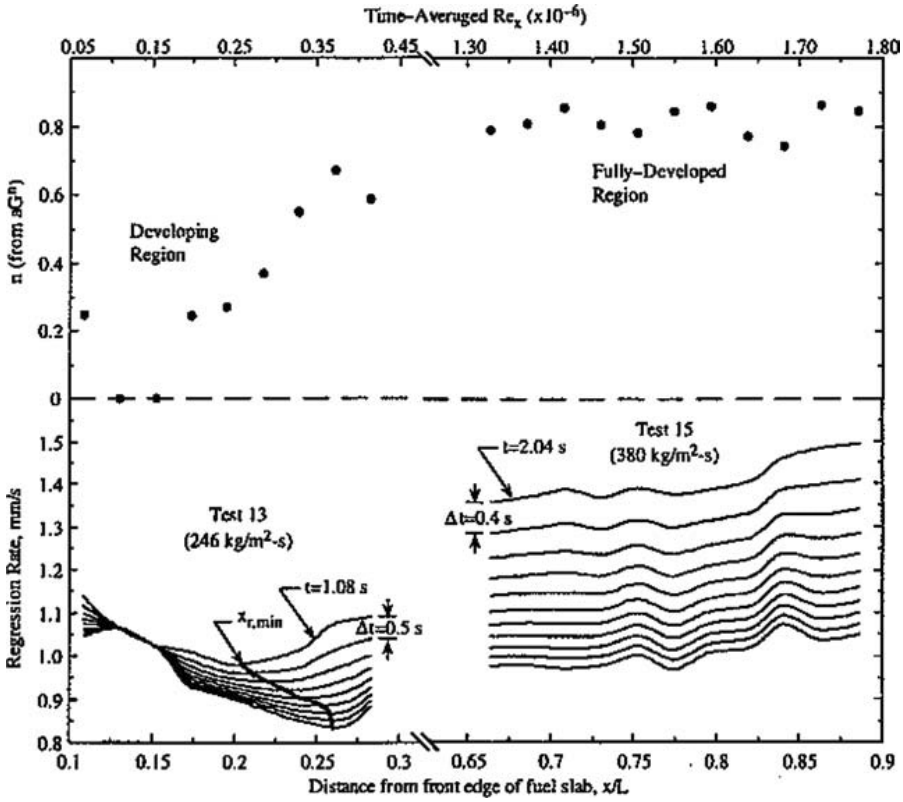

Figure 1.3: Regression rate of a laboratory-scale hybrid rocket motor [20]

$\Delta h/h_v$, that in turn is essentially fixed by the choice of the propellant combination. This behaviour could be easily explained, because a higher difference of enthalpy between the grain surface and the flame leads to higher thermal gradients, and thus to a higher heat flux, whereas a lower effective heat of vaporization results in lower energy necessary to vaporize the solid fuel. But since the blowing number is raised to a small power, changes of the enthalpy ratio $\Delta h/h_v$ have a small influence on the regression rate. This happens because enhancing the regression rate causes an increase of the fuel mass injected from the grain wall into the boundary layer, that reduces the convective heat transfer to the surface, which in turns leads to a decrease of the regression rate. This effect is called blocking effect [5, 18].

Looking again at equation (1.25), it is easy to see that the regression rate expression found by Marxman is mainly dependent on the local mass flux G. This quantity is the sum of the injected oxidizer mass flux and of the fuel mass flux added from the solid grain surface, and thus it increases along the motor length. However, the regression rate law has also a negative dependence on the axial position x, due to the increase of the boundary layer thickness that causes a decrease of the thermal gradients and in turn of the heat transfer between the flame and the solid grain wall. The presence of this two opposite effects results in the existence of a minimum regression rate location, as can be seen from figure 1.3 that summarizes the results

of the experimental tests conducted by Chiaverini et al. to analyse the internal ballistics of a laboratory-scale hybrid rocket motor [20]. From the head end of the grain until the minimum point, the regression rate decreases, due to the growing of the boundary layer, whereas downstream the minimum point, the increase of the local mass flux causes an increase of the regression rate. The result of this two opposite effects is a slow variation of the regression rate along the axial position [18]. Furthermore, this smooth trend is also enhanced by a self-compensating mechanism: the enlargement of the port area causes a local decrease of the mass flux, that in turn leads to a local decrease of the regression rate. This is an advantage compared to the coupling among burning area, mass flow, chamber pressure and regression rate in the solid rocket motors, that can lead to a catastrophic failure due to a variation of the burning area [5].

Moreover, the local mass flux decreases with the burning time, due to the enlargement of the port area, leading in turn to a similar behaviour of the regression rate variation with respect to time. This phenomenon causes the shift of the point of minimum regression rate to axial positions further downstream, because the effect of the local mass flux G on the regression rate is more important than the one of the axial position x, and thus the decrease of the local mass flux enhances the effects of the boundary layer growing [5, 18].

The regression rate correlation developed by Marxman has also a dependence on the scale of the motor. As the term that represents the length of the motor is raised to a negative power, the regression rate decreases for longer motors. But, since bigger motors require higher regression rate to have high volume loadings, this behaviour is the opposite than the desired one [5].

1.2 Effects of Thermal Radiation

The radiation term in equation (1.5) is not always negligible compared to the convective one: for example this is the case for solid grains with a high percentage of metal additives or for solid fuels that produce a high amount of soot. For this reason afterwards Marxman introduced a correction in order to add the radiation contribution, due to the gas phase combustion products, to the regression rate model. First, it is necessary to define the convective heat flux and the radiative heat flux as:

$$\dot{Q}_{conv} = 0.036 h_v \left(\frac{\mu_e}{x}\right)^{0.2} G^{0.8} B^{0.32} \tag{1.29a}$$

$$\dot{Q}_{rad} = \sigma \varepsilon_w (\varepsilon_g T_b^4 - \alpha_g T_w^4) \tag{1.29b}$$

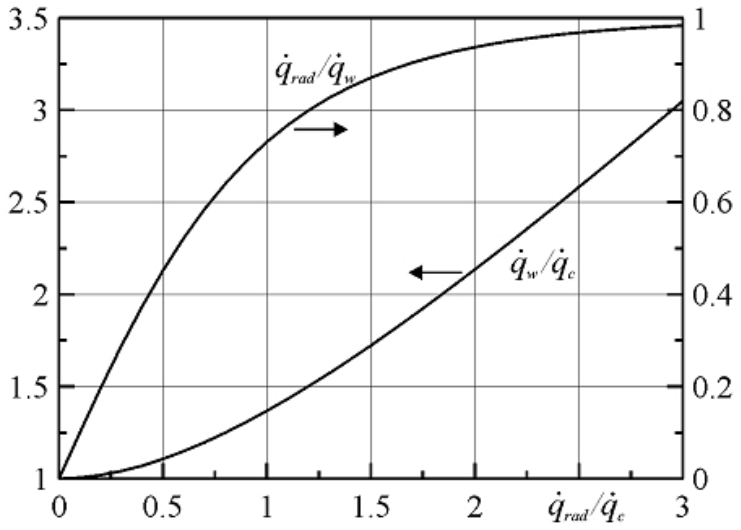

Figure 1.4: Coupling between the heat flux components

The radiation heat component is defined by two terms: the first one is the radiative heat flux emitted by the flame and absorbed by the wall, while the second one is the radiative heat flux emitted by the surface and absorbed by the flame. The latter term is generally negligible, because in hybrid rocket motors the typical temperature of the flame is about 3000 K and the surface has a temperature around 1000 K, whereas the gas phase reactions zone has a comparable emissivity and absorptivity [18].

It is now possible to write the expression of the regression rate for a system where both convective and radiant heat transfer act:

$$\dot{r}\varrho_f = \frac{1}{h_v}\left[\dot{Q}_{conv}\exp\left(-\frac{\dot{Q}_{rad}}{\dot{Q}_{conv}}\right) + \dot{Q}_{rad}\right] \tag{1.30}$$

Due to the intrinsic blocking effect of the hybrid rocket motors, a weak radiation heat component has a small effect on the total wall heat flux, and thus on the regression rate. This is because the enhancement of the total wall heat flux causes an increase of the regression rate, that in turn leads to a higher blowing of fuel from the solid grain surface, and thus causes the blocking of a larger portion of the convective heat flux. This is confirmed by Marxman's analysis, showing that the regression rate experiences an increase of only the 10% when a radiation component with a magnitude of half the convective heat flux is added [47]. Moreover, if the radiative heat flux is equal to the convection term in the case without radiation, the total wall heat flux, and thus the regression rate, is augmented of only the 47%, due to the decrease of the convective heat flux caused by the blocking effect [5]. In figure 1.4 a graphic representing the coupling among the convective heat flux, the

radiative heat flux and the total wall heat flux is shown. It is important to note that the emissivity term of the gas phase, which appears in equation (1.29b), is dependent on the pressure:

$$\varepsilon_g = 1 - e^{-k_g y p} \tag{1.31}$$

This means that the increase of the pressure enhances the influence of the radiative heat flux, and thus, when the radiation is the dominant component of the total wall heat flux, the regression rate is no longer dependent on the mass flux.

Furthermore, Strand et al. tested a laboratory scale hybrid motor, burning a slab solid fuel grain, to obtain an empirical analysis of the radiative heat flux, originated from both the gas phase and the soot particles. To reach this goal, the gas phase products radiation and the soot radiation were estimated using empirical expressions:

$$\dot{Q}_{rad_g} = \sigma T_g^4 \left(1 - e^{-k_g D p}\right) \tag{1.32a}$$

$$\dot{Q}_{rad_s} = \sigma T_g^4 \left(1 - e^{a_p N_p}\right) \tag{1.32b}$$

where the gas phase absorption coefficient k_g is dependent on the pressure, and the term $a_p N_p$ is a function of the particles weight fraction, the mixture ratio and the pressure:

$$k_g = 9.33 \times 10^{-4} - 6.19 \times 10^{-6} p + 1.79 \times 10^{-8} p^2 \tag{1.33a}$$

$$a_p N_p = 0.134 \left(\frac{\alpha_p p}{1 + O/F - \alpha_p} \right) \tag{1.33b}$$

The final finding was that the radiation component, including both the gas phase products term and the soot one, is more than the 50% of the total wall heat flux [65].

Moreover, considering a hybrid motor burning HTPB with GOX, Chiaverini et al. found that the radiative heat flux plays an important role in the regression rate, as can be seen in figure 1.5, that shows how the combustion chamber pressure influences the regression rate, with higher pressures causing an enhancement of the regression rate and a decrease of the dependence on the total mass flux, due to an increase of the radiative heat flux to the solid grain surface, in the low mass fluxes zone [19, 20]. Starting from the results of Strand et al., it was found that the radiation due to the soot was about 80% of the total radiative heat flux, and this term was represented by the following expression:

$$\dot{Q}_{rad_s} = \sigma T_g^4 \left(1 - e^{-k_s}\right) \tag{1.34}$$

where the soot absorption coefficient k_s is a function of the mixture ratio:

$$k_s = 0.51 - 0.113 O/F \tag{1.35}$$

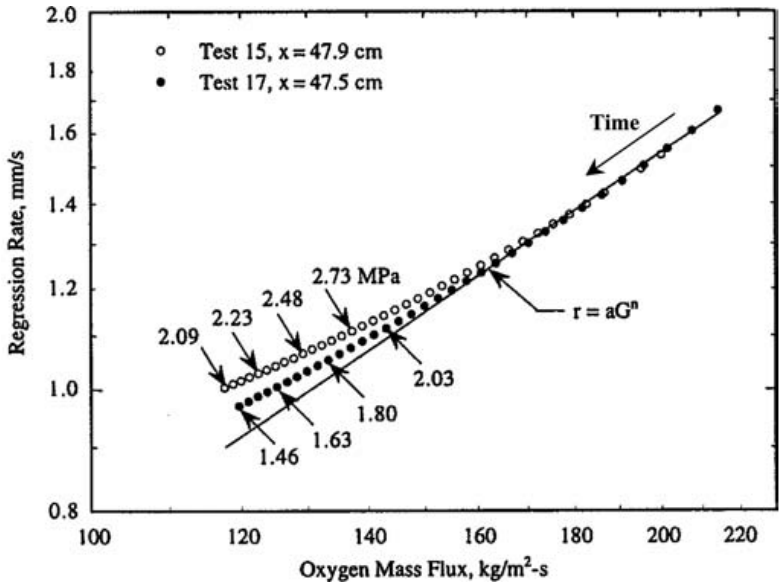

Figure 1.5: Effects of pressure on regression rate [20]

and this means that the soot emissivity decreases with the increase of the mixture ratio O/F, because there is more oxidizer to burn with the fuel produced by the pyrolysis of the solid grain. Including the radiative heat flux, a semi-empirical correlation of the regression rate was developed:

$$\begin{aligned}\frac{\dot{r}\varrho_f}{G} &= aStB\vartheta^b\left\{c\left(\frac{\dot{Q}_{rad}}{\dot{Q}_{conv}}\right)^d + \exp\left[-c\left(\frac{\dot{Q}_{rad}}{\dot{Q}_{conv}}\right)^d\right]\right\} \\ &= aStB\vartheta^b\left[f\left(\frac{\dot{Q}_{rad}}{\dot{Q}_{conv}}\right)\right]\end{aligned} \tag{1.36}$$

where a-d are empirical parameters, while the Stanton number St and the blowing number B are defined as follow:

$$St = \frac{\dot{Q}_{conv}}{G(\Delta h_r + \Delta h)} \tag{1.37a}$$

$$B = \frac{\Delta h_r + \Delta h}{h_v} \tag{1.37b}$$

The comparison between the radiative component of the total wall heat flux in equation (1.30), developed by Marxman, and in equation (1.36), developed by Chiaverini, is presented in figure 1.6. Even if equation (1.36) does not have a simple form, each factor accounts for different physical aspects [18]:

- The blowing number B and the Stanton number St represent the heat transfer to the solid fuel surface, considering a turbulent boundary layer with blowing.

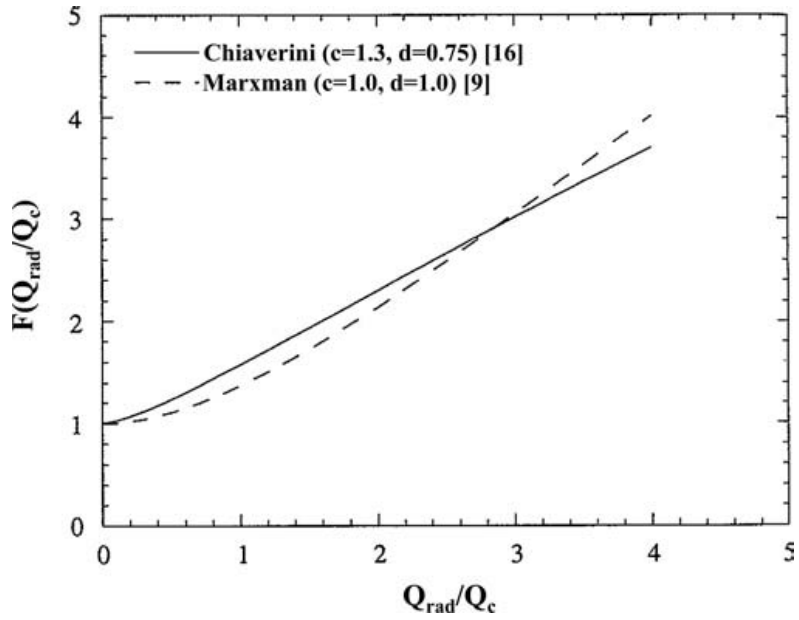

Figure 1.6: Comparison between the radiation component in equations (1.30) and (1.36) [18]

- The term ϑ, that is the ratio between the flame temperature and the wall temperature, represents the variation of the fluid and transport properties in the shear stress boundary layer.

- The term in brackets represents the radiative component of the total wall heat flux.

1.3 Effects of Chemical Kinetics

The results of the regression rate theory proposed by Marxman are based on the hypothesis that for typical operating conditions of hybrid rocket motors the Damköhler number is small, i.e. the chemical reactions rate is much greater than the rate of mixing of the reactants in the turbulent flame, as expressed by equation (1.1). But, in the operating region of very high mass fluxes this approximation is not valid, because the turbulent time scale is no longer lower than the chemical time scale, due to the large decrease of the residence time of the gases in the combustion chamber, caused by the increase of the oxidizer velocity. Therefore, in this region is necessary to include the chemical kinetic, that involves a reduction of the regression rate. The combustion chamber pressure influences the regression rate, because an increase of pressure causes an enhancement of the chemical reactions rate, and thus of the regression rate itself.

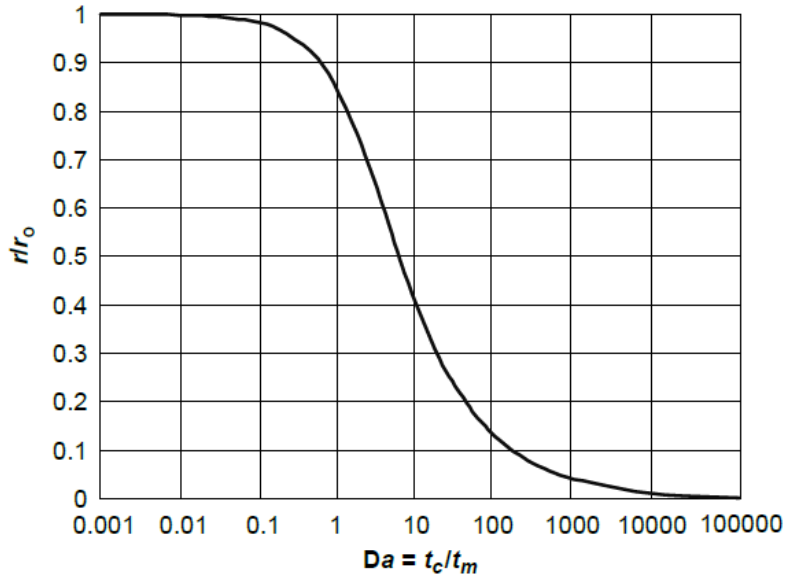

Figure 1.7: Variation of the regression rate with the Damköhler number [18]

The regression rate dependence on the pressure in the very high mass fluxes can be explained with several theories, that are based on three different approaches [18]:

1. The pressure dependence is caused by the kinetics of the chemical reactions of the gas phase, between the oxidizer and the pyrolyzed fuel.

2. The pressure dependence is causes by the kinetics of the heterogeneous reactions, between the oxidizer and the fuel at the solid grain surface.

3. The pressure dependence is caused by both the gas phase and the heterogeneous reactions kinetics.

Taking into account both the gas phase and the heterogeneous reactions kinetics, Wooldridge and Marxman derived a regression rate expression, dependent on the Damköhler number (1.1):

$$\frac{\dot{r}}{\dot{r}_0} = \left(\frac{2}{Da}\right)^{0.5} \left\{1 - \frac{1}{Da}[1 - \exp(Da)]\right\}^{0.5} 6 \tag{1.38}$$

where r_0 is the reference regression rate, such as that given by (1.25), computed for the mass flow region of pressure independence and flux dependence. The correlation between r/r_0 and the Damköhler number is plotted in figure 1.7.

The chemical kinetics is the limiting parameter when the Damköhler number is high, that happens when the combustion chamber pressure is low or when the

mass flux is high. In this region the previous equation simplifies to:

$$\frac{\dot{r}}{\dot{r}_0} = \left(\frac{2}{Da}\right)^{0.5} \tag{1.39}$$

The Damköhler number can be approximated, considering a second-order reaction, with the following expression:

$$Da = c_1\left(\frac{G^{0.8}x^{-0.2}}{p}\right) \tag{1.40}$$

where the constant c_1 includes the blowing parameter, the flame temperature and the gas viscosity [18]. Substituting equation (1.40) in equation (1.39):

$$\frac{\dot{r}}{\dot{r}_0} = c_2\left(\frac{p^{0.5}x^{0.1}}{G^{0.4}}\right) \tag{1.41}$$

Moreover, substituting the value of the reference regression rate r_0 with equation (1.25), it is possible to write the expression of the regression rate for the kinetically controlled region:

$$\dot{r} = cp^{0.5}G^{0.4}x^{-0.1} \tag{1.42}$$

Even if this correlation has a qualitative meaning, it is important to understand that, in the region of very high mass fluxes, the regression rate is dependent on the pressure of the combustion chamber, and that it has a lower dependence on the total mass flux and on the axial position.

1.4 Regression Rate Behaviour Summary

Figure 1.8, that qualitatively represents the correlation between the regression rate and the total mass flux in a logarithmic plot, is a valuable aid to summarize the effects of the thermal radiation and of the chemical kinetics on the regression rate behaviour [5, 18]:

- For intermediate mass fluxes the regression rate is dominated by the turbulent diffusion, and thus is independent from the radiation or from the chemical kinetics, and it is represented by the basic Marxman relation, that in a logarithmic plot is a straight line with a slope equal to the exponent n.
- For low mass fluxes the influence of the radiative heat flux increases, because the turbulent convection component of the total wall heat flux is small,

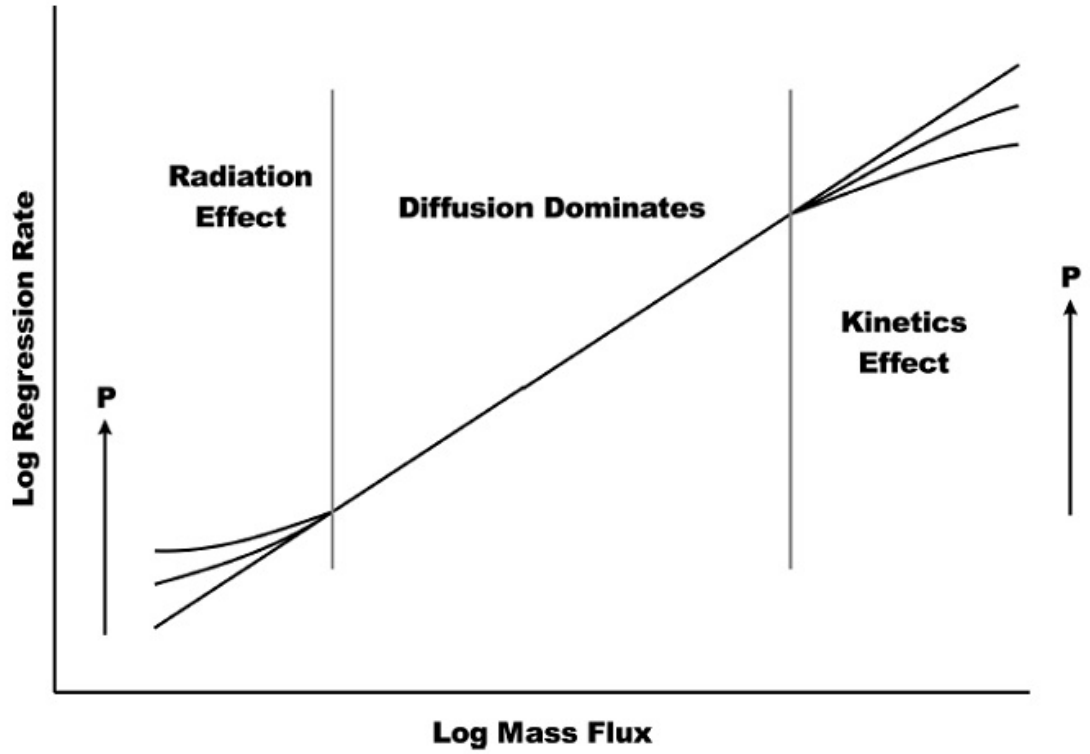

(a) Logarithmic plot

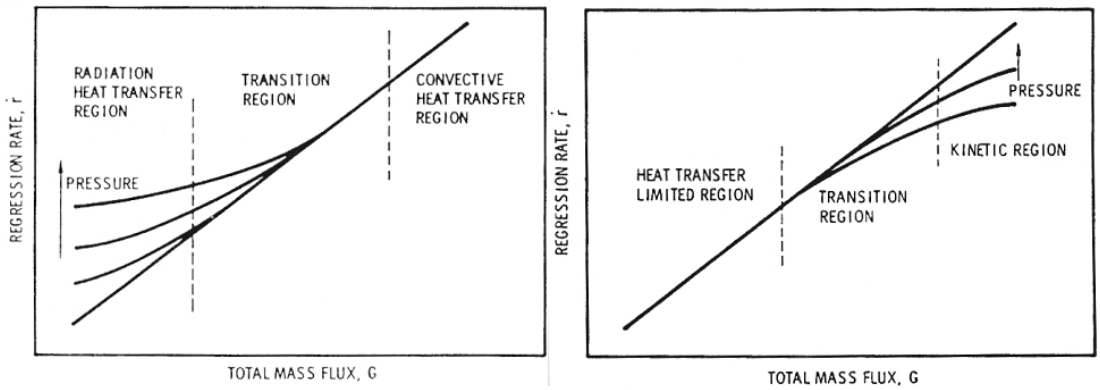

(b) Zoom of the pressure dependent regions

Figure 1.8: Variation of the regression rate with the total mass flux [5]

causing a flattening of the slope of the curve. In this region the decrease of the combustion chamber pressure leads to an increase of the linear part of the curve, further decreasing the regression rate.

- For high mass fluxes the effect of the chemical kinetics is more important, because the residence time of the gases is greatly reduced, causing a decrease of the slope of the curve. In this region the increase of the pressure leads to an increase of the linear part of the curve, and thus to an enhancement of the regression rate.

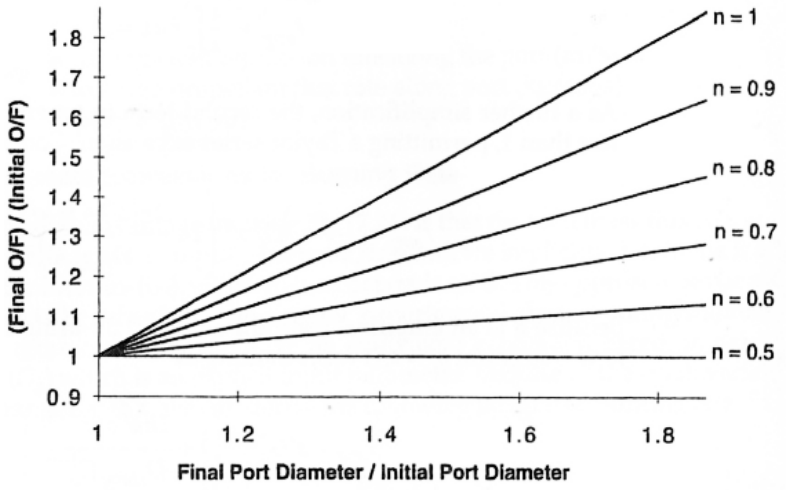

Figure 1.9: Mixture ratio shift with port diameter [5]

1.5 Mixture Ratio Shift

As already anticipated in the introduction, one of the disadvantages of hybrid rocket motors is the mixture ratio shift, that occurs during the burning time. For liquid rockets, the oxidizer to fuel ratio can be directly controlled adjusting the inlet propellant mass flows, and for solid rockets the ratio is constant, since fuel and oxidizer are premixed in the solid grain matrix. Contrariwise, for hybrid rockets the mixture ratio shifts during the operation, because only the oxidizer mass flow can be directly controlled, whereas the fuel generation is determined by the complex combustion process: considering a classical cylindrical grain with a circular port, i.e. a side-burning grain, the fuel port area enlarges during the burning, causing an increase of the fuel burning surface but at the same time a decrease of the fuel regression rate. These two effects are generally not balanced, leading to a mixture ratio variation with burning time.

Describing the regression rate law, for a single circular port, with equation (1.27), it is possible to define the mixture ratio, that is the ratio between the oxidizer and the fuel, as following:

$$O/F = \frac{\dot{m}_o}{\dot{m}_f} = \frac{d_p^{2n-1}\dot{m}_o}{a\pi^{1-n}4^n\varrho_f L} \tag{1.43}$$

It is possible to analyse two different situations:

- Variation of the O/F with constant oxidizer mass flow
- Variation of the O/F with variable oxidizer mass flow

The first case occurs when the oxidizer mass flow is kept constant during the combustion. With the passing of the burning time, the circular port of the solid

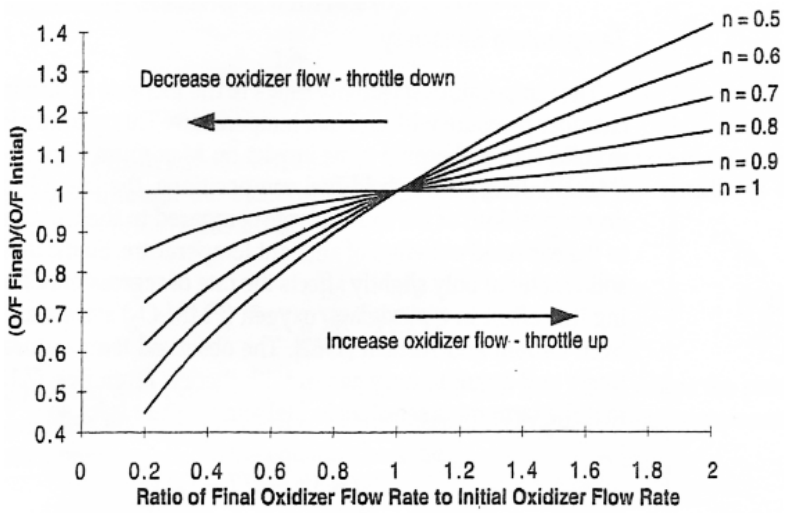

Figure 1.10: Mixture ratio shift with oxidizer mass flux [5]

grain enlarges, leading to a decrease of the oxidizer mass flux and thus of the regression rate, and obviously also resulting in an increase of the burning fuel area. The fuel mass flow results from the balance between the regression rate and the fuel area, because it is dependent on both these two variables. Considering that only the port diameter varies with time and that the exponent of this parameter is $2n - 1$, for $n = 0.5$ there is no mixture ratio shift, because the increase of the burning area is balanced by the reduction of the regression rate. On the contrary, for $n < 0.5$ the mixture ratio decreases during the burning time, because the enlargement of the port area is more relevant and thus the fuel mass flow increases, whereas for $n > 0.5$ the mixture ratio increases with time, because the reduction of the regression rate prevails leading to a decrease of the fuel mass flow. The variation of the mixture ratio O/F with the port diameter is represented in figure 1.9

The second scenario is when the oxidizer mass flow is throttled. The mixture ratio depends on the oxidizer mass flow, that is raised to the power of $1 - n$. Hence, for $n = 1$ there is no mixture ratio shift, because this case represents a linear correlation between the oxidizer mass flow and the fuel mass flow, but since the flux exponent predicted by Marxman is $n = 0.8$, the fuel mass flow variation is sub-linear, leading to a mixture ratio shift during the throttling, as can be seen in figure 1.10. Since the variation of the fuel mass flow caused by the oxidizer throttling is lower than the ideal case, this makes necessary a higher throttling ratio to obtain the wanted fuel variation.

Chapter 2

Enhancement of the Regression Rate

THE most limiting feature of hybrid rockets is the intrinsically low regression rate, that, as was already explained in chapter 1, derives directly from the diffusion flame that controls the combustion process. International researches are mostly focussed on finding a solution to this issue, encouraged by the great study of Casillas et al., demonstrating that a three-to-fourfold increase in the regression rate may be satisfactory to develop a really competitive hybrid rocket motor, that will be able to compete with the well-known liquid and solid rocket technology [14]. Possible methods are the addition of a certain quantity of oxidizer to the solid fuel grain or the replacement of the inert fuel with a more energetic binder to increase its reactivity, but this will convert the grain from a inert solid fuel (like the very common HTPB) to a fuel rich solid propellant (like GAP). Another technique is the employment of a high-energy oxidizer, but this will lead to the formation of exhaust gases that cannot be considered environmental friendly any longer for the presence of products of the combustion reaction containing chlorine [62]. Four main approaches that have been developed to increase the regression rate, without reducing the inherent advantages of the hybrid rockets, look promising:

- *Solid fuel additives*: the addition of energetic particles to the solid fuel grain leads to a substantial enhancement of the pyrolysis process of the fuel, and hence of the regression rate. Using metals as additives has some inherent advantages such as an increase in the specific impulse and in the density-specific impulse, because adding this type of particles to the solid fuel ensures an higher heat of combustion and an increased density of the grain. The combustion of the metal additive near the surface of the fuel increases the heat released and in turn the heat that is transferred back to the solid grain surface from the combustion zone, causing an enhancement of the pyrolysis of the fuel and thus an increase of the regression rate. The most popular metal

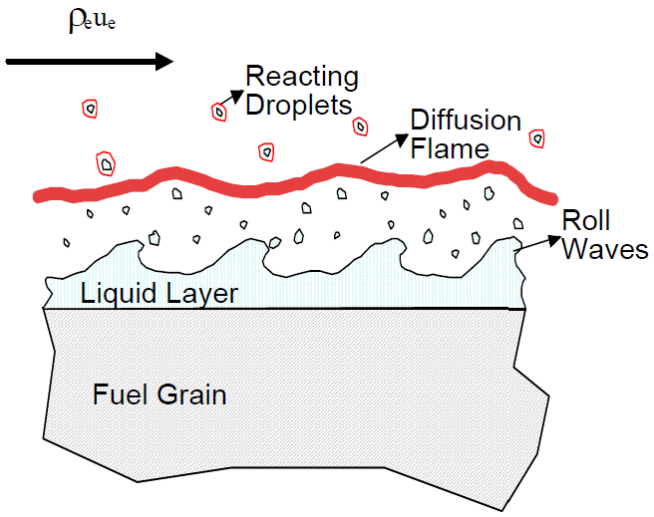

Figure 2.1: Physical model of paraffin-based fuel combustion [30]

additive is aluminium, because of its high heat of oxidation, high density, ease of ignition, low cost and ease of processing [62].

- *Liquefying solid fuels*: paraffin-based or cryogenic fuels show a characteristic behaviour, because they form a very thin hydro-dynamically unstable liquid film, with low viscosity and low surface tension, on the melting fuel surface during the burning time. The oxidizer flow causes the entrainment of small droplets from the liquid-gas interface, greatly increasing the fuel mass transfer and thus the regression rate, up to 3-4 times compared to conventional hybrid rockets fuels [30, 31]. The combustion process of the liquefying fuels is shown in figure 2.1.

- *Diaphragm*: the induction of a strong level of turbulence in the flow field by the mean of a diaphragm, as can be seen in figure 2.2, improves the mixing of the reactants, thus increasing the combustion efficiency, and intensifies the heat transfer to the solid fuel grain surface, leading to an enhancement of the regression rate. The improvement caused by the diaphragm depends on its geometry and position along the motor [12, 24].

- *Nonconventional solid fuel grain geometries and unique injector designs*: different methods to increase the fuel regression rate are currently under study and test, based on various grain geometries and different swirl injectors, or a combination of both. The key operating principle is to alter the classical flow field in the combustion chamber in order to improve the heat transfer to the solid fuel grain surface and thus the regression rate. The most promising approaches are [18, 60]:

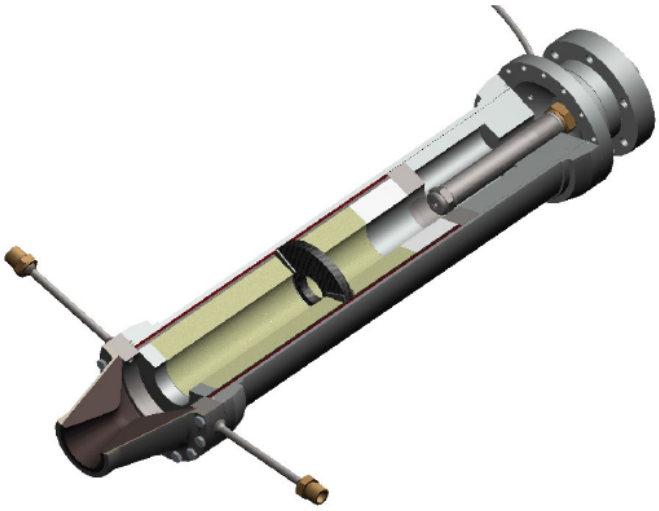

Figure 2.2: Single hole diaphragm [24]

- Swirl injection in side-burning grains
- Vortex hybrid rocket engine
- Swirl injection in end-burning grains
- Axial injection in end-burning grains
- Radial injection in end-burning grains

The solutions presented are mostly still investigated at a laboratory scale and need further researches, to better understand the scaling effects. This thesis is focussed on the last presented method, and especially on the swirl injection in side-burning grains, used to obtain a substantial increase of the combustion efficiency and of the regression rate.

2.1 Swirl injection in side-burning grains

A hybrid rocket with a swirl injector at the fore end of the motor was experimented by Yuasa et al., to find a solution to the low regression rate and to the poor combustion efficiency. The configuration is characterized by a tangential oxidizer injector, located at the motor head end, used together with a classical cylindrical solid grain with a circular port, i.e. a side burning grain. A regression rate about 2.7 greater than that for classical axial flow hybrid rockets was found, for a motor using PMMA as fuel burning with gaseous O_2 as oxidizer [18, 67, 71, 73].

Conducting several experiments with different injector designs, the effects of the swirl strength and of the oxidizer mass flux on the regression rate were analysed, varying these two parameters independently. The injectors are characterized by

the geometric swirl number, whose definition comes from the conservation of the momentum following the convention proposed by Beer and Chigier [7]:

$$SN_g = \frac{(r_{inj} - r_{hol})r_{inj}}{N_{hol}r_{hol}^2} \tag{2.1}$$

This approach permits to use only geometrical parameters, namely the dimensions of the injection plate, in order to compare different situations, without the need for specific measurements of local fluid unknowns. Moreover, an axial injector was used to find a baseline regression rate correlation, that made possible to evaluate the improvements in terms of performance of the swirl injector compared to the axial one.

The researchers also studied the effect of the solid fuel grain length on the average regression rate, using two different grain geometries of 150 mm and 500 mm. Based on the results of the tests, a correlation of the average regression rate with the oxidizer mass flux was obtained, based on the classical hybrid rockets regression rate equation:

$$\bar{\dot{r}} = aG_o^n \tag{2.2}$$

As can be seen from the plot in figure 2.3, the regression rate multiplicative coefficient a varies approximately linearly with the geometrical swirl number, for both the solid fuel grain geometry. This behaviour is consistent with the observed increase in the average regression rate with stronger swirling flow fields. It is important to remark that the tests with the shorter grain length correspond to a lower oxidizer mass flux of about $10\,\mathrm{kg/m^2}$ to $20\,\mathrm{kg/m^2}$, while the tests with the longer grain length correspond to a higher oxidizer mass flux of about $40\,\mathrm{kg/m^2}$ to $60\,\mathrm{kg/m^2}$. Furthermore, from the trend of the regression rate exponential coefficient n, that does not change significantly with the geometric swirl number, it is possible to understand that the strength of the swirling flow field does not cause a substantial variation of the nature of the heat transfer in the turbulent boundary layer, but only alters its magnitude. The exponential coefficient, instead, increases with the oxidizer mass flux, from about 0.6 for the lower G_o range to about 0.8 for larger values of G_o. This behaviour indicates that a lower oxidizer mass flux enhances the influence of the thermal radiation on the regression rate, while the increase in the oxidizer mass flux causes a stronger dependency of the regression rate on the turbulent heat transfer, represented by $n \approx 0.8$.

Moreover, Yuasa et al. analysed the solid fuel grain axial regression rate profile, figuring out that the increase of the geometrical swirl number involves a weakening of the dependency of the local regression rate on the axial location. This in turn

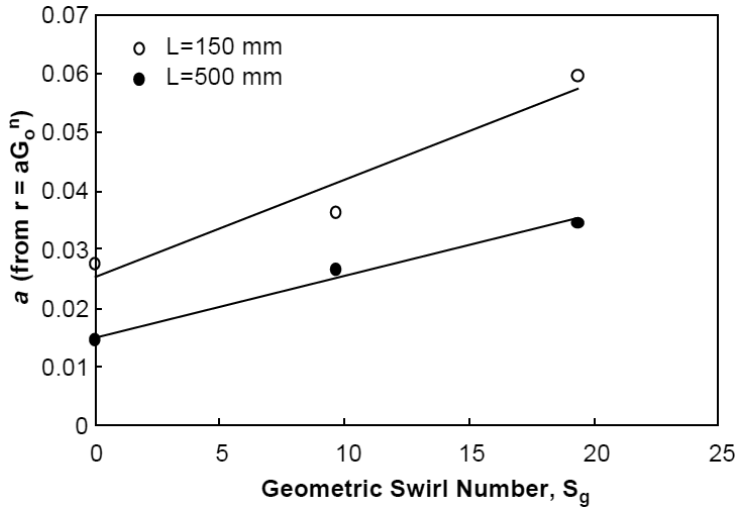

Figure 2.3: Correlation between the geometrical swirl number SN_g and the regression rate multiplicative coefficient a [18]

leads to a more uniform regression of the solid fuel grain.

The injection of the oxidizer with a strong tangential velocity component produces helical streamlines in the combustion chamber. This characteristic flow field enhances the heat transfer to the grain wall for several reasons, namely reducing the boundary layer thickness and retarding its growth along the motor axis, thanks to an increment in the velocity by the additional tangential velocity component, and increasing the density of the gases near the solid fuel wall, due to the centrifugal force. Furthermore, the swirling flow field enhances the mixing of the reactants and the residence time of the gases, improving the combustion efficiency.

2.2 Vortex hybrid rocket engine

Designed and developed by Knuth et al. at ORBITEC (Orbital Technologies Corporation), the vortex hybrid rocket engine (VHRE) uses a swirl injector, that is situated between the aft end of the combustion chamber and the nozzle entrance section, and a classical cylindrical solid fuel grain with a circular port, i.e. a side burning grain, as can be seen in figure 2.4a. The oxidizer is injected tangentially into the combustion chamber, producing a flow field in the motor that is characterized by a pair of coaxials, coswirlings and counterflowings vortices, that are schematically represented in figure 2.4b. The outer vortex spirals along the fuel surface toward the motor head end, mixing and burning with the pyrolized fuels. At the fore end, the outer vortex flows inward toward the motor axis and it turns into an inner vortex that spirals downward and out the nozzle. The strong centrifugal forces and the radial pressure gradients, associated with the tangential injection, prevent

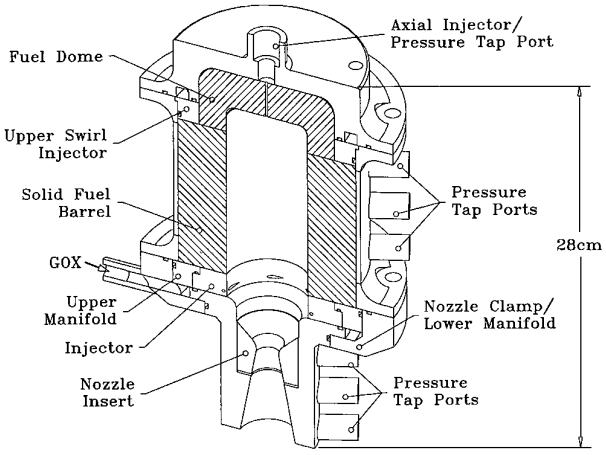

(a) Schematics of the laboratory scale motor

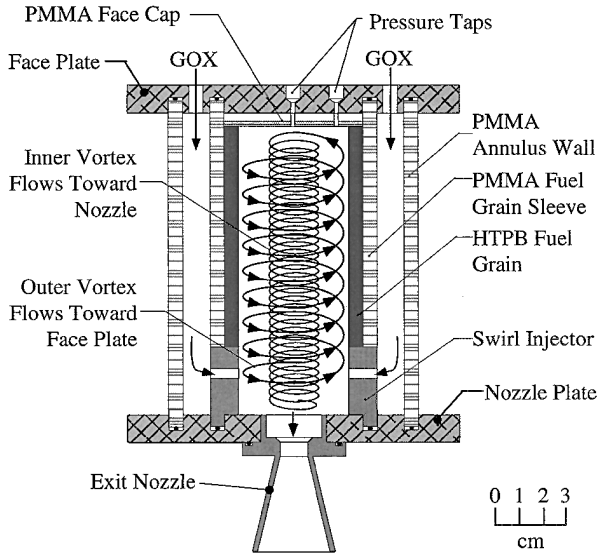

(b) Representation of the pair of vortices

Figure 2.4: Vortex hybrid rocket engine [36]

the oxidizer from directly flowing out of the nozzle, pushing the injected mass flow toward the combustion chamber head end [18, 34, 35, 37].

The flow field structure was confirmed numerically, as can be seen in figure 2.5 that shows the axial velocity field calculated using the finite difference Navier-Stokes (FDNS) code, and by the analytical solution of Majdalani that, assuming at first the flow to be steady, inviscid, incompressible, rotational and axisymmetric, demonstrated the formation of a free vortex in the motor dictated by the inviscid solution of the momentum equation in the tangential direction. Afterwards Majdalani augmented the initial approximations by a viscous correction for the regions where this term cannot be neglected, namely near the centerline of the motor, where a singularity of the free vortex (called mantle) changes the flow structure to a forced vortex, and near the walls, where the condition of no-slip results in a thin boundary

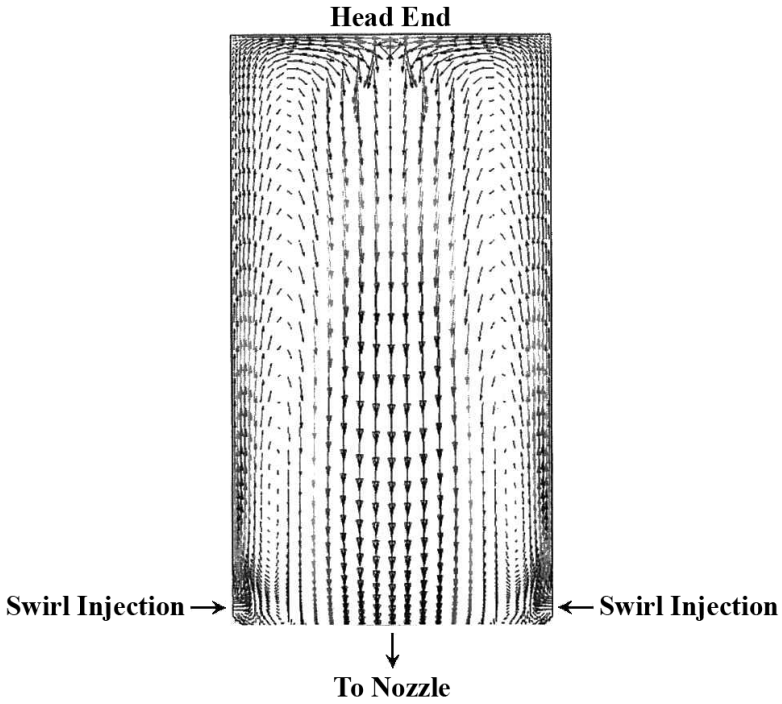

Figure 2.5: Axial velocity field predicted by the FDNS code [36]

layer of null speed in the wall-tangential direction [5, 45].

The flow field derived from the tangential configuration of the injector involves a high increase of the residence time of the gases, due to the particular formation of the pair of vortices that forces the propellant mass to flow through the combustion chamber twice, and of the mixing of the chemical species, because the unburned reactants are transported from the outer to the inner vortex, where the combustion can continue to achieve a better completeness. Moreover the thickness and the growth of the boundary layer is reduced, resulting accordingly in an enhancement of the heat transfer to the solid fuel grain surface and in a very uniform regression rate along the axis of the motor. Another important consequence is the division of the combustion chamber in a high temperature zone and a low temperature region. During the combustion time, the radial pressure gradients cause the hot lower density gases, deriving form the combustion process, to remain in the inner vortex, while the colder and denser gases are transported into the outer vortex. This mechanism results in a relatively low temperature chamber walls, that can have high relevance during the combustion chamber design, with respect to the usable chamber casing materials and their relative thickness [68].

Laboratory experiments have been conducted with GOX and HTPB, and several others proprietary fuel blends, to analyse the fuel regression rate of VHRE of various sizes. HTPB shows a huge increase in the regression rate, that is up to six times faster than those for classical hybrid rockets [36]. With an empirical method, a

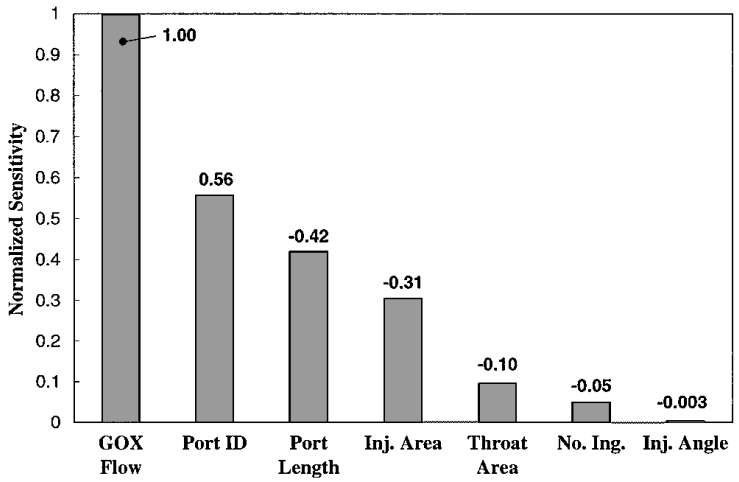

Figure 2.6: Sensitivity of the average regression rate to the independent test variables [36]

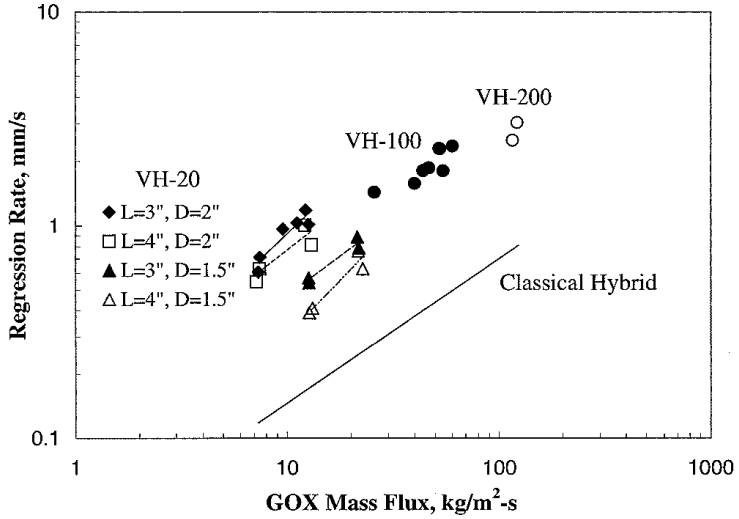

Figure 2.7: Average regression rate behaviour [36]

correlation was developed to characterize the average regression rate as a function of the oxidizer mass flux:

$$\bar{\dot{r}} = 0.193 G_o^{0.54} \tag{2.3}$$

with $\bar{\dot{r}}$ in [mm/s] and G_o in [kg/(m^2 s)]. The empirical power of 0.54 on the oxidizer mass flux ensures a nearly neutral burn and in turn a greatly reduced mixture ratio shifting, because the decrease of the regression rate with the burning time is almost balanced by the increase of the fuel surface area. Since the oxidizer mass flux has a relatively low influence on the average regression rate, a sensitive analysis was conducted to determine the influence of the other test variables. As can be seen in figure 2.6, that shows the results of the statistical analysis, the oxidizer mass flux has, as expected, the largest effect on the average regression rate. However, also the initial fuel port diameter has a strong effect on the increase of

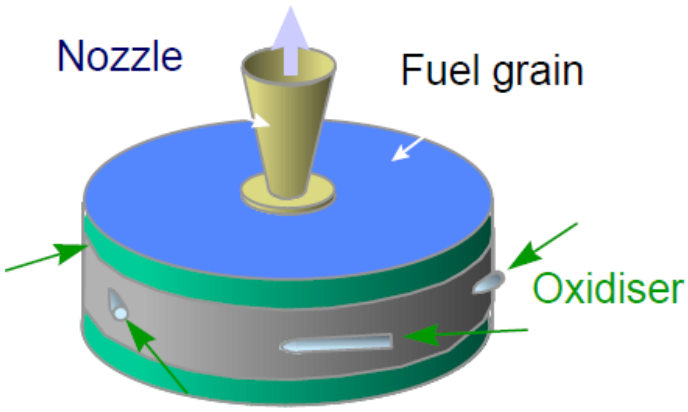

Figure 2.8: Vortex flow pancake hybrid motor [25]

the regression rate, whereas the initial grain port length has an opposite results. Moreover, the inversely proportional dependence on the injection area suggests that high oxidizer jet velocities can be effective in forming stronger vortices in the motor. The remaining independent variables, namely the nozzle throat area, the number of injection holes and the angle of the oxidizer flow injection, have a relatively small and negative effects on the average regression rate.

The average regression rate trend is represented in figure 2.7 for different oxidizer mass fluxes, initial port diameter and initial port length. The classical hybrid rockets regression rate is obtained from the correlation [66]:

$$\bar{\dot{r}} = 0.03 G_o^{0.68} \tag{2.4}$$

with $\bar{\dot{r}}$ in [mm/s] and G_o in [kg/(m^2 s)]. The average regression rate of the VHREs exhibits high values at relatively low oxidizer mass fluxes. This behaviour is caused by the intrinsic nature of the flow field that is established in the motor, because the pair of vortex seems to compress the oxidizer, injected into the combustion chamber, to a thin layer near the solid grain, and thus the fuel surface experiences an higher oxidizer mass flux compared to the overall port size [18].

2.3 Swirl injection in end-burning grains

The tangential oxidizer injection have been used also with an end-burning solid fuel grain. Haag et al. developed the so-called vortex flow pancake (VFP), to be the orbital upper-stage for small satellites [18, 25]. In this configuration two fuel discs that burn in opposite direction are used, with a central circular port in the lower solid fuel grain to allow the hot gases to exit through the nozzle, and a swirl oxidizer injector is placed between them, as shown in figure 2.8.

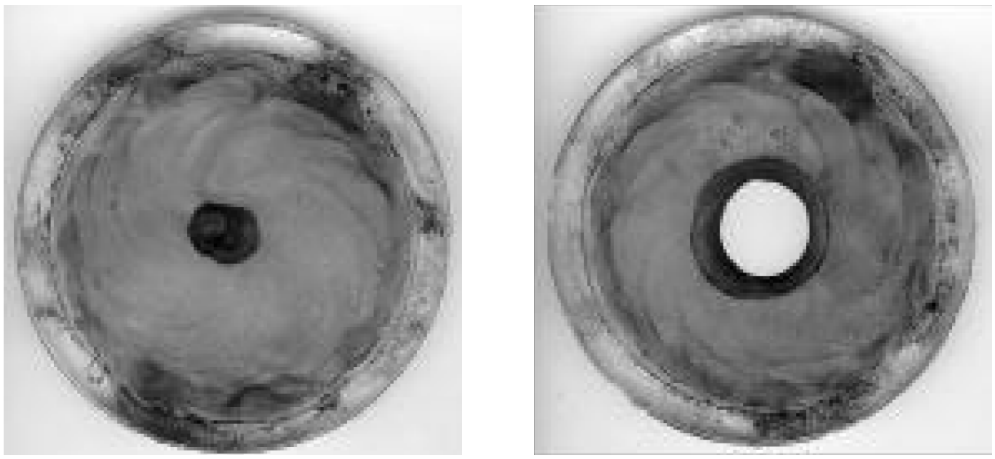

(a) Top fuel disc (b) Bottom fuel disc

Figure 2.9: VFP solid fuel grains after test firing [25]

Since the variable of interest used to measure the performance of VFPs was the fuel mass flow rate, there is no available correlation for the regression rate of this engine configuration. From the performed laboratory tests was found that the fuel mass flow rate is strongly dependent on the oxidizer mass flux. Furthermore, the injection velocity had a large influence on the resultant fuel flow rate, because higher velocities result in a thinner boundary layer, and thus in an enhancement of the heat transfer to the solid fuel grain surface. A dependence of the fuel mass flow rate on the combustion chamber pressure was not found over the tested pressure range. This suggests that the convective heat transfer was higher than the radiative heat transfer, that normally becomes important in classic hybrid combustion at low oxidizer mass fluxes. This effect is caused by the swirling flow field, that greatly increases the convective heat transfer to the solid fuel grain surface. Figure 2.9 shows the effects of the combustion combined with a swirling flow field on the two fuel discs, recovered after the test firing. Moreover, it is important to note that the swirl oxidizer injection applied a negligible residual torque to the motor and that the throat size was not significantly affected by swirling flow, because in the nozzle the streamlines are nearly parallel to the chamber axis due to the high axial velocity acceleration of the hot combustion products.

A similar configuration, named vortex end-burning hybrid (VEBH), with only one fuel disk at the head motor end, was developed by Rice et al. An empirical average regression rate correlation was found for HTPB burning with GOX [18, 61]:

$$\bar{\dot{r}} = 0.4 G_o^{0.62} \tag{2.5}$$

with $\bar{\dot{r}}$ in [mm/s] and G_o in [kg/(m^2 s)]. Compared to classical hybrid rockets using

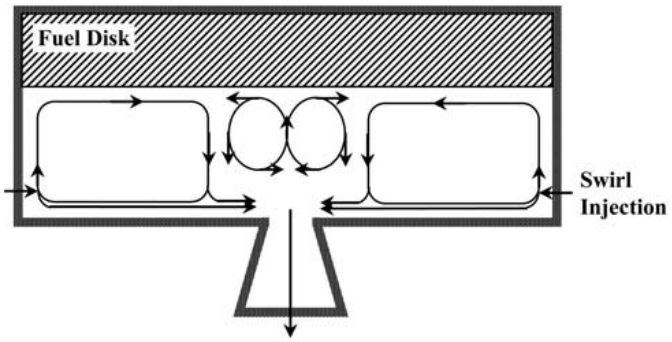

(a) Internal recirculation zone

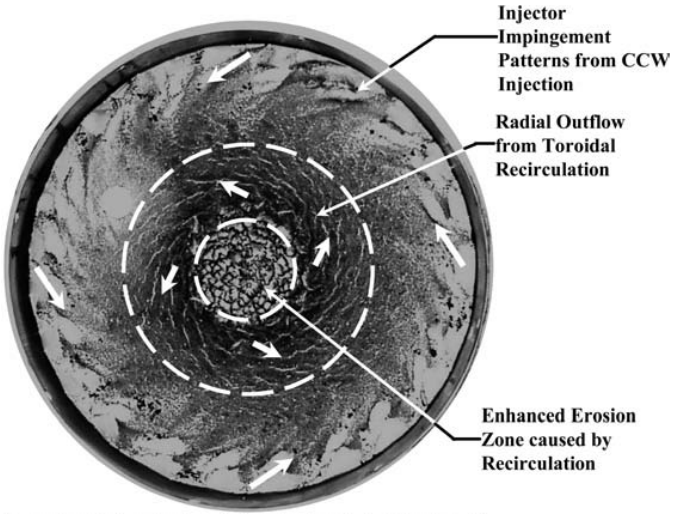

(b) Flow patterns in the solid fuel grain

Figure 2.10: Vortex end-burning hybrid [61]

the same propellant combination, the regression rate of VEBH is more than an order of magnitude greater. But it is necessary to highlight that it is not completely correct to make direct comparison between the two cases, because classical hybrid rockets operate at much higher oxidizer mass fluxes, requiring a large extrapolation of the regression rate correlation (2.4). From the tests carried out, was found that a region of very high regression rate near the center of the fuel grain is present, together with an intermediate zone of apparent counter-rotation, caused by a co-rotating, but radial outflow zone of toroidal recirculation about the combustion chamber axis, as can be seen in figure 2.10, that can lead to fuel residuals.

2.4 Axial injection in end-burning grains

Nagata et al. developed two different types of hybrid rocket motors using an axial injector and end-burning solid fuel grains with a particular geometry. The first one is the so-called dry-towel configuration, that uses a cluster of thin fuel

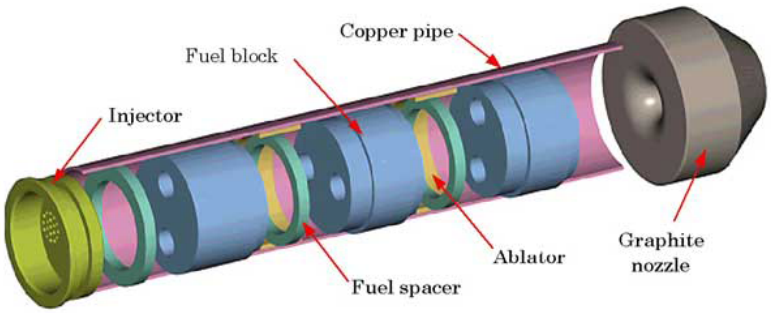

Figure 2.11: Cascaded multistage impinging-jet

tubes. The oxidizer is injected and passes through the tubes without burning, then exits the end of the tubes where is combusted in the diffusion flame on the aft end face of the fuel tube cluster, that burns toward the head end face [18, 56, 59]. One of the first advantages is the usage of an end-burning grain, that exhibits a nearly constant burning surface area, and thus a negligible mixture ratio shifting. Initial tests carried out with a single PE tube burning with GOX showed very high values of regression rate, ranging from 0.5 to 10 mm/s. From these tests was possible to identify a range of oxidizer flow velocities necessary to have an end-burning grain from the aft end face. Beyond the upper critical velocity, that corresponds to the blow-off limit, the diffusion flame is no more established. Below the lower critical velocity the flame flow back into the fuel tube. The velocity range depends on the ambient pressure, where higher pressures permits to have both higher upper and lower critical velocities.

The second configuration developed by Nagata et al. is the so-called cascaded multistage impinging-jet (CAMUI), that consists of several cylindrical grain blocks, with two circular axial ports, separated by a small space, as can be seen in figure 2.11 [18, 57, 58]. Both the grains end faces and the ports surfaces are burned, increasing the total fuel burning surface. A solid fuel grain of PMMA burning with GOX was tested, and was found that the grains end faces burn about twice faster than the grains ports and that the overall combustion efficiency was about 90%. Unfortunately the multiple grain configuration can lead to large fuel slivers, that can be reduced if the burning ports surface reaches the external grain diameter when the upstream face meets the downstream face, and a low volumetric loading.

2.5 Radial injection in end-burning grains

Caravella et al. researched some solutions to increase the regression rate using several unique radial flow hybrid motor concepts [13, 18]. One of the configurations

found, that uses two cylindrical fuel disks and a nozzle located below a circular port in the lower disk, is very similar to the VFP except for the injector, that has an annular design that forces the oxidizer to enter radially the gap between the two fuel disks.

Moreover, the authors tested a motor configuration, with PE as fuel burning with H_2O_2, that injects the oxidizer through a central port in the upper fuel grain into the space between the two disks. The hot gases can flow outside the combustion chamber through a series of nozzle located around the periphery of the lower fuel disk, configuration that provides an approximation of an annular nozzle that can be interesting for practical applications. The regression rate was found to be about three times larger than those measured for a classical hybrid rocket, using the same fuel and oxidizer combination at the same conditions [69], probably due to the three-dimensional flow generated by the radial injector, and generally a higher regression rate was measured for the lower fuel disk:

$$\begin{aligned} \bar{\dot{r}} &= 0.092 G_o^{0.57} \qquad \text{for the upper disk} \\ \bar{\dot{r}} &= 0.1 G_o^{0.7} \qquad \text{for the lower disk} \end{aligned} \tag{2.6}$$

with $\bar{\dot{r}}$ in [mm/s] and G_o in [kg/(m^2 s)]. The local regression rate behaviour on both the fuel disks is very complex, and generally shows a radial profile that is more uniform on the upper fuel disk than on the lower fuel disk. Furthermore a much weaker dependence of the regression rate on the radial location than would be expected was found. In fact, the classical regression rate correlation predicts a decrease in regression rate moving outward toward the disk periphery, due to the increase in flow area at larger radii and thus a decrease in local oxidizer mass flux, whereas as increasing regression rate with an increase in radial location was found from some conducted tests.

Chapter 3

Numerical Investigation

The numerical investigation is carried out with a commercial 3D steady-state computational fluid dynamics code (CFD), to solve the Reynolds-averaged Navier-Stokes equations (RANS) associated with the flow field that characterizes the swirl oxidizer injection type hybrid rocket motor. This type of analysis can really help with the comprehension of the physical phenomena hidden behind the experimental measurement, and so it can be a powerful aid in the preliminary development and testing of the hybrid rocket motors.

First, an incremental analysis of the motor with the swirl injector was conducted, to better understand the role of each component on the flow field. Afterwards, the tangential injector motor was compared with the baseline axial configuration. At last, different configurations were analysed, to study the influence of several parameters on the motor performances, namely:

- Injection swirl number
- Oxidizer mass flux

3.1 Motor Design

A developed and tested laboratory-scale motor is used to obtain a preliminary geometry, that is schematically represented in figure 3.1 [42]. The model consists of different sections:

- Injection plate: the oxidizer can be injected through both an axial and a swirl injector, composed of 12 tangential holes, spatially distributed around the motor axis.
- Combustion chamber: the main part of the motor is composed of a cylindrical grain with a circular port, i.e. a side-burning grain.

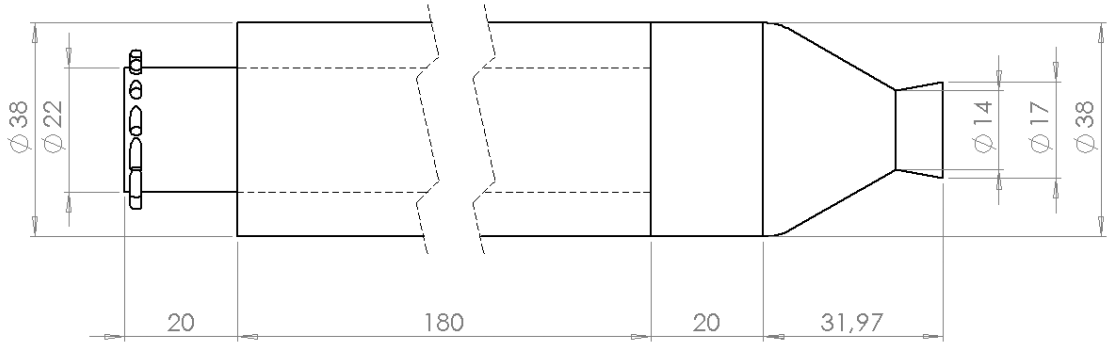

Figure 3.1: Hybrid rocket motor with swirl injector

- Post-combustion chamber: this section is used also as a pick-up point for the parameters of interest, to evaluate the motor performances.

- Nozzle: the expansion of the gases occurs inside a conical nozzle, dimensioned to have a total combustion chamber pressure of 400 000 Pa and a perfect expansion at an atmospheric pressure of 101 325 Pa.

3.2 Simulations Setup

The first step is to find the physically correct boundary conditions for the system. The chosen boundary conditions for all the numerical simulations conducted, as well as the sections where these conditions are applied, are listed here:

- *Inlet* boundary condition: a fixed mass flow at the injector holes surface and at the grain lateral surface is imposed, as well as the temperature of the gases. The mass flow is injected tangentially to the area of the inlets, and the velocity is automatically computed from the following equation:

$$\dot{m} = \varrho A v \tag{3.1}$$

- *Outlet* boundary condition: a fixed pressure at the nozzle outlet section (or at the grain end section for the cases without the nozzle) is chosen.

- *Wall* boundary condition: a no-slip wall condition is applied to all the other surfaces of the motor, to take into account the viscosity of the fluid, and thus the gas immediately next to the wall has the same velocity of the wall, that in this case is null.

$$v = v_w = 0 \tag{3.2}$$

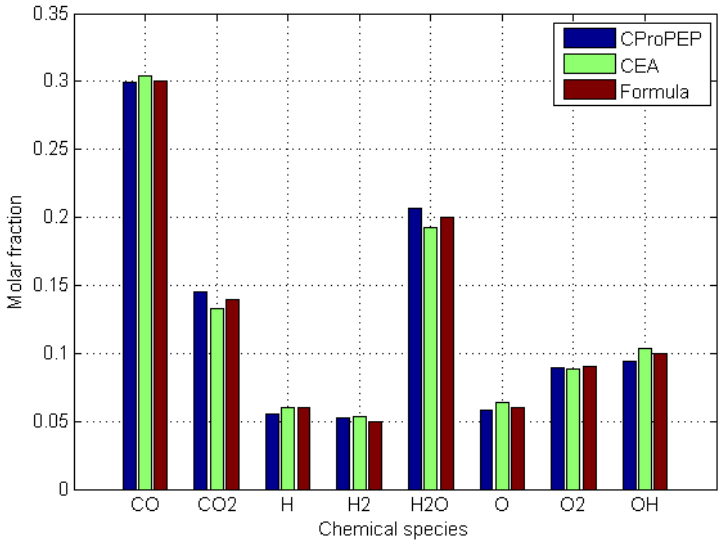

(a) Molar fractions

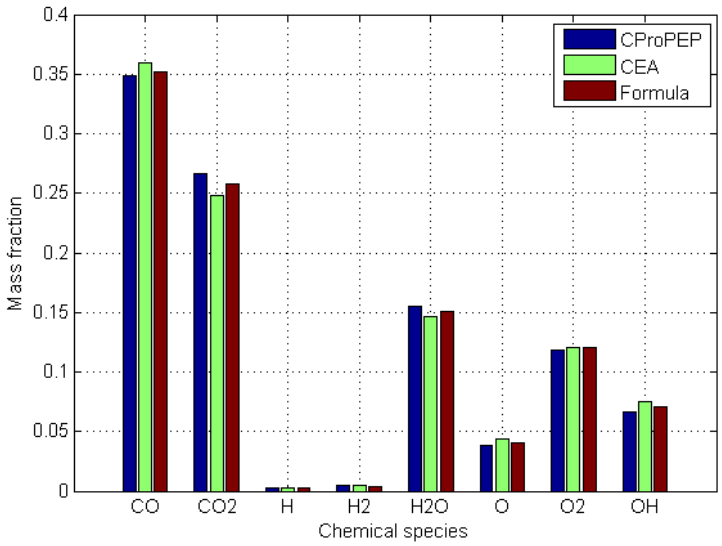

(b) Mass fractions

Figure 3.2: Comparison between combustion formula and thermochemical calculations

Considering the propellant choice, the oxidizer is gaseous O_2 injected at 300 K, while the fuel is HTPB injected already decomposed in butadiene at 1000 K. The chemical reaction of the combustion process is simplified with a single-step formula:

$$56\,O_2 + 11\,C_4H_6 \rightarrow 30\,CO + 14\,CO_2 + 6\,H + 5\,H_2 + 20\,H_2O + 6\,O + 9\,O_2 + 10\,OH$$

The chemical products were chosen using the results of a thermochemical software, like CProPep or CEA, neglecting those with a molar fraction lower than 1×10^{-3}. In figure 3.2 a comparison between the thermochemical software calculations and the formula used in the CFD simulations is presented, for both molar and mass fraction of the reaction products. The combustion process is analysed considering

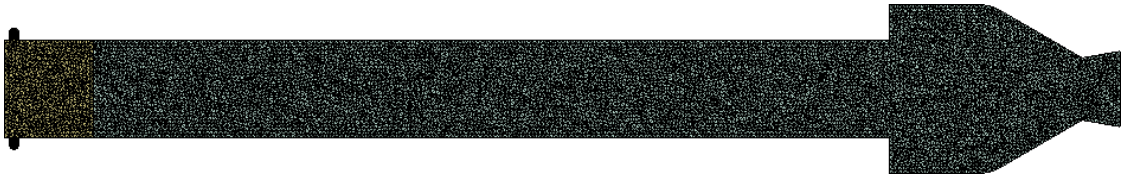

Figure 3.3: View of the entire mesh on a section plane along the motor axis

all the chemical species as ideal gases and using the eddy dissipation model to treat the chemistry of the flame, thus not including chemical kinetics effects. This is a good approximation for typical hybrid rocket motors, where the rate of mixing of the reactants in the turbulent diffusion flame is higher than the chemical reactions rate. This is summarized by a small Damköhler number, that is defined as the ration between the chemical time scale τ_c and the turbulent time scale τ_t:

$$Da = \frac{\tau_c}{\tau_t} \ll 1 \tag{3.3}$$

The turbulence model used in the numerical simulations is the SST $k-\omega$. It was developed to combine the advantages of the $k-\varepsilon$ model with the ones of the $k-\omega$ model, using a blending function to switch between the two models [51]:

- The $k-\omega$ model is used in the near-wall region, because it can accurately simulate the flow in the viscous sub-layer.
- The $k-\varepsilon$ model is used in the free-stream zone, where its accuracy is higher.

The SST $k-\omega$ is a two-equations eddy-viscosity turbulence model, because it includes two extra transport equations to characterize the turbulent properties of the flow, where the first transported variable is the turbulent kinetic energy k, that represents the energy in the turbulence, and the second transported variable is the specific dissipation ω, that represents the scale of the turbulence [15–17].

The mesh type is unstructured with tetrahedral elements, that have a maximum size of 1 mm, chosen after a convergence study. The mesh of the swirl injector case is shown in figure 3.3. The analysis is carried with a steady-state solver and all the methods are second order accurate in space.

3.3 Simulations Matrix

The first step of this numerical investigation is to study the initial motor geometry, increasing the complexity of the system with the addition of each component one by one, to better understand which are the parameters that influence the swirling flow field inside the combustion chamber [9]:

1. *Injection* simulation: only the oxidizer is injected, and the motor geometry is without the post-combustion chamber and the nozzle. This is the most basic case.

2. *Blowing* simulation: also the blowing of the fuel is considered, to account for the increase of the total mass along the motor axis.

3. *Combustion* simulation: now the combustion comes into play, to understand how this chemical process influences the flow field.

4. *Nozzle* simulation: the nozzle is added to the geometry, to include the expansion of the gases, passing from the subsonic region to the supersonic zone of the nozzle.

Afterwards, a comparison between the axial and the swirl injection is made, analysing the qualitative differences in the flow fields and the quantitative ones in the performances.

The central and most important part of this numerical study is focussed on the inspection of the motor performances related to the scaling of several parameters, analysing different configurations. The parameters of interest are:

- Injection swirl number: in order to change the tangential velocity component of the injected oxidizer, and thus the strength of the swirling flow field, the inlet area is varied.

- Oxidizer mass flux: the mass flux of the injected oxidizer is changed gradually, to account for different throttling situations.

The variation of the regression rate with these parameters of interest is computed, starting from the regression rate of the laboratory-scale reference motor, scaling this value with an iterative process accordingly to the wall heat flux, evaluated in the numerical simulations. This approach is possible because, having the same propellant combination and combustion temperature, the regression rate is dependent only on the variation of the wall heat flux:

$$\dot{r} = \frac{\dot{Q}_w}{\varrho_f h_v} \tag{3.4}$$

Chapter 4

Numerical Results

In this chapter the results of the numerical analysis, whose configuration is fully described in chapter 3, are presented and discussed. The same order of the simulation matrix, that was previously presented, is followed, and the results are supported with analytical studies, to better understand the physics controlling the system, and compared with data obtained from several references.

4.1 Incremental Analysis

The swirl injector forces the oxidizer to enter the combustion chamber with a strong tangential velocity component, creating the characteristic helical streamlines that distinguish the flow field of this particular type of hybrid rocket motor. In figure 4.1 the streamlines resulting from the different simulations of the incremental analysis are represented.

Two important parameters to study the swirling flow field in the combustion chamber are:

- The swirl number, that is defined as the ratio between the axial flux of the tangential momentum and the axial flux of the axial momentum:

$$SN = \frac{\int \varrho v_z v_\vartheta r \, \mathrm{d}A}{r_{max} \int \varrho v_z^2 \, \mathrm{d}A} \tag{4.1}$$

- The swirl angle, that is defined as the angle between the streamline and the motor axis (0° means axial flow, while 90° represents fully tangential flow):

$$SA = \arctan\left(\frac{v_z}{v_\vartheta}\right) \tag{4.2}$$

Both these parameters give information about the rotational flow and the way it varies along the motor axis. Their variation along the motor axis is shown in

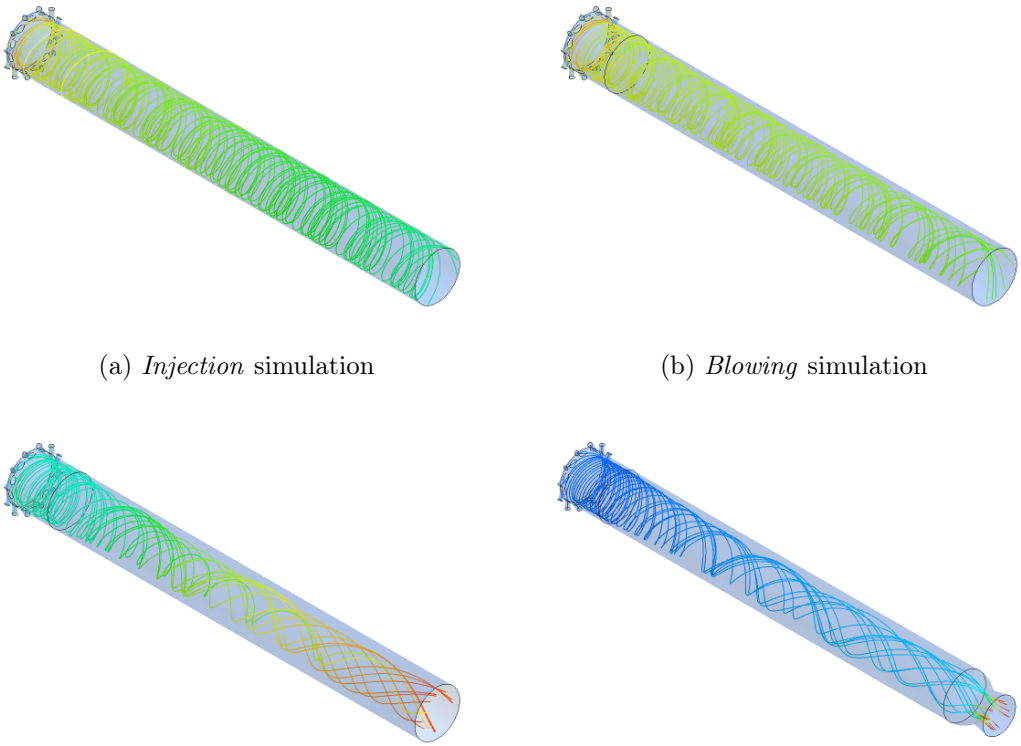

(a) *Injection* simulation

(b) *Blowing* simulation

(c) *Combustion* simulation

(d) *Nozzle* simulation

Figure 4.1: Comparison between the streamlines in the motor for all the simulations

figure 4.2. The decrease of the swirl number, and thus the straightening of the helical flow represented by the reduction of the swirl angle, is caused by two different phenomena, namely the wall friction (that has a minor relevance) and the respect of the continuity equation:

1. *Injection* simulation: the two parameters of interest decrease along the motor axis only slightly, due to the wall friction that decelerates the tangential velocity component.

2. *Blowing* simulation: the decrease of the tangential velocity component is smaller than in the previous case, because the friction is reduced for the presence of the blowing, as can be seen in figure 4.3, but the addition of heated fuel mass involves an increase of the axial velocity component, according to the continuity equation, that in turns causes a reduction of the relative intensity of the rotational flow and a straightening of the streamlines.

3. *Combustion* simulation: the combustion process has the highest influence on the swirl number and on the swirl angle, due to the huge increase of the

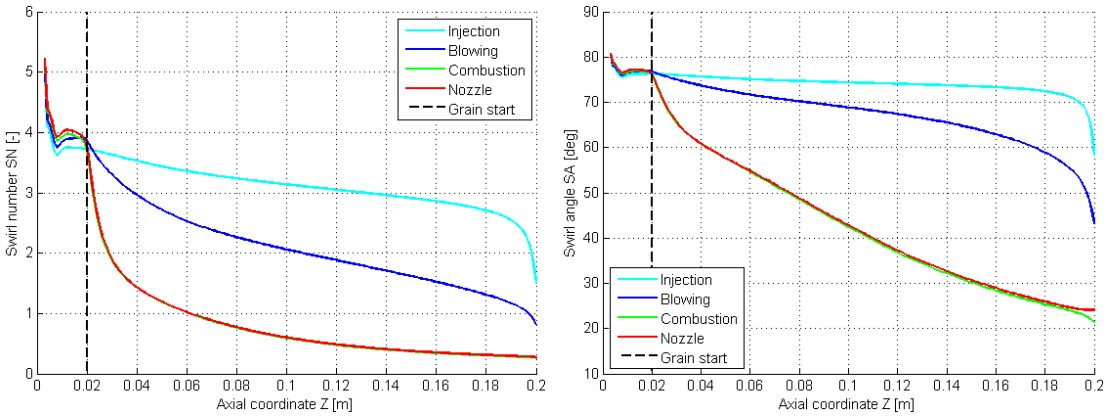

(a) Swirl number (b) Swirl angle

Figure 4.2: Variation of swirl number and swirl angle along the motor axis

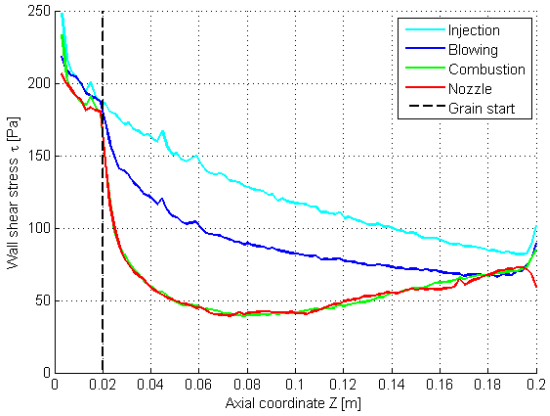

Figure 4.3: Variation of wall shear stress along the motor axis (variable is computed over a line on the grain surface)

temperature of the gases that leads to an acceleration of the flow in the axial direction, to respect the continuity equation.

4. *Nozzle* simulation: the results of this case are mostly identical to those of the previous simulation, because the addition of the nozzle to the geometry does not change the flow field in the combustion chamber, but only expands and accelerates the gas passing through it.

The trends of axial and tangential velocity components, along the motor axis, are represented in figure 4.4.

An analytical study, conducted by Bellomo et al., shows that a forced vortex is imposed to the flow field in the combustion chamber of the hybrid motor and describes the centrifugal effect caused by the rotation of the flow [9]. This result can be obtained analysing the Navier-Stokes equations, neglecting the gravity and the normal viscous terms.

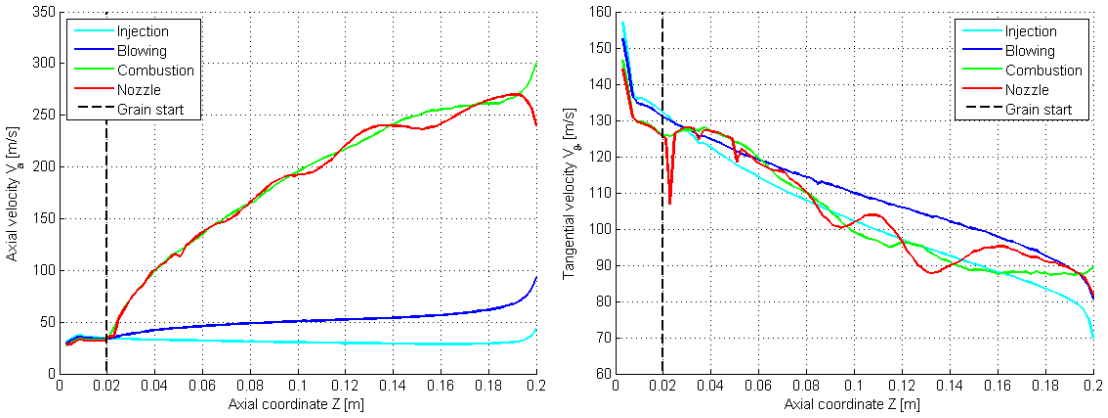

(a) Axial velocity (b) Tangential velocity

Figure 4.4: Variation of axial and tangential velocity components along the motor axis (variables are computed over an axial line 1 mm away from the grain surface)

The momentum balance in the tangential direction, expressed in cylindrical coordinates, can be written as:

$$\varrho\left(\frac{\partial v_\vartheta}{\partial t}+v_r\frac{\partial v_\vartheta}{\partial r}+\frac{v_\vartheta}{r}\frac{\partial v_\vartheta}{\partial \vartheta}+v_z\frac{\partial v_\vartheta}{\partial z}+\frac{v_r v_\vartheta}{r}\right)=-\frac{1}{r}\frac{\partial p}{\partial \vartheta} + \mu\left[\frac{1}{r}\frac{\partial}{\partial r}\left(r\frac{\partial v_\vartheta}{\partial r}\right)+\frac{1}{r^2}\frac{\partial^2 v_\vartheta}{\partial \vartheta^2}+\frac{\partial^2 v_\vartheta}{\partial z^2}-\frac{v_\vartheta}{r^2}+\frac{2}{r^2}\frac{\partial v_r}{\partial \vartheta}\right] \quad (4.3)$$

Considering the following hypothesis, some important simplifications can be introduced in last equation:

- Steady state flow
- Axis-symmetry, and thus null derivative over the tangential direction
- Negligible variation of tangential velocity component in the longitudinal direction
- Negligible radial velocity component compared to axial and tangential velocity components

Accordingly, equation (4.3) becomes:

$$\frac{1}{r}\frac{\partial}{\partial r}\left(r\frac{\partial v_\vartheta}{\partial r}\right)-\frac{v_\vartheta}{r^2}=0 \quad (4.4)$$

whose only possible solution is the forced vortex:

$$\omega r = v_\vartheta \quad (4.5)$$

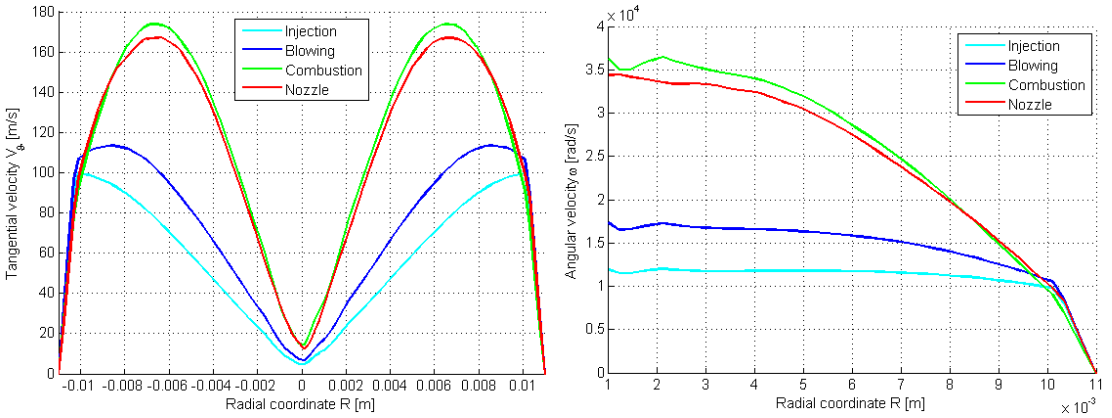

(a) Tangential velocity (b) Angular velocity

Figure 4.5: Variation of tangential velocity and angular velocity components along the motor diameter (variables are computed over a diametric line at middle grain)

The forced vortex flow field was confirmed from the CFD simulations. This is mathematically true only when the oxidizer is injected into the combustion chamber, whereas the increase of the system complexity causes the results to be far away from the theoretical ones. Considering the addition of the fuel, through the blowing from the solid grain walls, varies the solution only slightly, contrariwise taking into account also the combustion process makes the mathematical solution no longer valid, as can be seen in figure 4.5, even though the flow field is still in agreement with the analytical result, at least from a qualitative point of view.

Considering cylindrical coordinates, the momentum balance in the radial direction is the following:

$$\varrho\left(\frac{\partial v_r}{\partial t}+v_r\frac{\partial v_r}{\partial r}+\frac{v_\vartheta}{r}\frac{\partial v_r}{\partial \vartheta}+v_z\frac{\partial v_r}{\partial z}-\frac{v_\vartheta^2}{r}\right)=-\frac{\partial p}{\partial r} + \mu\left[\frac{1}{r}\frac{\partial v_r}{\partial r}+\frac{1}{r^2}\frac{\partial^2 v_r}{\partial \vartheta^2}+\frac{\partial^2 v_r}{\partial z^2}-\frac{v_r}{r^2}-\frac{2}{r^2}\frac{\partial v_\vartheta}{\partial \vartheta}\right] \tag{4.6}$$

Introducing the same hypothesis, and thus the same simplifications, previously applied to the momentum balance in the tangential direction, equation (4.6) can be written as:

$$\varrho\frac{v_\vartheta^2}{r}=\frac{\partial p}{\partial r} \tag{4.7}$$

Moreover, considering an ideal gas and a forced vortex, it is possible to obtain:

$$\varrho\frac{v_\vartheta^2}{r}=\frac{\partial p}{\partial r}=\frac{\omega^2 r M_m p}{R_u T} \tag{4.8}$$

For constant molecular mass and temperature along the radial direction, the previous

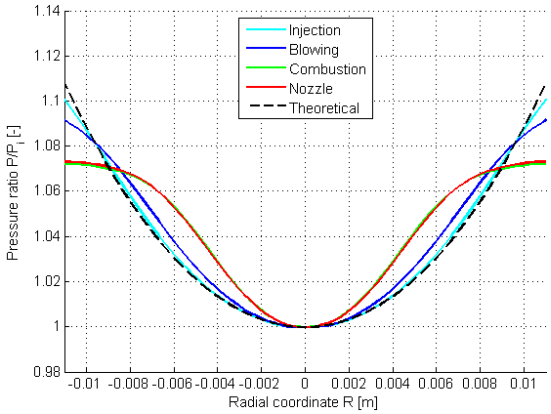

Figure 4.6: Variation of pressure ratio along the motor diameter (variable is computed over a diametric line at middle grain)

equation can be integrated between the center of the motor ($r = 0$, $p = p_i$ and $\varrho = \varrho_i$) and a generic radial position (r, p and ϱ):

$$\ln \frac{p}{p_i} = \frac{\omega^2 r^2 M_m}{2R_u T} \tag{4.9a}$$

$$\ln \frac{\varrho}{\varrho_i} = \frac{\omega^2 r^2 M_m}{2R_u T} \tag{4.9b}$$

$$p(r) = p_i \exp\left(\frac{\omega^2 r^2 M_m}{2R_u T}\right) \tag{4.10a}$$

$$\varrho(r) = \varrho_i \exp\left(\frac{\omega^2 r^2 M_m}{2R_u T}\right) \tag{4.10b}$$

The equations (4.9) and (4.10) describe the centrifugal effects caused by the rotation of the flow, that pushes the fluid toward the wall of the combustion chamber. The radial pressure gradient was numerically confirmed by the CFD simulations, with accurate results for the *injection* simulation. As for the forced vortex solution, the increase of the system complexity causes the results to be far away from the theoretical one, maintaining, however, the qualitative trend, as shown in figure 4.6.

4.2 Comparison Between Axial and Swirl Injection

The comparison between the axial injection and the swirl one is carried out analysing the same motor geometry with two different injectors. The streamlines in the hybrid rocket motor are the first and trivial difference. Using the axial injector, in the combustion chamber the formation of streamlines that are parallel

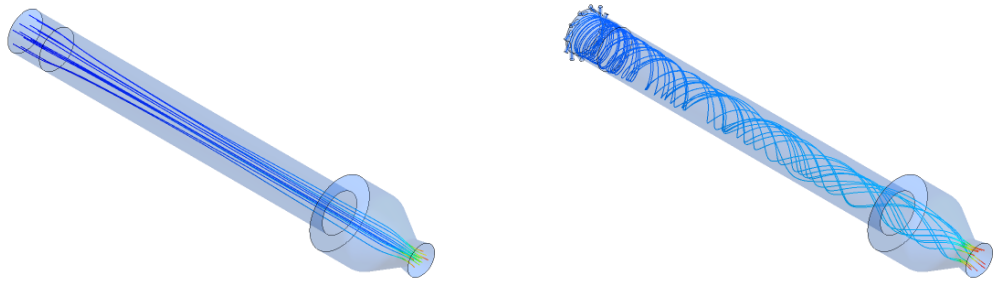

(a) Axial injection simulation (b) Swirl injection simulation

Figure 4.7: Comparison between the streamlines in the motor for both the simulations

to the motor axis occurs, whereas the swirl injector involves the developing of the characteristic helical streamlines, that are represented in figure 4.7.

The real primary difference is that the injection of the oxidizer using a swirl injector, that forces the gaseous oxygen to enter the combustion chamber with a strong tangential velocity component, enhances the mixing of the reacting chemical species involved in the combustion process, as can be seen in figure 4.8, ensuring a more effective burning process, that in turn leads to an increase of the characteristic velocity c^* and of the combustion efficiency η. Moreover, the rotational flow field allows to obtain a better mixing of the chemical products, as represented in figure 4.9, and thus a greater heating of the cold gases in the central core of the combustion chamber. The zone where the hot product gases are present is, thus, wider in the swirl injector case than in the axial one, where the temperature gradient is really steep, as can be seen in figure 4.10. Furthermore, remembering the equations (4.10) that describe the centrifugal effect caused by the oxidizer swirl injection, it is important to underline that another difference is the presence of a pressure gradient in the combustion chamber, represented in figure 4.11.

This qualitative considerations are translated in quantitative terms with the plots in figure 4.12 and 4.13, that represent the variation of the discussed variables along different radial sections of the combustion chamber, for the axial injection simulation and for the swirl injection one. The pressure gradient is less pronounced near the nozzle than near the injector because, given the same angular velocity of the gases, the variation of pressure from the grain surface to the motor axis is lower when the fluid is hotter, and thus has lower density, and when the molar mass is lower, because of inertial forces [10]. This behaviour is represented in figure 4.14, where the pressure ratio for different radial sections of the motor is plotted. It is possible to see that the post combustion chamber is the zone where the radial

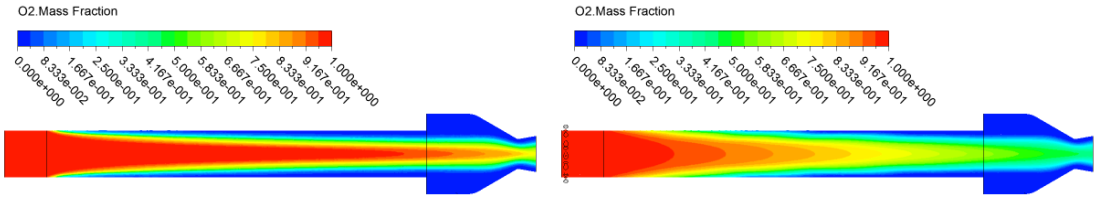

(a) Axial injection simulation (b) Swirl injection simulation

Figure 4.8: Comparison between the oxidizer mass fraction in the motor for both the simulations

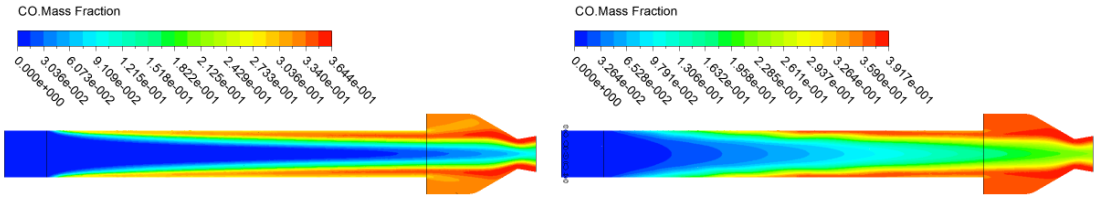

(a) Axial injection simulation (b) Swirl injection simulation

Figure 4.9: Comparison between the products mass fraction in the motor for both the simulations

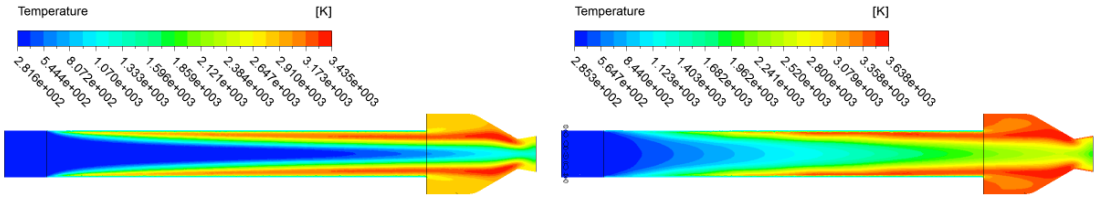

(a) Axial injection simulation (b) Swirl injection simulation

Figure 4.10: Comparison between the temperature in the motor for both the simulations

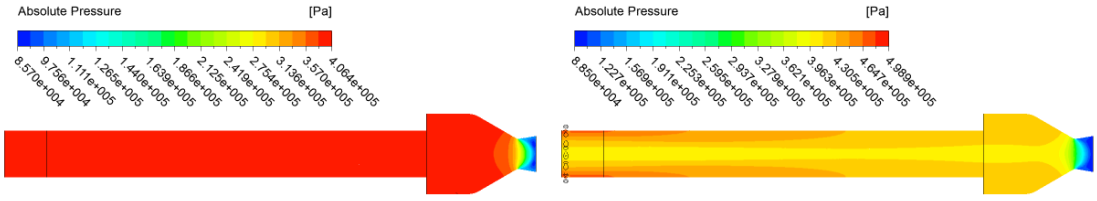

(a) Axial injection simulation (b) Swirl injection simulation

Figure 4.11: Comparison between the pressure in the motor for both the simulations

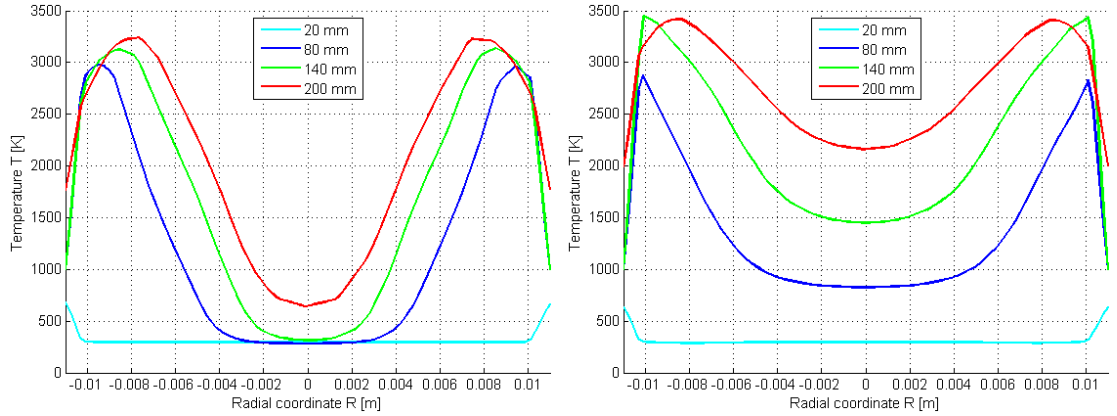

(a) Axial injection simulation (b) Swirl injection simulation

Figure 4.12: Variation of temperature along the motor diameter (variable is computed over several diametric line)

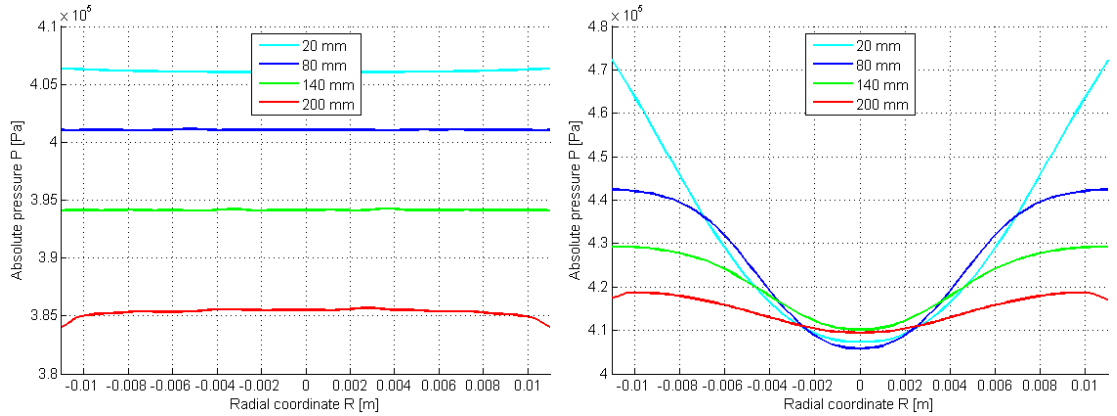

(a) Axial injection simulation (b) Swirl injection simulation

Figure 4.13: Variation of pressure along the motor diameter (variable is computed over several diametric line)

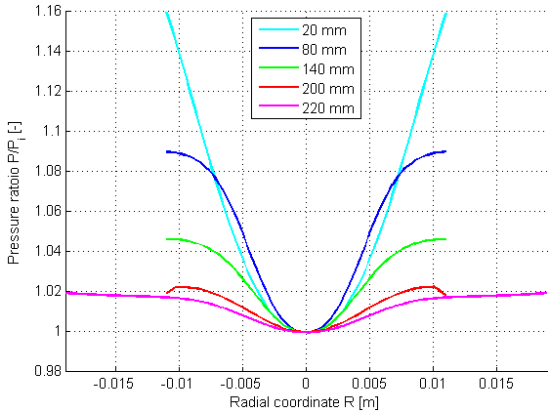

Figure 4.14: Variation of pressure ratio along the motor diameter (variable is computed over several diametric line)

pressure gradient is smaller and thus the pressure is more homogeneous, making this region the perfect place to position a pressure measurement point.

4.2.1 Motor Performance

In order to evaluate the increase of the motor performance, it is necessary to consider two parameters:

- The characteristic velocity c^*, that is computed with two different relations:

$$c^* = \frac{p_c c_d A_t}{\dot{m}} \tag{4.11a}$$

$$c^* = \sqrt{\frac{\frac{R_u}{M_m} T_c}{\gamma \left(\frac{2}{\gamma + 1} \right)^{\frac{\gamma+1}{\gamma-1}}}} \tag{4.11b}$$

- The combustion efficiency η, that is defined as:

$$\eta = \frac{c^*_{sim}}{c^*_{th}} \tag{4.12}$$

The discharge coefficient c_d accounts for the reduction of the nozzle throat area caused by the presence of the swirling component of the flow, due to the centrifugal forces opposing the fluid that approaches the nozzle throat. This effect was theoretically examined by several authors [2, 21, 22, 44]. The discharge coefficient for the axial case is approximately taken as equal to 1, and for the swirl case is equal to 0.98. The value of this parameter is computed comparing the pressure in the combustion chamber between the axial configuration and the swirl one:

$$c_d = \frac{p_{c_{ax}}}{p_{c_{sw}}} \tag{4.13}$$

The process for the evaluation of the discharge coefficient is better explained in section 4.5.

The values of these performances parameters, for both the simulations, are represented in figure 4.15 and summarized in table 4.1. It is possible to note that there is a difference in the value of the two parameters, depending on the expression used. This is due to the hypothesis of isentropic, uniform and monodimensional flow through the nozzle, that is necessary to pass from equation (4.11a) to equation (4.11b). In the simulation with axial injection the difference is bigger than

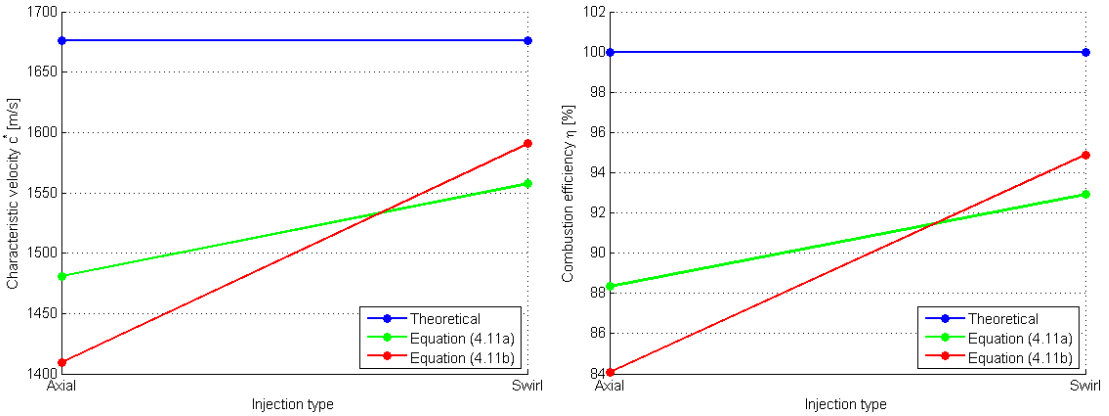

(a) Characteristic velocity (b) Combustion efficiency

Figure 4.15: Comparison of the propulsive performance of the motor between axial injection and swirl injection

Table 4.1: Comparison of the propulsive performance of the motor between axial injection and swirl injection

Case	c_d [−]	c_1^* [m/s] (4.11a)	c_2^* [m/s] (4.11b)	η_1 [%]	η_2 [%]
Axial injection	1	1481	1409	88.3	84.1
Swirl injection	0.972	1558	1591	92.9	94.9

with the swirl injector, because in the former case the oxidizer and the fuel flow parallel to the motor axis, producing the typical stratified flow field, whereas in the latter case the rotational flow field enhances the mixing of the gases, thus reducing the distance from the ideal case. Moreover, considering the hypothesis of monodimensional flow, the swirling flow is greatly reduced in the nozzle, to respect the continuity equation, as can be seen in figures 4.16 and 4.17. In conclusion, the swirl injection results in an increase of the characteristic velocity, and thus of the combustion efficiency, of the 5.2%, using the first definition of the characteristic velocity (4.11a), for several reasons:

- It enhances the mixing of the reacting chemical species, ensuring a more effective burning process.
- It allows to obtain a better mixing of the chemical products, and thus a greater heating of the cold gases in the central core.
- The centrifugal forces push the flame near the solid grain surface, increasing the wall heat flux.
- The additional tangential velocity component increases the effective velocity of the oxidizer mass flowing onto the solid fuel wall.

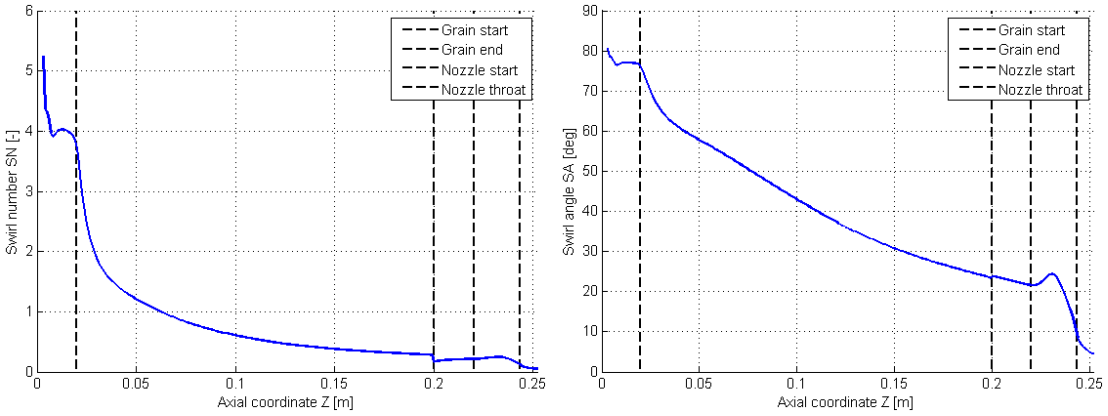

(a) Swirl number (b) Swirl angle

Figure 4.16: Variation of swirl number and swirl angle along the motor axis

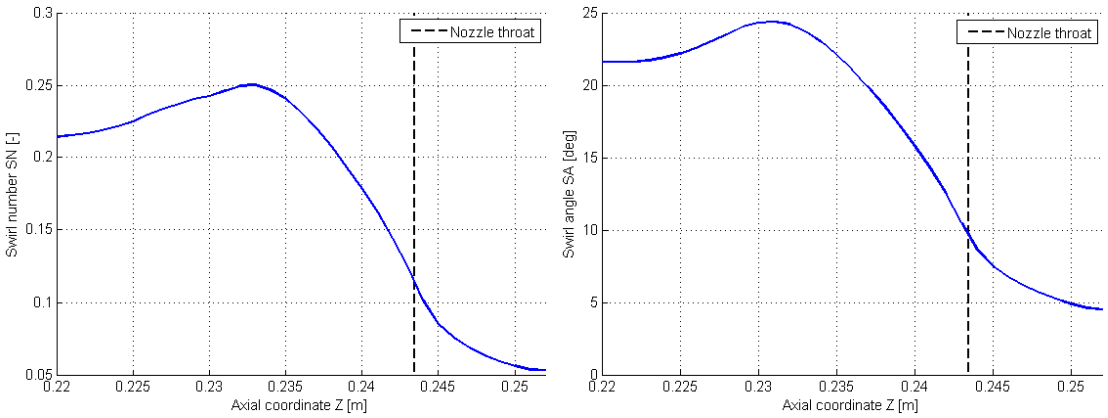

(a) Swirl number (b) Swirl angle

Figure 4.17: Variation of swirl number and swirl angle along the nozzle

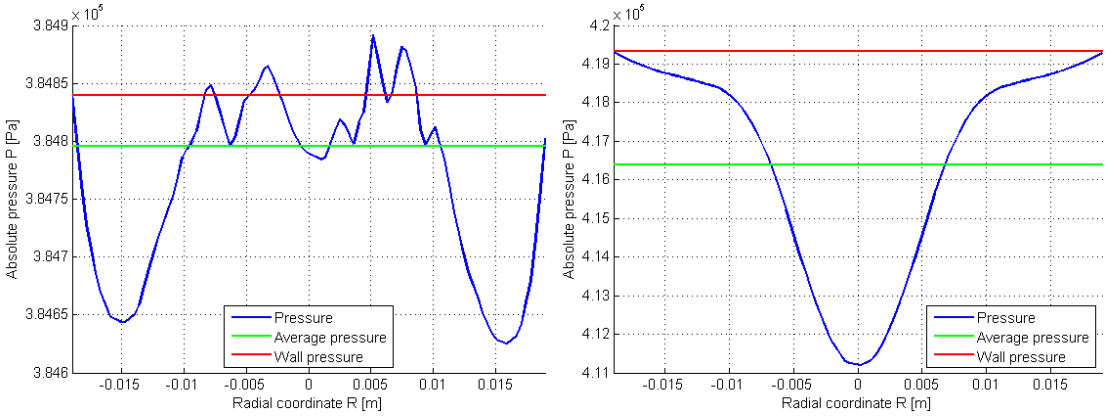

(a) Axial injection simulation (b) Swirl injection simulation

Figure 4.18: Comparison of the pressure measures between axial injection and swirl injection (variable is computed over a diametric line at post-combustion chamber)

Table 4.2: Comparison of the pressure measures between axial injection and swirl injection

Case	P_{ave} [Pa]	P_w [Pa]	Δ [%]
Axial injection	384796	384840	0.01
Swirl injection	416378	419323	0.71

Furthermore, the measurement point of the pressure plays an important role in the evaluation of the performance parameters. The previous values were obtained using the average post-combustion chamber pressure but, as represented in figure 4.18, the measure of the pressure at the wall of the post-combustion chamber, as is common in an experimental setup, leads to an overestimation of the performance of the motor. However, the difference is small, that is 0.01% for the axial injection and 0.71% for the swirl injection, as summarized in table 4.2.

4.3 Scaling of Injection Swirl Number

In this section the effects of the scaling of the injection swirl number are analysed. Before presenting and discussing the results of the numerical simulations, it is important to remember the definition of the geometric swirl number, already introduced in chapter 2, which comes from the conservation of the momentum following the convention proposed by Beer and Chigier [7]. This approach permits to use only geometrical parameters, namely the dimensions of the injection plate, that are easily obtainable also during an experimental test, in order to compare different situations, without the need for specific measurements of local fluid unknowns, that require a more complicated instrumentation:

$$SN_g = \frac{(r_{inj} - r_{hol})r_{inj}}{N_{hol}r_{hol}^2} \tag{4.14}$$

The geometric swirl number was varied changing the dimension of the injection holes r_{hol}, and thus the inlet area, maintaining the number of holes fixed. Three different configuration were studied:

- $SN_g = 4.39$
- $SN_g = 5.97$
- $SN_g = 9.17$

The streamlines in the combustion chamber of the cases studied, which are plotted in figure 4.19, explicate that the increase of the geometric swirl number

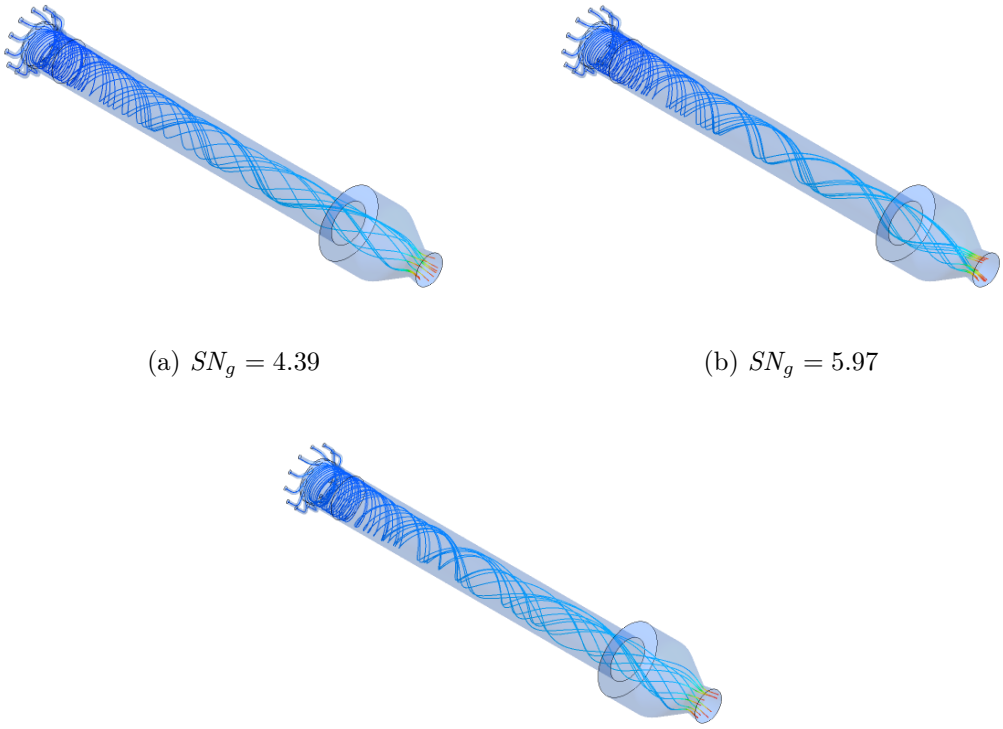

(a) $SN_g = 4.39$

(b) $SN_g = 5.97$

(c) $SN_g = 9.17$

Figure 4.19: Comparison between the streamlines in the motor for all the simulations

leads to a helical flow field with a higher pitch, and thus to a stronger recirculating flow field. This behaviour can also be represented by the variation of the swirl number and the swirl angle, as can be seen in figure 4.20 and figure 4.21. The fast decrease of the swirl number, along the hybrid motor axis, reduces the influence of the geometric swirl number on the local swirl number, that experiences a small variation due to the change of the injection conditions.

It is important to note that the variation of the injection swirl number does not affect the shape of the flow field and of its describing parameters, but it only changes the magnitude of these variables. The temperature in the combustion chamber increases with the geometric swirl number, as represented in figure 4.22, because a stronger rotational flow field enhances the mixing of the reactants, promoting a more complete combustion. The axial velocity component increases only slightly with the geometric swirl number, as can be seen in figure 4.23, to respect the continuity equation, because of the increase of the temperature and of the addition of fuel due to an enhancement of the regression rate, that will be discussed in the next paragraph. The growing of the tangential velocity component, that is represented in figure 4.24, is the obvious result of the geometric swirl number

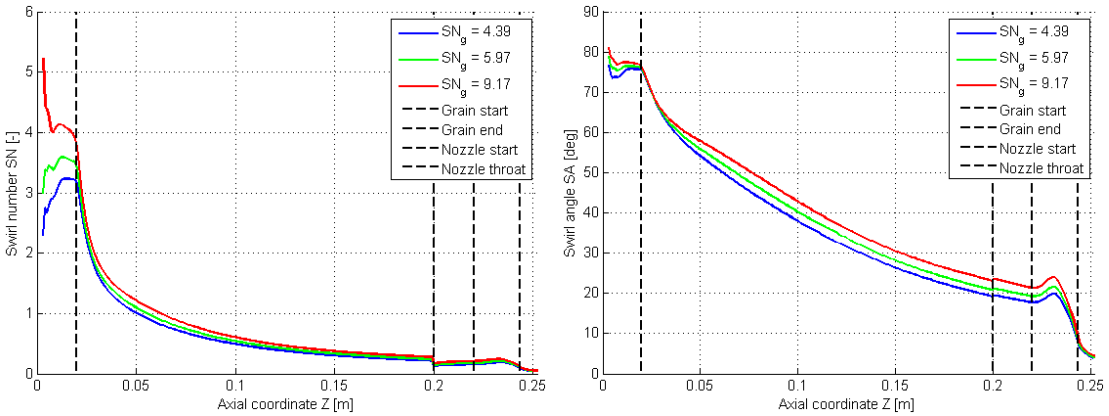

(a) Swirl number (b) Swirl angle

Figure 4.20: Variation of swirl number and swirl angle along the motor axis

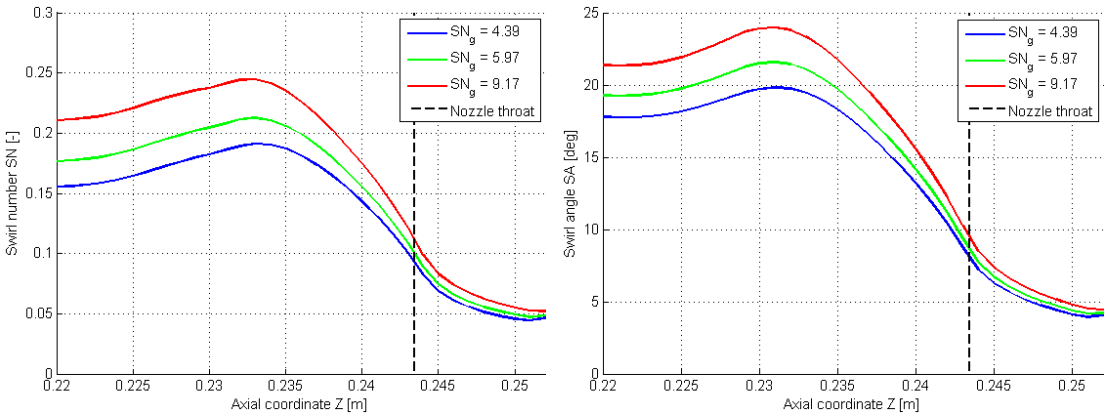

(a) Swirl number (b) Swirl angle

Figure 4.21: Variation of swirl number and swirl angle along the nozzle

increase. The enhancement of the pyrolysis of the solid fuel also leads to an increase of the combustion chamber pressure, as can be seen in figure 4.25.

The variation of the injection swirl number has an important impact on the regression rate of the motor, because the increase of the geometric swirl number leads to an enhancement of this fundamental motor parameter. This is the main reason that makes the use of a swirl injector with a side-burning grain a viable way to solve the principal inherent problem of the hybrid rocket motors, namely the low regression rate. As can be seen in figure 4.26, the spacial averaged regression rate of the hybrid motor, studied in the numerical simulations, is increasing with the geometric swirl number of the injector, as well as the local regression rate, and thus the mixture ratio is decreasing, as represented in figure 4.27. It is possible to see that the simplified model of the numerical simulations, that approximate the local regression rate with its spacial averaged value, is not satisfactory to predict

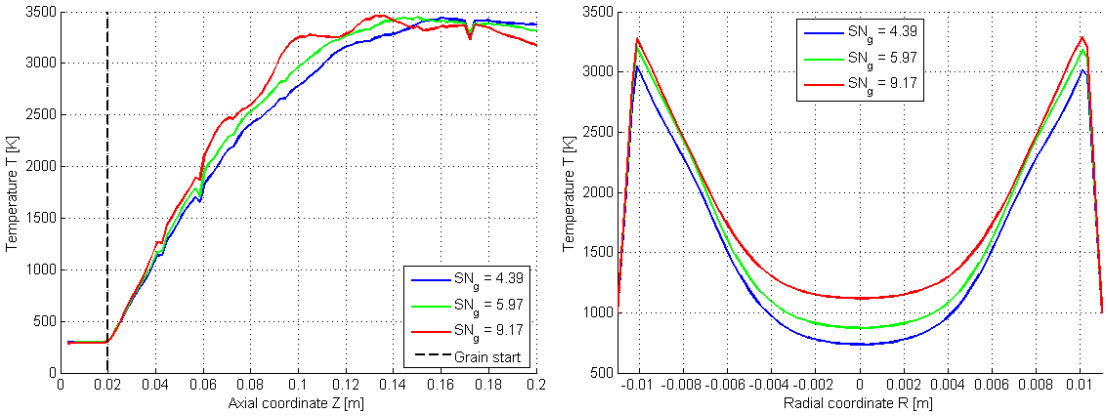

(a) Axial variation (b) Radial variation

Figure 4.22: Variation of temperature (variable is computed over an axial line 1 mm away from the grain surface and over a diametric line at middle grain)

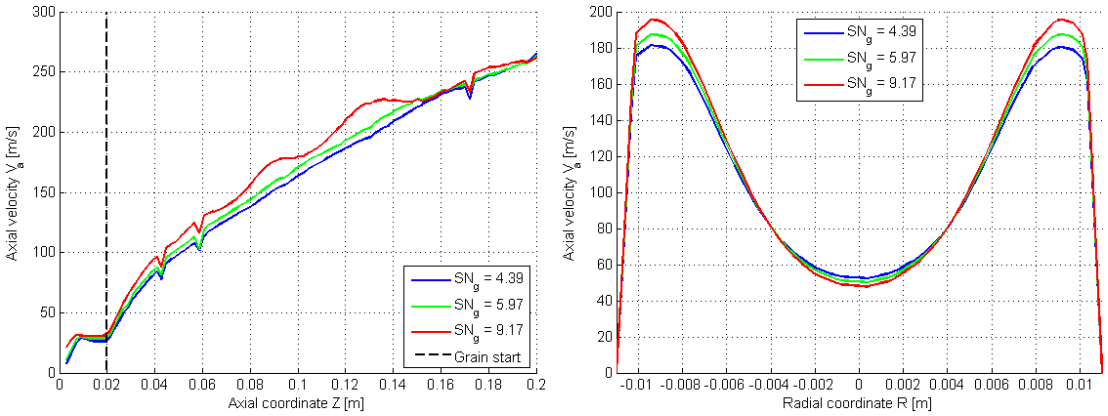

(a) Axial variation (b) Radial variation

Figure 4.23: Variation of axial velocity (variable is computed over an axial line 1 mm away from the grain surface and over a diametric line at middle grain)

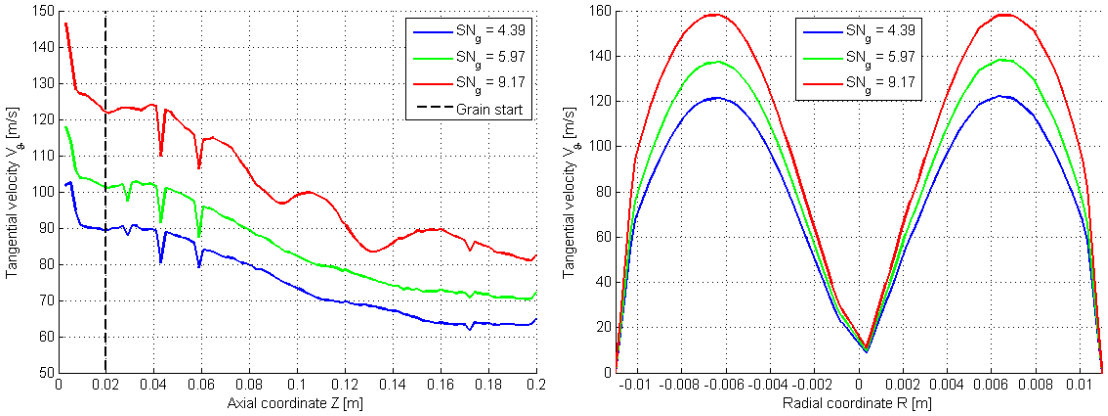

(a) Axial variation (b) Radial variation

Figure 4.24: Variation of tangential velocity (variable is computed over an axial line 1 mm away from the grain surface and over a diametric line at middle grain)

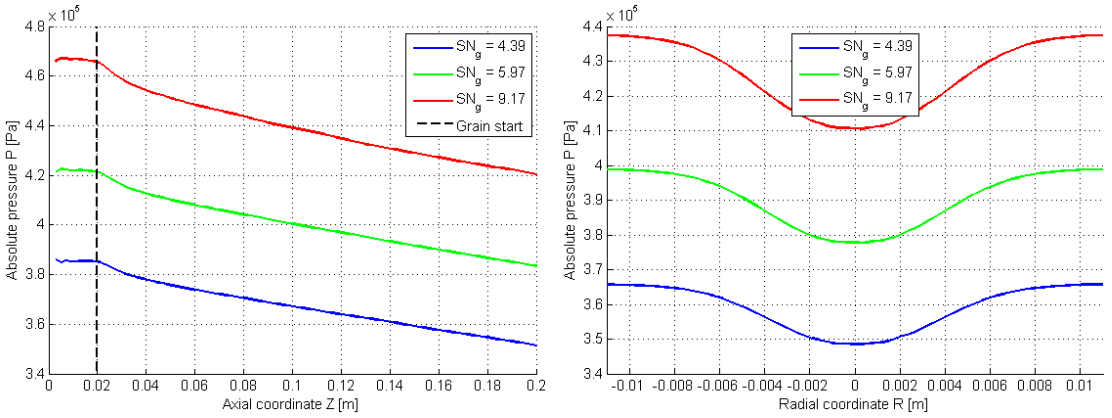

(a) Axial variation (b) Radial variation

Figure 4.25: Variation of pressure (variable is computed over an axial line 1 mm away from the grain surface and over a diametric line at middle grain)

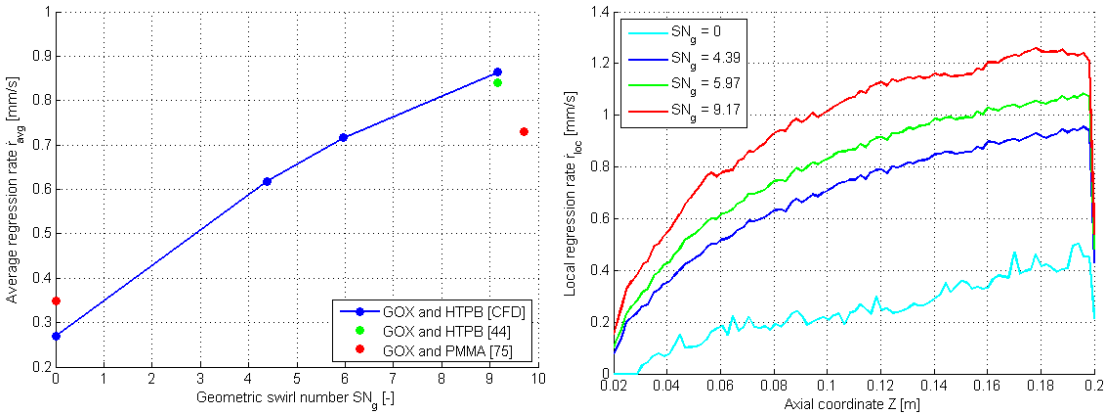

(a) Average regression rate (b) Local regression rate

Figure 4.26: Variation of average and local regression rate with geometric swirl number

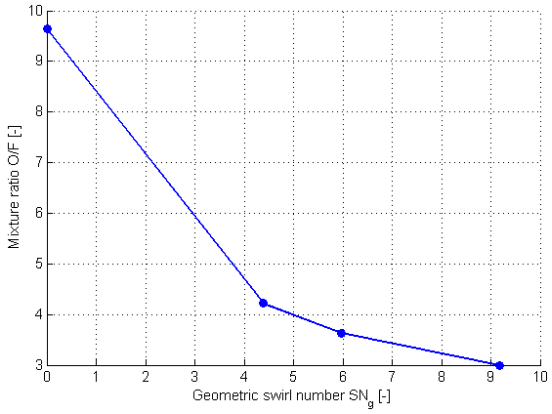

Figure 4.27: Variation of mixture ration with geometric swirl number

Table 4.3: Variation of average regression rate and mixture ration with geometric swirl number

Case	$\bar{\dot{r}}$ [mm/s]	O/F [−]
$SN_g = 0$	0.269	9.64
$SN_g = 4.39$	0.619	4.22
$SN_g = 5.97$	0.716	3.63
$SN_g = 9.17$	0.864	3

Table 4.4: Variation of the propulsive performance of the motor with geometric swirl number

Case	c_d [−]	c_1^* [m/s] (4.11a)	c_2^* [m/s] (4.11b)	η_1 [%]	η_2 [%]
$SN_g = 4.39$	0.976	1416	1466	89.7	92.9
$SN_g = 5.97$	0.975	1496	1528	92.3	94.3
$SN_g = 9.17$	0.972	1563	1588	93.3	94.8

correctly the variation of the regression rate along the motor axis, because several experimental analysis showed that at the leading edge of the solid grain there is a zone of very high local regression rate, due to the impingement of the oxidizer mass flow striking onto the fuel surface. The values of the average regression rate and of the mixture ratio for the different geometric swirl numbers are summarized in table 4.3, where can be easily compared.

4.3.1 Motor Performance

The values of the performances parameters, that is the characteristic velocity and the combustion efficiency, for all the simulations, are represented in figure 4.28 and summarized in table 4.4. As in the comparison between the axial case and the swirl one, it is possible to note that there is a difference in the value of the two parameters, depending on the expression used. For all the three geometric swirl numbers considered, the discharge coefficient of the nozzle is really close to 1, that implies a negligible fictitious shrinkage of the nozzle throat area, due to the choking effect of the swirling component of the flow in the combustion chamber of the hybrid motor. The swirl injection results in an enhance of the motor performance of the 5.6%, using the first definition of the characteristic velocity (4.11a), increasing the geometric swirl number from 4.39 to 5.97, and of the 10.4% going from 4.39 to 9.17.

Moreover, the measure of the pressure at the wall of the post-combustion chamber leads to an overestimation of the performance of the motor, as can be seen in figure 4.29. However, the difference is small, as summarized in table 4.5.

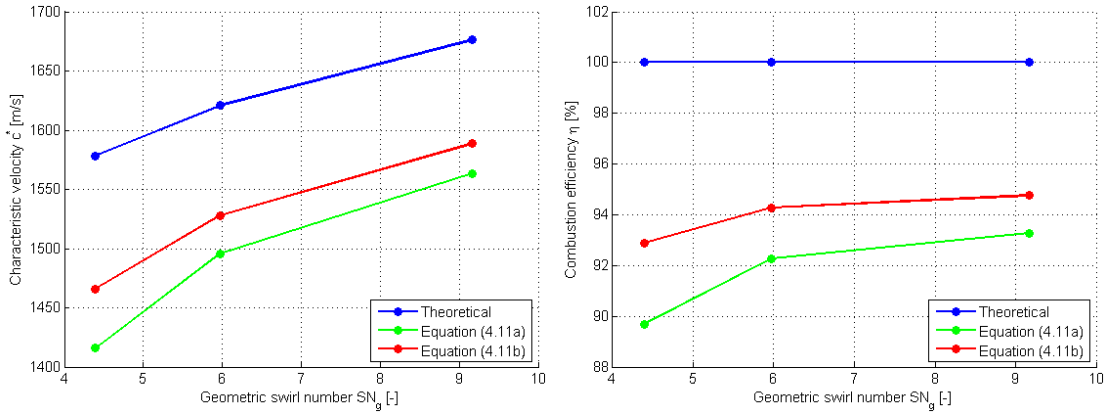

(a) Characteristic velocity (b) Combustion efficiency

Figure 4.28: Variation of the propulsive performance of the motor with geometric swirl number

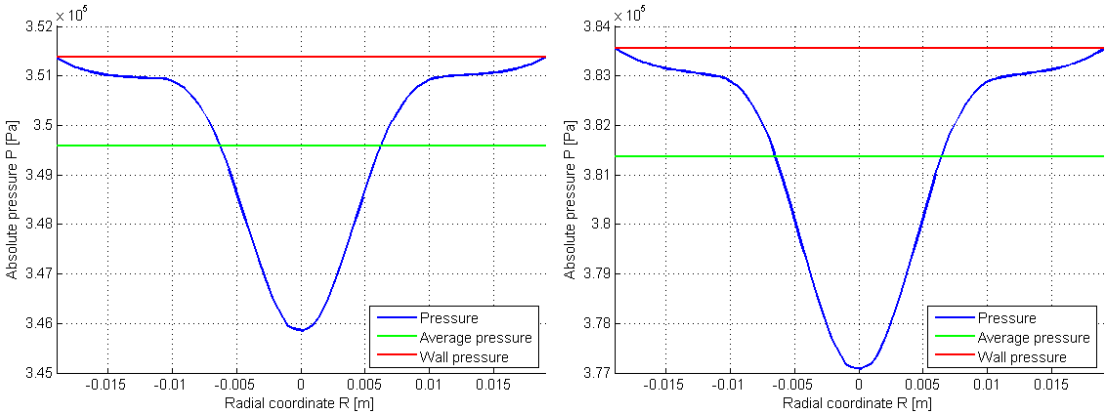

(a) $SN_g = 4.39$ (b) $SN_g = 5.97$

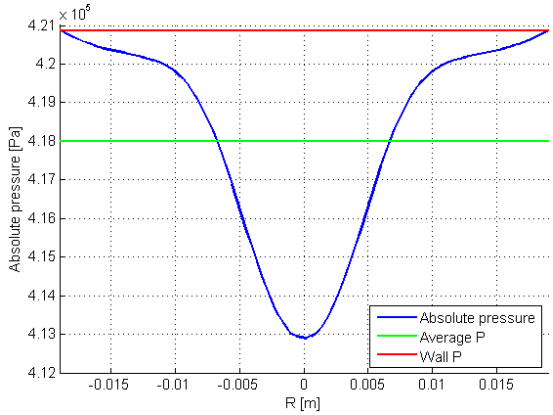

(c) $SN_g = 9.17$

Figure 4.29: Variation of the pressure measures with geometric swirl number (variable is computed over a diametric line at post-combustion chamber)

Table 4.5: Variation of the pressure measures with geometric swirl number

Case	P_{ave} [Pa]	P_w [Pa]	Δ [%]
$SN_g = 4.39$	349586	351381	0.51
$SN_g = 5.97$	381365	383553	0.57
$SN_g = 9.17$	417986	420848	0.68

The made error increases with the geometric swirl number because, remembering equations (4.10) that describe the centrifugal effect caused by the oxidizer swirl injection, the radial pressure gradient becomes greater with the enhancement of the angular velocity of the flow.

4.3.2 Torque around Motor Axis

One of the possible problems of the swirling oxidizer injection is a residual torque around the motor axis, that can cause an unwanted spinning of the hybrid rocket. The torque can be approximated as:

$$T_z \approx \dot{m}_o v_\vartheta d_p \tag{4.15}$$

and the oxidizer mass flow rate can be defined using the continuity equation, considering the properties of the flow and of the geometry at the injection point:

$$\dot{m}_o = \varrho_o A_{hol} v_\vartheta \tag{4.16}$$

Substituting this last equation in the first expression of the torque, it is possible to obtain:

$$T_z \approx \frac{\dot{m}_o^2}{\varrho_o} \frac{d_p}{A_{hol}} \tag{4.17}$$

that, remembering the definition of the oxidizer mass flux (1.28), can be written as:

$$T_z \approx \frac{G_o^2}{\varrho_o} \frac{A_p^2 d_p}{A_{hol}} = \frac{\pi}{4} \frac{G_o^2}{\varrho_o} \frac{d_p^5}{N_{hol} d_{hol}^2} \tag{4.18}$$

The values of the torque applied to the motor axis for the different geometric swirl numbers are plotted in figure 4.30.

The torque applied to the motor axis can now be expressed in terms of the angular acceleration and the motor moment of inertia:

$$T_z = I_{zz} \dot{\omega}_z \tag{4.19}$$

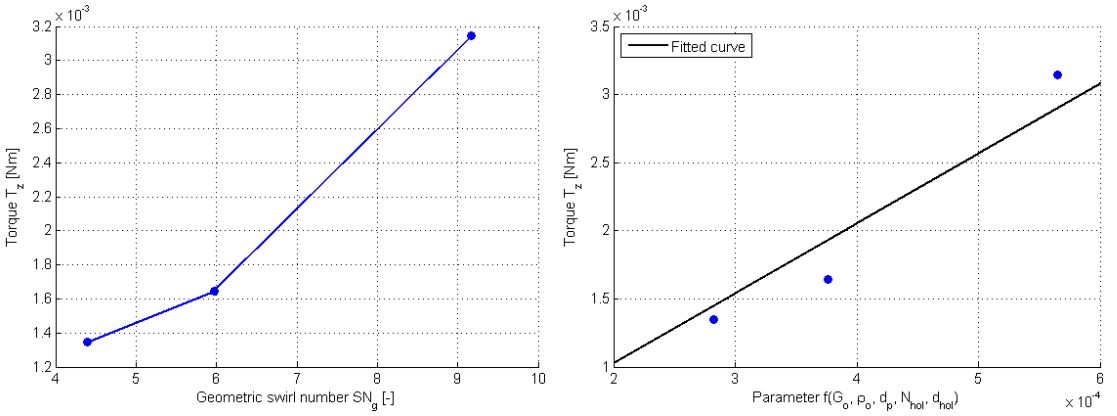

(a) (b)

Figure 4.30: Variation of torque around motor axis with geometric swirl number and parameter of equation (4.18)

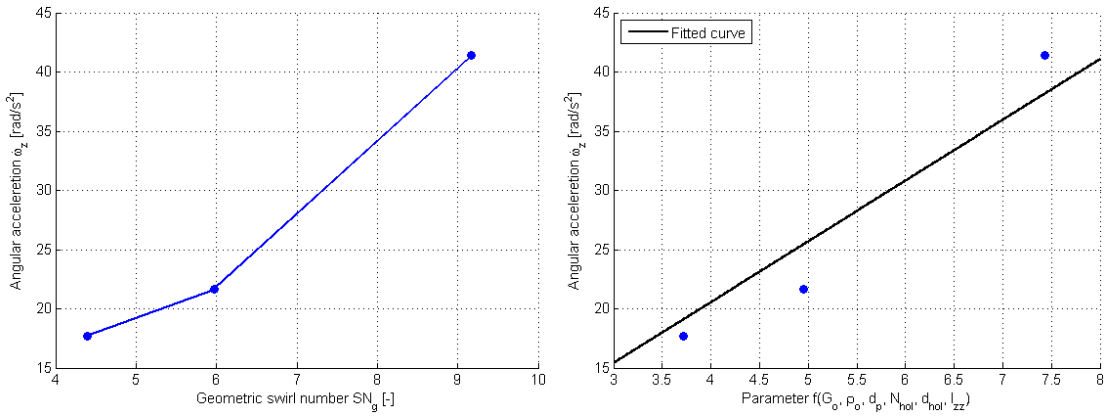

(a) (b)

Figure 4.31: Variation of angular acceleration around the motor axis with geometric swirl number and parameter of equation (4.18)

and substituting equation (4.18):

$$\dot{\omega}_z = \frac{T_z}{I_{zz}} \approx \frac{G_o^2}{\varrho_o} \frac{A_p^2 d_p}{A_{hol}} \frac{1}{I_{zz}} = \frac{\pi}{4} \frac{G_o^2}{\varrho_o} \frac{d_p^5}{N_{hol} d_{hol}^2} \frac{1}{I_{zz}} \tag{4.20}$$

To define the moment of inertia of the motor about its axis, some approximations are necessary:

- The geometry of the motor is approximated as a cylinder and the nozzle is neglected.

- Only the masses of the solid fuel grain and of the oxidizer are considered to compute the moment of inertia.

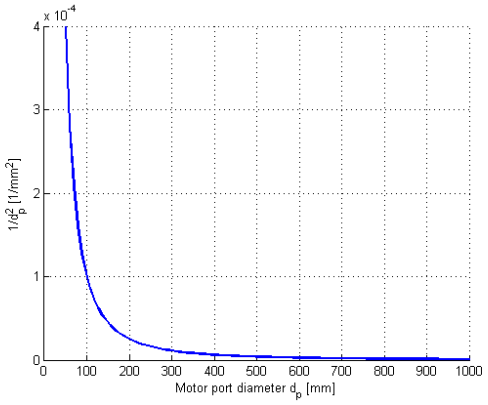

Figure 4.32: Behaviour of equation (4.23)

- The oxygen is stored as liquid phase in a tank of the same diameter of the motor.

- An optimum *O/F* ratio of 2 for oxygen burning with HTPB is used to compute the average oxidizer stored [3].

The moment of inertia can now be defined as:

$$I_{zz} = I_f + I_o = m_f \frac{d_i^2 + d_f^2}{2} + m_o \frac{d_f^2}{2} \approx m_f \frac{(1 + O/F_{opt}) d_f^2 + O/F_{opt} d_i^2}{2} \tag{4.21}$$

As represented in figure 4.31, the angular acceleration for the motor analysed is really high, but this is caused only by its small dimension. It is possible to consider that, for fixed oxidizer mass flux and motor dimensions ratio L/D, all the variables of equation (4.20) scale with the port diameter of the motor as following:

$$A_p d_p^2 \propto d_p^5 \tag{4.22a}$$

$$A_{hol} \propto d_p^2 \tag{4.22b}$$

$$I_{zz} \propto m_f d_p^2 \propto d_p^5 \tag{4.22c}$$

and thus also the angular velocity of the motor scales with the diameter of the circular port of the solid fuel grain:

$$\dot{\omega}_z \propto \frac{1}{d_p^2} \tag{4.23}$$

This basic scaling correlation permits to understand that, with the increase of the motor diameter, the angular acceleration becomes quickly negligible, as can be seen in figure 4.32.

4.4 Scaling of Oxidizer Mass Flux

After analysing the effects of different geometric swirl numbers on the flow field in the combustion chamber of the motor, in this section the consequences of scaling the oxidizer mass flux will be studied. This situation represents the throttling of the motor at different levels. The oxidizer mass fluxes analysed are:

- Oxidizer mass flux 100%
- Oxidizer mass flux 67%
- Oxidizer mass flux 33%

As can be seen in figure 4.33, for a given geometric swirl number, that identifies a specific injector configuration, the scaling of the oxidizer mass flux changes the intensity of the helical flow field in the combustion chamber, because a smaller quantity of oxygen pushed in the motor means lower injection velocities. This differences can also be quantitatively measured by the variation of the swirl number and the swirl angle, that are represented in figure 4.34. It is possible to see that, for a fixed geometric swirl number, the throttling of the motor causes a translation of the curves of these two parameters. As already said for the scaling of the injection swirl number, the scaling of the oxidizer mass flux does not affect the shape of the flow field and of its describing parameters, but it only changes the magnitude of these variables. The temperature in the motor decreases with the oxidizer mass flux, as can be seen in figure 4.35, because a higher quantity of fresh oxidizer reduces the temperature of the hot products of the combustion. Also, the axial velocity decreases only slightly with the increase of the oxidizer mass flux, as represented in figure 4.36, for the variation of the temperature and of the quantity of pyrolyzed fuel, as will be later discussed in the next paragraph. As can be seen in figure 4.37, the tangential velocity component, instead, obviously increases with the oxidizer mass flux, to respect the continuity equation, because the injection area is fixed, whereas the mass of oxygen, pushed into the combustion chamber through the injector holes, is higher.

The oxidizer mass flux is a critical parameter to describe the functioning of a classic hybrid rocket motor, because it regulates the combustion process, and thus the regression mechanism of the solid fuel, as described by the Marxman theory, previously examined in chapter 1:

$$\bar{\dot{r}} = aG_o^n \tag{4.24}$$

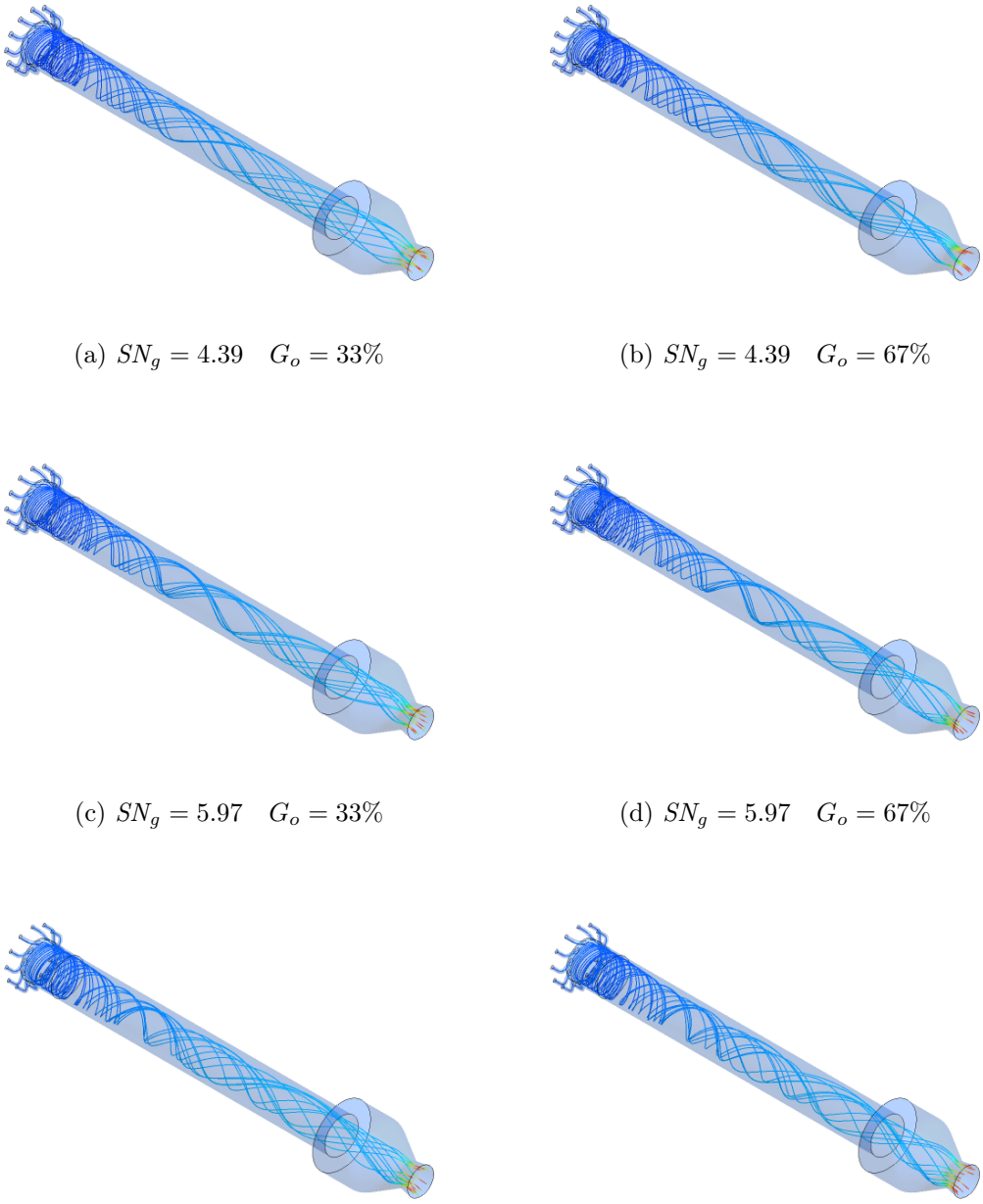

(a) $SN_g = 4.39 \quad G_o = 33\%$

(b) $SN_g = 4.39 \quad G_o = 67\%$

(c) $SN_g = 5.97 \quad G_o = 33\%$

(d) $SN_g = 5.97 \quad G_o = 67\%$

(e) $SN_g = 9.17 \quad G_o = 33\%$

(f) $SN_g = 9.17 \quad G_o = 67\%$

Figure 4.33: Comparison between the streamlines in the motor for all the simulations

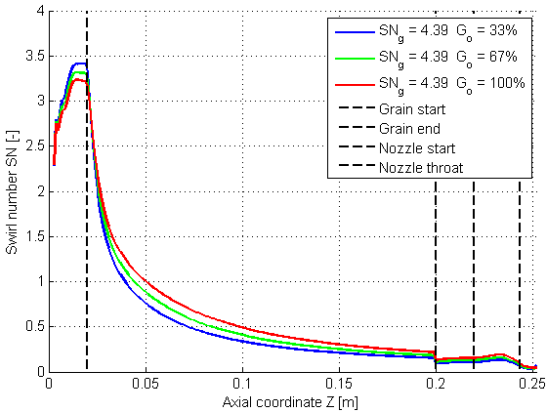

(a) Swirl number for $SN_g = 4.39$

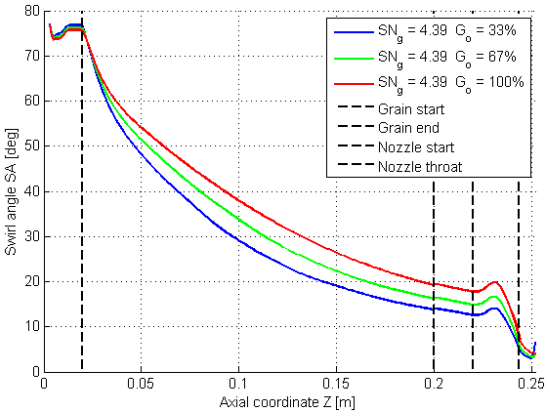

(b) Swirl angle for $SN_g = 4.39$

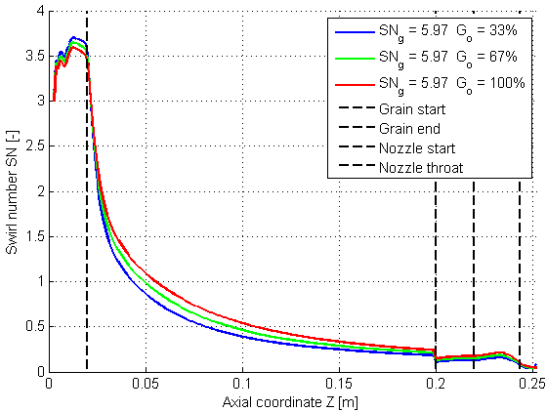

(c) Swirl number for $SN_g = 5.97$

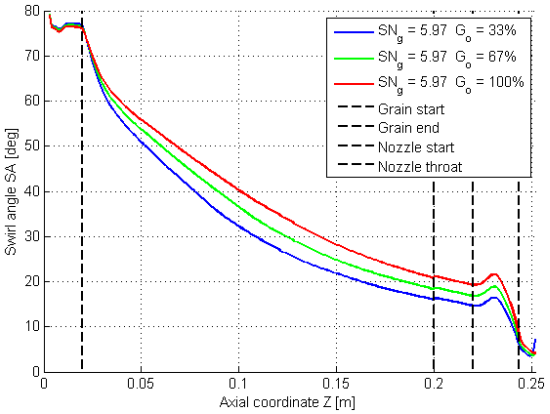

(d) Swirl angle for $SN_g = 5.97$

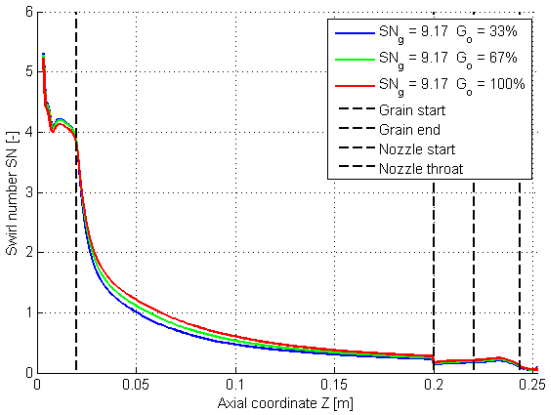

(e) Swirl number for $SN_g = 9.17$

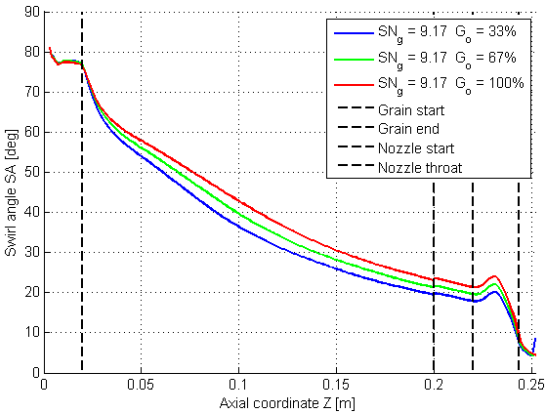

(f) Swirl angle for $SN_g = 9.17$

Figure 4.34: Variation of swirl number and swirl angle along the motor axis

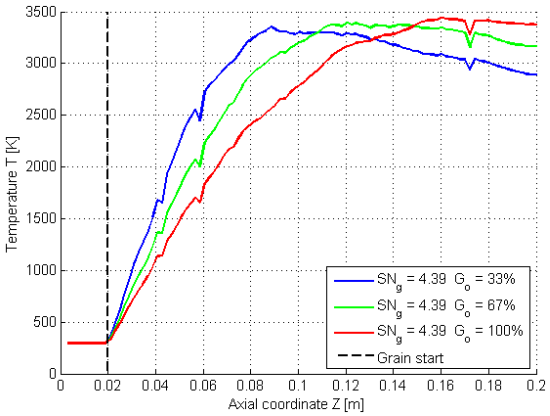

(a) Axial variation for $SN_g = 4.39$

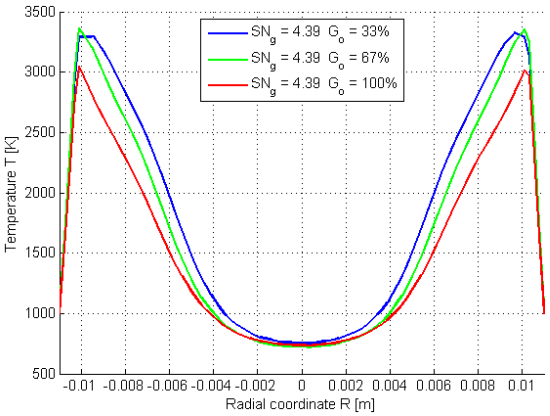

(b) Radial variation for $SN_g = 4.39$

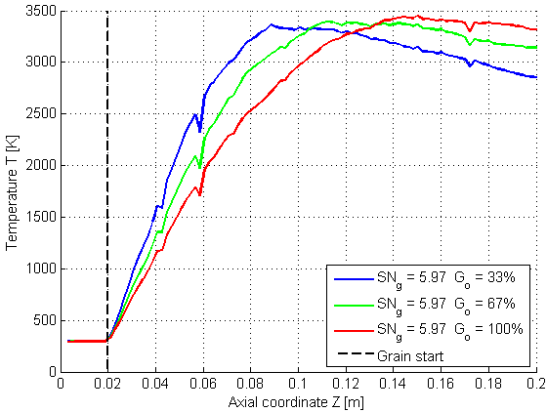

(c) Axial variation for $SN_g = 5.97$

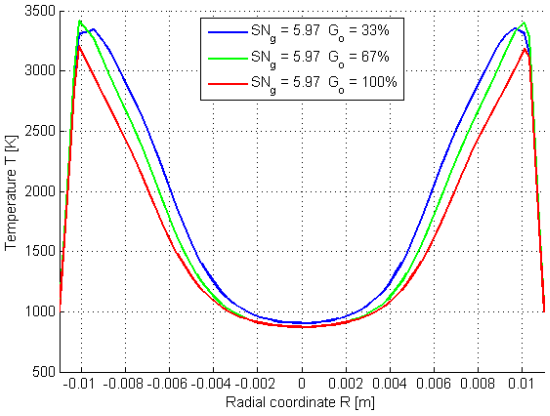

(d) Radial variation for $SN_g = 5.97$

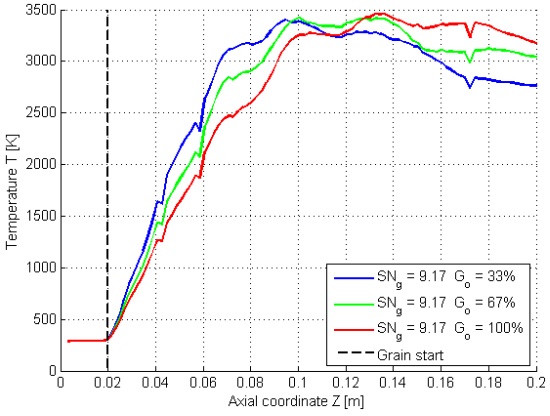

(e) Axial variation for $SN_g = 9.17$

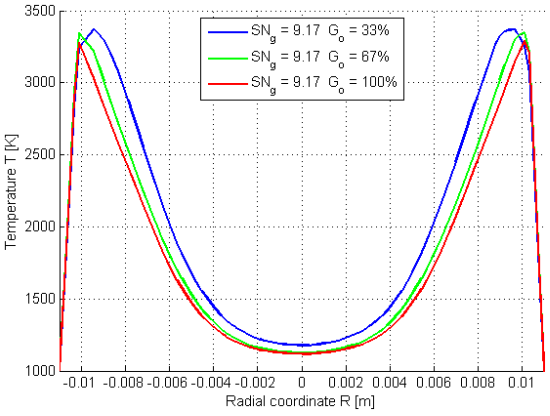

(f) Radial variation for $SN_g = 9.17$

Figure 4.35: Variation of temperature (variable is computed over an axial line 1 mm away from the grain surface and over a diametric line at middle grain)

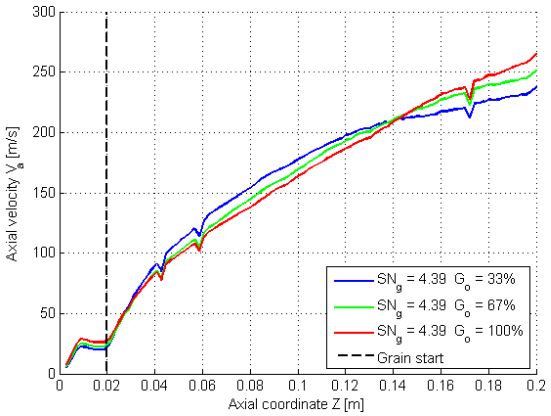

(a) Axial variation for $SN_g = 4.39$

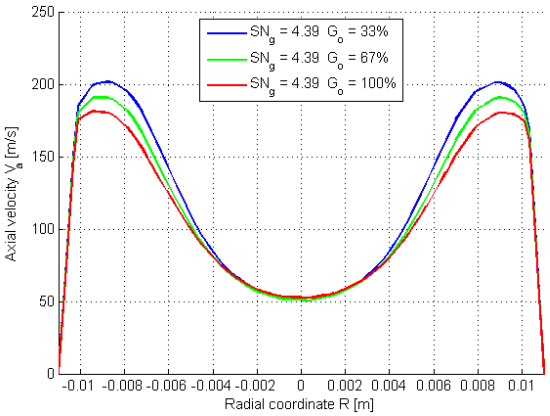

(b) Radial variation for $SN_g = 4.39$

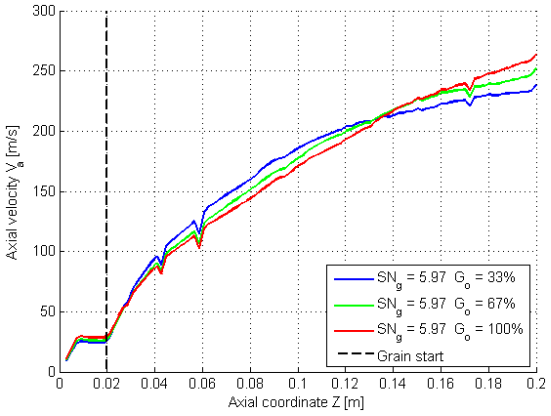

(c) Axial variation for $SN_g = 5.97$

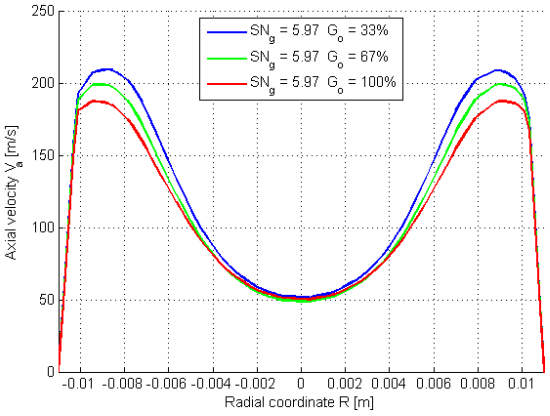

(d) Radial variation for $SN_g = 5.97$

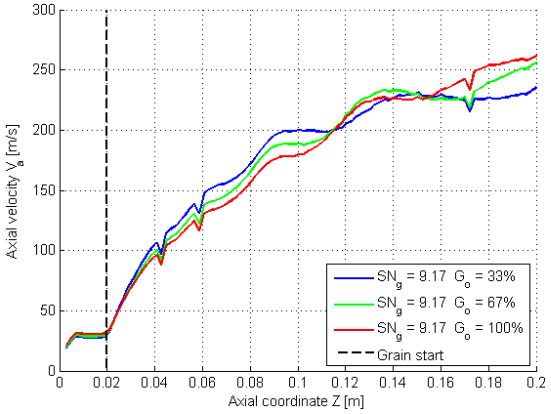

(e) Axial variation for $SN_g = 9.17$

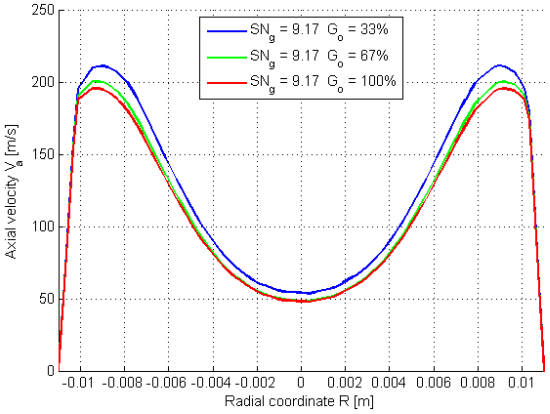

(f) Radial variation for $SN_g = 9.17$

Figure 4.36: Variation of axial velocity (variable is computed over an axial line 1 mm away from the grain surface and over a diametric line at middle grain)

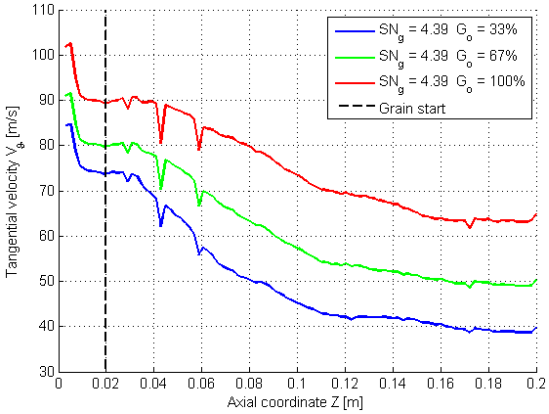

(a) Axial variation for $SN_g = 4.39$

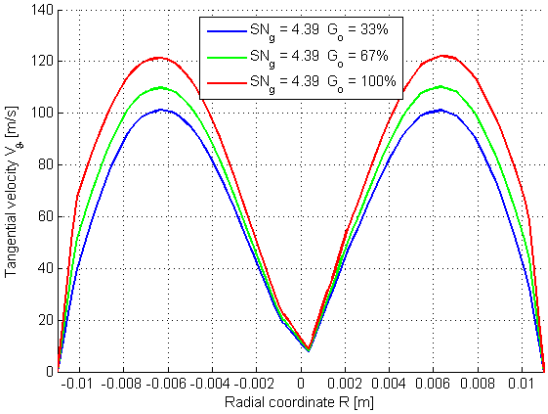

(b) Radial variation for $SN_g = 4.39$

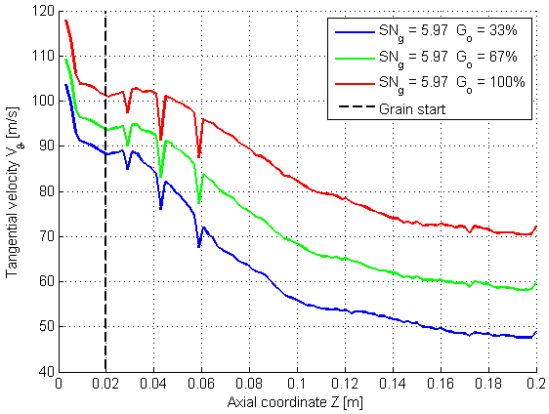

(c) Axial variation for $SN_g = 5.97$

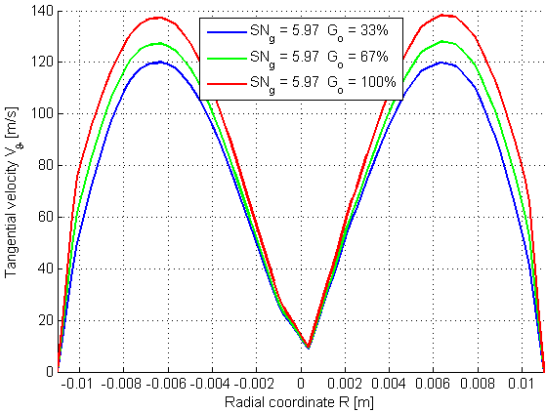

(d) Radial variation for $SN_g = 5.97$

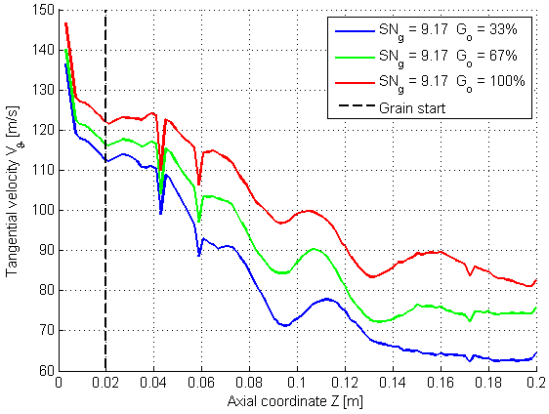

(e) Axial variation for $SN_g = 9.17$

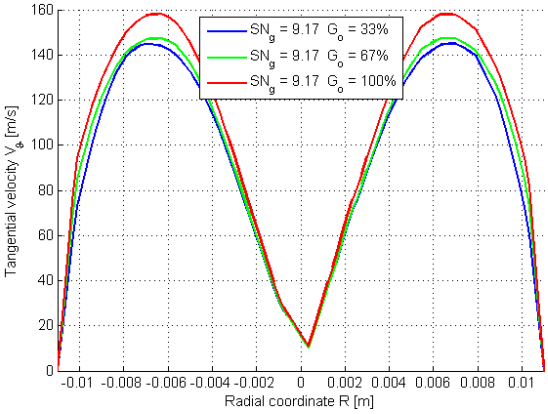

(f) Radial variation for $SN_g = 9.17$

Figure 4.37: Variation of tangential velocity (variable is computed over an axial line 1 mm away from the grain surface and over a diametric line at middle grain)

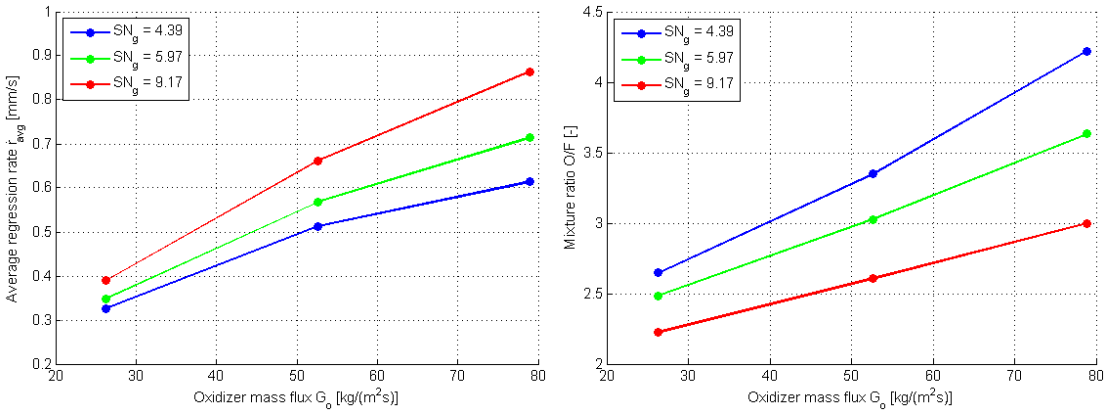

(a) Average regression rate (b) Mixture ratio

Figure 4.38: Variation of average regression rate and mixture ratio with geometric swirl number and oxidizer mass flux

Table 4.6: Variation of average regression rate and mixture ratio with geometric swirl number and oxidizer mass flux

Case		$\bar{\dot{r}}$ [mm/s]	O/F [−]
$SN_g = 4.39$	$G_o = 33\%$	0.327	2.65
$SN_g = 4.39$	$G_o = 67\%$	0.516	3.35
$SN_g = 4.39$	$G_o = 100\%$	0.619	4.22
$SN_g = 5.97$	$G_o = 33\%$	0.348	2.49
$SN_g = 5.97$	$G_o = 67\%$	0.572	3.02
$SN_g = 5.97$	$G_o = 100\%$	0.716	3.63
$SN_g = 9.17$	$G_o = 33\%$	0.388	2.23
$SN_g = 9.17$	$G_o = 67\%$	0.663	2.61
$SN_g = 9.17$	$G_o = 100\%$	0.864	3

This parameter is, obviously, fundamental also for hybrid rocket motors with swirling oxidizer injection. As can be seen in figure 4.38 and table 4.6, the spacial averaged form of the regression rate increases with the oxidizer mass flux, as expected from a system that follows the theory developed by Marxman. However, the mixture ratio experiences an increase of its value with the growing of the oxidizer mass flux. Starting from the results of the numerical simulations, it is possible to obtain a correlation between the regression rate and the oxidizer mass flux, for the different geometric swirl number, with the same form of the law obtained by Marxman:

$$\bar{\dot{r}} = 0.053221 G_o^{0.5631} \qquad SN_g = 4.39 \tag{4.25a}$$

$$\bar{\dot{r}} = 0.04365 G_o^{0.6416} \qquad SN_g = 5.97 \tag{4.25b}$$

$$\bar{\dot{r}} = 0.03835 G_o^{0.7145} \qquad SN_g = 9.17 \tag{4.25c}$$

Table 4.7: Variation of the propulsive performance of the motor with geometric swirl number and oxidizer mass flux

Case		c_1^* [m/s] (4.11a)	c_2^* [m/s] (4.11b)	η_1 [%]	η_2 [%]
$SN_g = 4.39$	$G_o = 33\%$	1555	1548	90.8	90.4
$SN_g = 4.39$	$G_o = 67\%$	1529	1523	92.9	92.6
$SN_g = 4.39$	$G_o = 100\%$	1416	1466	89.7	92.9
$SN_g = 5.97$	$G_o = 33\%$	1566	1563	90.5	90.3
$SN_g = 5.97$	$G_o = 67\%$	1560	1559	93.2	93.2
$SN_g = 5.97$	$G_o = 100\%$	1496	1528	92.3	94.3
$SN_g = 9.17$	$G_o = 33\%$	1560	1586	88.6	90.1
$SN_g = 9.17$	$G_o = 67\%$	1590	1592	92.6	92.7
$SN_g = 9.17$	$G_o = 100\%$	1563	1588	93.3	94.8

Table 4.8: Variation of the pressure measures with geometric swirl number and oxidizer mass flux

Case		P_{ave} [Pa]	P_w [Pa]	Δ [%]
$SN_g = 4.39$	$G_o = 33\%$	142630	142931	0.21
$SN_g = 4.39$	$G_o = 67\%$	264150	264985	0.32
$SN_g = 4.39$	$G_o = 100\%$	349586	351381	0.51
$SN_g = 5.97$	$G_o = 33\%$	146328	146754	0.29
$SN_g = 5.97$	$G_o = 67\%$	276745	277866	0.41
$SN_g = 5.97$	$G_o = 100\%$	381365	383553	0.57
$SN_g = 9.17$	$G_o = 33\%$	151109	151793	0.45
$SN_g = 9.17$	$G_o = 67\%$	294188	295836	0.56
$SN_g = 9.17$	$G_o = 100\%$	417986	420848	0.68

While the multiplicative coefficient a decreases, the exponential coefficient n increases with the geometric swirl number, leading to the increase of the regression rate with the geometric swirl number, as previously described.

4.4.1 Motor Performance

The values of the performances parameters, that is the characteristic velocity and the combustion efficiency, for all the simulations, are represented in figure 4.39 and summarized in table 4.7. The characteristic velocity decreases with the increase of the oxidizer mass flux, but the combustion efficiency follows an opposite trend, because it increases with the increase of the oxidizer mass flux.

Moreover, the measure of the pressure at the wall of the post-combustion chamber leads to an overestimation of the performance of the motor. However, the difference is small, as summarized in table 4.8. The made error increases with the oxidizer mass flux, for a fixed geometric swirl number, because, remembering

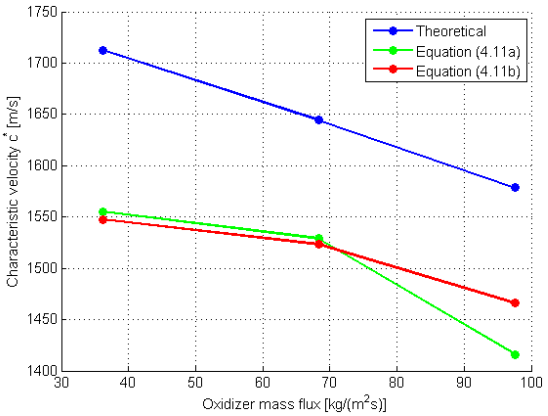

(a) Characteristic velocity for $SN_g = 4.39$

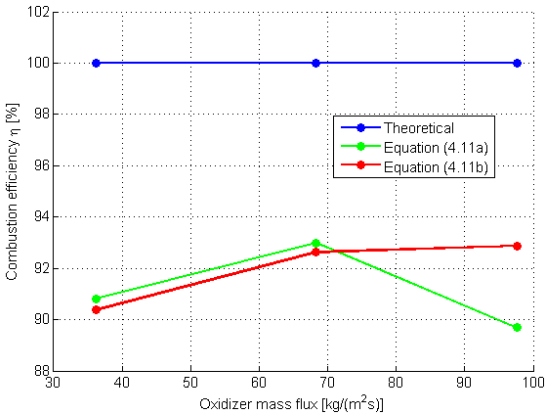

(b) Combustion efficiency for $SN_g = 4.39$

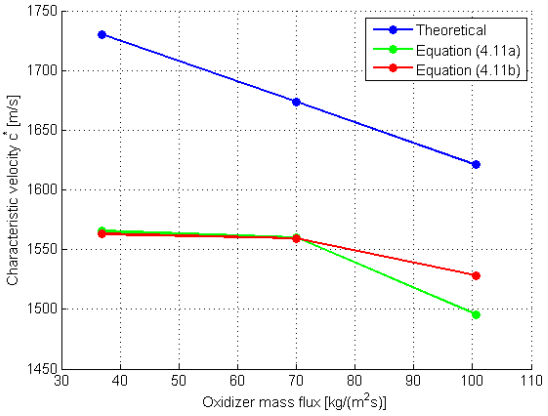

(c) Characteristic velocity for $SN_g = 5.97$

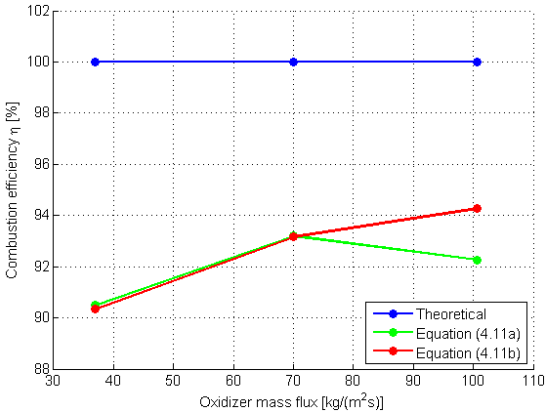

(d) Combustion efficiency for $SN_g = 5.97$

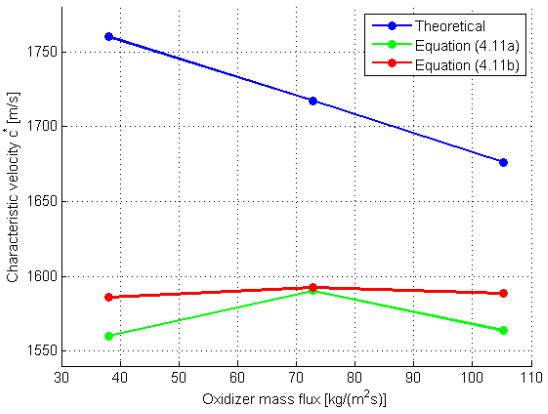

(e) Characteristic velocity for $SN_g = 9.17$

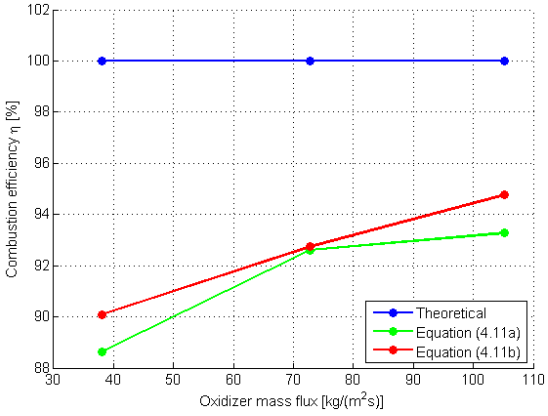

(f) Combustion efficiency for $SN_g = 9.17$

Figure 4.39: Variation of the propulsive performance of the motor with geometric swirl number and oxidizer mass flux

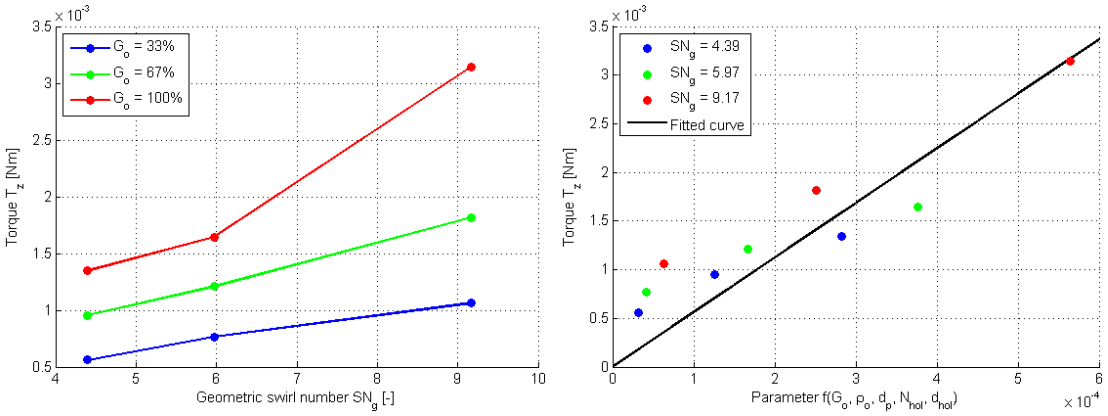

(a) (b)

Figure 4.40: Variation of torque around motor axis with oxidizer mass flux and parameter of equation (4.18)

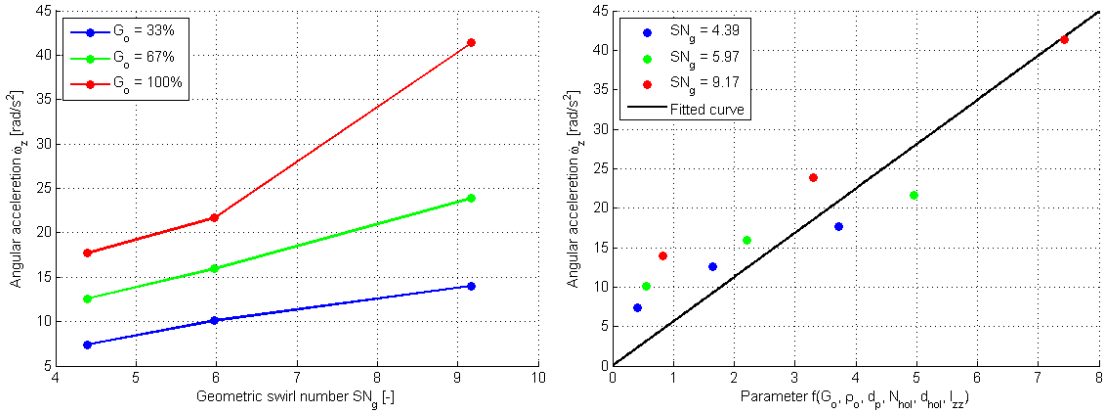

(a) (b)

Figure 4.41: Variation of angular acceleration around the motor axis with oxidizer mass flux and parameter of equation (4.18)

equations (4.10) that describe the centrifugal effect caused by the oxidizer swirl injection, the radial pressure gradient becomes greater with the enhancement of the angular velocity of the flow.

4.4.2 Torque around Motor Axis

As already done for the scaling of the injection swirl number, it is possible to analyse the torque applied to the motor axis, and the consequent angular velocity imparted to the hybrid rocket. As can be seen in figure 4.40 and 4.41, both the parameters increase with the oxidizer mass flux, because the torque applied to the hybrid motor, and thus the angular velocity, is proportional to the oxidizer mass flow rate, since a higher quantity of oxidizer injected in the combustion chamber leads to

a stronger helical flow field. It is possible to see that the expressions (4.18) and (4.20) are giving good results also in this case, confirming that the two equations have been obtained following a correct process, despite the high level of approximation used to reach the solution.

4.5 Discharge coefficient

As theoretically examined by several authors [2, 21, 22, 44], a swirling flow, that has a strong tangential velocity component, through a convergent-divergent nozzle, results in a reduction of the effective throat area. This phenomenon is caused by the centrifugal forces opposing the flow that approaches the nozzle throat. A useful parameter, used to quantify the ratio between the actual mass flow rate through the nozzle throat and the theoretical mass flow rate, is the discharge coefficient, that is defined as follows:

$$c_d = \frac{p_{c_{ax}}}{p_{c_{sw}}} \tag{4.26}$$

For a swirling flow field, the discharge coefficient is directly proportional to the tangential component of the velocity of the flow and inversely proportional to its speed of sound:

$$c_d \propto \frac{v_\vartheta}{a} \tag{4.27}$$

where a is the speed of sound, defined as:

$$a = \sqrt{\gamma R T} \tag{4.28}$$

The discharge coefficient can not be evaluated directly using equation (4.26) and the numerical results of the simulations in which the combustion process happens, because in the swirling case the increment of pressure is caused by two different phenomena:

- The chocking effect of the swirling flow
- A more complete and efficient combustion process, thanks to the higher level of mixing caused by the swirling flow

The discharge coefficient has to include only the increase of the pressure in the combustion chamber due to the first phenomenon listed. Thus, to exclude the increase of the pressure due to the second phenomenon described, three different groups of simulations, for all the geometric swirl numbers considered until now, were carried out:

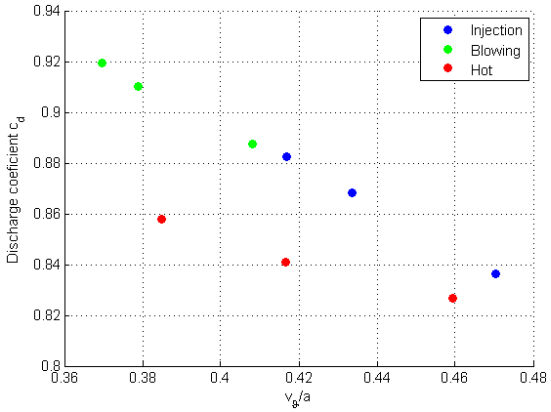

Figure 4.42: Variation of discharge coefficient with parameter v_ϑ/a

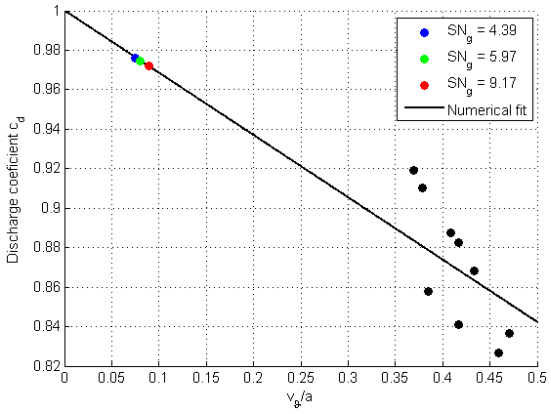

Figure 4.43: Extrapolation of discharge coefficient

1. *Injection*: only the cold oxidizer is injected.

2. *Blowing*: both the cold oxidizer and the cold fuel are considered.

3. *Hot*: both the oxidizer and the fuel are considered, injected at the ideal temperature of combustion.

The same gas, for both the oxidizer and the fuel, was injected, to not consider the variation of the molecular mass of the flow due to the better mixing of the swirling flow, and the same injection temperature was imposed, to avoid a thermal gradient in the radial direction. Afterwards, using the results of all these numerical simulations, the discharge coefficient was evaluated as a pressure ratio between the axial case and the swirling one, and correlated to the parameter v_ϑ/a, as can be seen in figure 4.42.

Using the numerical correlation obtained with the process explained, it is possible to evaluate the discharge coefficient for the *combustion* simulations, only calculating the parameter v_ϑ/a for each specific case, as represented in figure 4.43, in such a way that only the increase of pressure due to the centrifugal forces is considered.

The resulting discharge coefficients of the nozzle, for all the considered geometric swirl numbers, are:

- $SN_g = 4.39 \qquad c_d = 0.976$
- $SN_g = 5.97 \qquad c_d = 0.975$
- $SN_g = 9.17 \qquad c_d = 0.972$

4.6 Regression Rate Law

Following the approach proposed by Yuasa et al. [72], it is possible to introduce a useful parameter, that permits to obtain a correlation to describe the regression rate law. The fuel regression, caused by its pyrolysis, is governed by the oxidizer mass flux flowing in the combustion chamber of the hybrid motor, apart from the region immediately next to the inlet, where the oxidizer wall jet, striking directly onto the solid grain surface, leads to a higher consumption of the fuel. This behaviour is similar to the one that controls the combustion of classic hybrid rocket motors, but if a swirl injector is used, then also the tangential velocity component of the flow must be considered in addition to the axial velocity component. Before introducing the parameter to describe a correlation for the regression rate, it is necessary to define the geometric swirl number with an approximate equation, that is obtained assuming an uniform velocity distribution of the axial oxidizer flow and the conservation of momentum at the injector exit:

$$SN_g = \frac{\text{angular momentum flux}}{\text{axial momentum flux} \cdot \text{radius}} \approx \frac{\dot{m}_o v_{\vartheta_0} r}{\dot{m}_o v_{z_0} r} = \frac{v_{\vartheta_0}}{v_{z_0}} \tag{4.29}$$

where v_{z_0} and v_{ϑ_0} are the axial and tangential velocity components at the injector exit. Assuming conservation of momentum and mass between the oxidizer mass flow at the injector exit and the oxidizer mass flow at a section of the solid grain port, these velocities can be correlated with the axial and tangential velocity components measured along the motor:

$$v_z = v_{z_0} \frac{A_p}{A_0} = v_{z_0} \frac{d_p}{d_0} \tag{4.30a}$$

$$v_\vartheta = v_{\vartheta_0} \frac{A_p}{A_0} = v_{\vartheta_0} \frac{d_p}{d_0} \tag{4.30b}$$

Therefore, the velocity of the swirling flow can be computed summing the rotational component, caused by the particular configuration of the injector that forces the

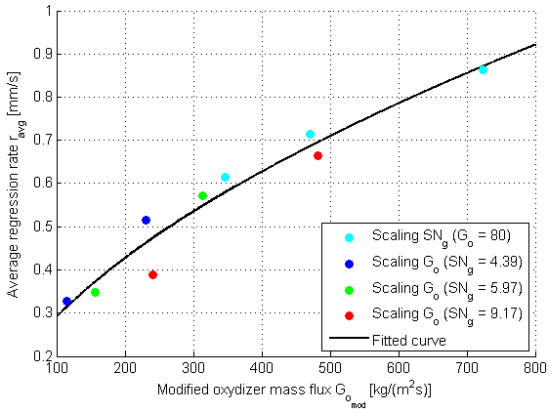

Figure 4.44: Variation of average regression rate with modified oxidizer mass flux

oxidizer mass to enter tangentially the combustion chamber of the hybrid motor, and the axial component:

$$v = \sqrt{v_z^2 + v_\vartheta^2} = v_z \sqrt{1 + \left(\frac{d_p}{d_0} SN_g\right)^2} \tag{4.31}$$

and when $SN_g \gg 1$ this last equation can be approximated as a function of the tangential velocity and of the geometric swirl number:

$$v \approx v_z \frac{d_p}{d_0} SN_g \tag{4.32}$$

Remembering the definition of the oxidizer mass flux (1.28):

$$G_o = \frac{\dot{m}_o}{A_p} \tag{4.33}$$

this equation can be rewritten to include the tangential component of the velocity, introducing the expression of the velocity of the swirling flow (4.32). The definition can be approximate as follows:

$$G_{o_{mod}} \approx \frac{\dot{m}_o}{A_p} \frac{d_p}{d_0} SN_g \tag{4.34}$$

This new parameter permits to introduce a correlation between the regression rate and the oxidizer mass flux, corrected to include the rotational component of the flow, that has a similar shape to the one describing classic hybrid rocket motors:

$$\bar{\dot{r}} = a G_{o_{mod}}^n \tag{4.35}$$

and using the results of the numerical simulations carried out varying the geometric

swirl number and the oxidizer mass flux, the correlation obtained is:

$$\bar{\dot{r}} = 0.02256 G_{o_{mod}}^{0.5551} \tag{4.36}$$

This equation permits to obtain a curve well fitting the results of the regression rate, evaluated from all the numerical simulations conducted, as represented in figure 4.44. The small exponential coefficient n is probably due to the small oxidizer mass fluxes analysed.

It is possible to see that the correlation obtained fits well the regression rates evaluated, and this means that this process, despite of all the approximations introduced to reach a solution, has a valid physical basis. For this reason, this approach could be used to find a regression rate law for hybrid rocket motors with swirling oxidizer injection, provided a wider range of oxidizer mass fluxes analysed.

Chapter 5

Summary and Conclusions

THE study of the behaviour of hybrid rockets with swirling oxidizer injection is necessary, in order to better understand the capability of this promising technology to solve the inherent problems of hybrid motors, that is mainly the low regression rate.

After a brief introduction presenting hybrid rocket motors along with their advantages and disadvantages compared with solid and liquid rockets, in chapter 1 the hybrid combustion process, that is based on the formation of a turbulent boundary layer located over the solid fuel surface, is presented and the Marxman's regression rate theory is analysed, arriving at the regression rate law:

$$\bar{\dot{r}} = aG_o^n L^m \tag{5.1}$$

Moreover, several subsequent corrections, developed to consider the effects of thermal radiation and of chemical kinetics, are briefly described.

In chapter 2 several possible methods to increase the regression rate of hybrid rockets, without reducing their inherent advantages, are presented. International researches are encouraged by the great study of Casillas et al., demonstrating that a three-to-fourfold increase in the regression rate may be satisfactory to develop a really competitive hybrid rocket motor [14]. Four main approaches that have been developed are discussed:

- The introduction of solid additives to the grain
- The use of liquefying solid fuels
- The addition of a diaphragm in the hybrid motor
- The implementation of nonconventional solid fuel grain geometries and unique injector designs

Furthermore, the last approach is studied more in detail, and therefore also the swirling oxidizer injection, analysing several injector configurations used together with both side-burnings and end-burnings grains.

In chapter 3 the numerical investigation, carried out with a commercial 3D steady-state computational fluid dynamics code, is presented, describing the design of the analysed hybrid rocket motor with swirling oxidizer injection, the setup of the numerical simulations and the test matrix followed.

In chapter 4 the results of the numerical simulations conducted are presented and discussed, supporting the analysis with analytical studies and comparing it with data obtained from several references. This chapter is divided in six different sections:

1. Incremental analysis
2. Comparison between axial and swirl injector
3. Scaling of injection swirl number
4. Scaling of oxidizer mass flux
5. Discharge coefficient
6. Regression rate law

In the first section the initial motor geometry is studied, increasing the complexity of the system with the addition of each component one by one, to better understand which are the parameters that influence the swirling flow field inside the combustion chamber. Analysing the Navier-Stokes equations, neglecting the gravity and the normal viscous terms, it has been analytically demonstrated that a forced vortex is imposed to the flow field in the combustion chamber:

$$\omega r = v_\vartheta \tag{5.2}$$

This solution also describes the centrifugal effect caused by the rotation of the flow, that pushes the fluid toward the wall of the combustion chamber. This effect could be described by the pressure gradient in the radial direction:

$$p(r) = p_i \exp\left(\frac{\omega^2 r^2 M_m}{2R_u T}\right) \tag{5.3}$$

The radial pressure gradient was numerically confirmed by the CFD simulations. This is mathematically true only when the oxidizer is injected into the combustion

chamber, whereas the increase of the system complexity causes the results to be far away from the theoretical ones.

The second section contains the comparison between axial and swirl injector. If in the axial configuration the oxidizer and the fuel flow parallel to the flame along the motor port remaining stratified, the swirl injector, that forces the gaseous oxygen to enter the combustion chamber with a strong tangential velocity component and thus leads to the formation of a rotational flow field, enhances the mixing of the reacting chemical species involved in the combustion process. This ensures a more complete and effective burning process, which involves the improvement of the motor performance.

In the third section the scaling of the injection swirl number is analysed. The injector is characterized by a geometric swirl number:

$$SN_g = \frac{(r_{inj} - r_{hol})r_{inj}}{N_{hol}r_{hol}^2} \tag{5.4}$$

Three different injectors, defined by three different geometric swirl numbers, are considered. The increase of the injection swirl number leads to a higher regression rate of the motor and to a better performance of the hybrid motor. Moreover, the resultant torque applied to the motor axis, due to the presence of a helical flow field, is analysed, and an approximated expression of the resultant torque and of the angular velocity of the motor is obtained. The applied torque increases with the injection swirl number, but the angular velocity of the hybrid rocket motor decreases quickly with the motor diameter.

The fourth section discusses the scaling of the oxidizer mass flux. This situation represents the throttling of the motor at different levels. The increase of the oxidizer mass flux leads to a better pyrolysis of the solid fuel grain, as would be expected remembering the regression rate law developed by Marxman, and to a better performance of the hybrid rocket. For each geometric swirl number considered it is possible to obtain a correlation between the regression rate and the oxidizer mass flux, following the form of the Marxman's law. Furthermore, the resultant torque applied to the motor axis increases with the oxidizer mass flux, due to a stronger helical flow field.

As theoretically examined by several authors [2, 21, 22, 44], a swirling flow through a convergent-divergent nozzle results in a reduction of the effective throat area. This phenomenon is caused by the centrifugal forces opposing the flow that approaches the nozzle throat. In the fifth section the discharge coefficient of the nozzle, for the different geometric swirl number considered, is obtained. This parameter quantifies the ratio between the actual mass flow rate through the nozzle

throat and the theoretical mass flow rate, that is defined as follows:

$$c_d = \frac{p_{c_{ax}}}{p_{c_{sw}}} \tag{5.5}$$

In the last section, following the research of Yuasa et al. [72], a correlation between the regression rate and the oxidizer mass flux is obtained, including the geometric swirl number in the expression:

$$\bar{\dot{r}} = aG_{o_{mod}}^{n} \tag{5.6}$$

where the modified oxidizer mass flux is defined as:

$$G_{o_{mod}} \approx \frac{\dot{m}_o}{A_p}\frac{d_p}{d_0}SN_g \tag{5.7}$$

This approach permits to have a single regression rate law for several injection swirl numbers, and thus, different injector configurations. The obtained correlation fits well the regression rates evaluated with the numerical simulations, and this means that this process, despite of all the approximations introduced to reach a solution, has a valid physical basis. For this reason, this approach could be used to find a regression rate law for hybrid rocket motors with swirling oxidizer injection, provided a wider range of oxidizer mass fluxes analysed.

The numerical analysis carried out permits to obtain an overall view of the influencing parameters of an hybrid rocket motor with swirling oxidizer injection. Moreover, it provides a scaling behaviour of the motor, at least from a qualitatively point of view, in relation to the variation of the geometric swirl number and of the oxidizer mass flux. Further work is needed to consider also the scaling of the geometric dimension of the hybrid rocket motor.

Bibliography

[1] A. Abdelhafez and A. K. Gupta. "Propagation of Swirl in Transonic Airflow". In: *45th AIAA/ASME/SAE/ASEE Joint Propulsion Conference and Exhibit* (2009).

[2] A. Abdelhafez and A. K. Gupta. "Swirling Airflow Through a Nozzle: Choking Criteria". In: *Journal of Propulsion and Power* 26.4 (2010), pp. 754–764.

[3] D. Altman and A. Holzman. "Overview and History of Hybrid Rocket Propulsion". In: *Fundamentals of Hybrid Rocket Combustion and Propulsion*. Ed. by Martin J. Chiaverini and Kenneth K. Kuo. Vol. 218. Progress in Astronautics and Aeronautics. American Institute of Aeronautics and Astronautics, 2007.

[4] D. Altman and R. W. Humble. "Hybrid Rocket Propulsion Systems". In: *Space Propulsion Analysis and Design*. Ed. by R. W. Humble, G. N. Henry, and W. J. Larson. Space Technology Series. McGraw-Hill, 1995.

[5] F. Barato. "Numerical and Experimental Investigation of Hybrid Rocket Motors Transient Behavior". PhD thesis. Università degli Studi di Padova, 2013.

[6] F. Barato, M. Faenza, N. Bellomo, M. Lazzarin, A. Bettella, and D. Pavarin. "Numerical Simulations of an H2O2 Vortex Hybrid Rocket Motor". In: *3rd Space Propulsion Conference* (2012).

[7] J. M. Beér and N. A. Chigier. *Combustion Aerodynamic*. Krieger Publishing Company, 1972.

[8] N. Bellomo, F. Barato, M. Faenza, M. Lazzarin, A. Bettella, and D. Pavarin. "Numerical and Expermintal Investigation of Unidirectional Vortex Injection in Hybrid Rocket Engines". In: *Journal of Propulsion and Power* 29.5 (2013), pp. 1097–1113.

[9] N. Bellomo, F. Barato, M. Faenza, M. Lazzarin, A. Bettella, and D. Pavarin. "Numerical and Expermintal Investigation on Vortex Injection in Hybrid Rocket Motors". In: *47th AIAA/ASME/SAE/ASEE Joint Propulsion Conference and Exhibit* (2011).

[10] N. Bellomo, M. Faenza, F. Barato, A. Bettella, and D. Pavarin. "The "Vortex Reloaded" Project: Numerical Investigation on Fully Tangential Vortex Injection in N2O-Paraffin Hybrid Motors". In: *48th AIAA/ASME/SAE/ASEE Joint Propulsion Conference and Exhibit* (2012).

[11] N. Bellomo, M. Faenza, F. Barato, A. Bettella, D. Pavarin, and A. Selmo. "The "Vortex Reloaded" Project: Experimental Investigation on Fully Tangential Vortex Injection in N2O-Paraffin Hybrid Motors". In: *48th AIAA/ASME/SAE/ASEE Joint Propulsion Conference and Exhibit* (2012).

[12] N. Bellomo, M. Lazzarin, F. Barato, and M. Grosse. "Numerical Investigation of the Effect of a Diaphragm on the Performance of a Hybrid Rocket Motor". In: *46th AIAA/ASME/SAE/ASEE Joint Propulsion Conference and Exhibit* (2010).

[13] J. R Caravella, S. D. Heister, and E. J. Wernimont. "Characterization of Fuel Regression in a Radial Flow Hybrid Rocket". In: *Journal of Propulsion and Power* 14.1 (1998), pp. 51–56.

[14] E. D. Casillas, C. W. Shaeffer, and J. C. Trowbridge. "Cost and Performance Payoffs Inherent in Increased Fuel Regression Rates". In: *33rd Joint Propulsion Conference and Exhibit* (1997).

[15] CFD-Online. *K-Omega Models*. URL: `http://www.cfd-online.com/Wiki/K-omega_models`.

[16] CFD-Online. *SST K-Omega Model*. URL: `http://www.cfd-online.com/Wiki/SST_k-omega_model`.

[17] CFD-Online. *Two Equation Turbulence Models*. URL: `http://www.cfd-online.com/Wiki/Two_equation_models`.

[18] M. J. Chiaverini. "Review of Solid-Fuel Regression Rate Behavior in Classical and Nonclassical Hybrid Rocket Motors". In: *Fundamentals of Hybrid Rocket Combustion and Propulsion*. Ed. by M. J. Chiaverini and K. K. Kuo. Vol. 218. Progress in Astronautics and Aeronautics. American Institute of Aeronautics and Astronautics, 2007.

[19] M. J. Chiaverini, K. K. Kuo, A. Peretz, and G. C. Harting. "Regression-Rate and Heat-Transfer Correlations for Hybrid Rocket Combustion". In: *Journal of Propulsion and Power* 17.1 (2001), pp. 99–110.

[20] M. J. Chiaverini, N. Serin, D. K. Johnson, Y.-C. Lu, K. K. Kuo, and G. A. Risha. "Regression Rate Behavior of Hybrid Rocket Solid Fuels". In: *Journal of Propulsion and Power* 16.1 (2000), pp. 125–132.

[21] A. D. Cutler and R. W. Barnwell. “Vortex Flow in a Convergent-Divergent Nozzle”. In: *AIAA Journal* 37.10 (1999), pp. 1329–1331.

[22] A. Gany, M. Mor, and C. Goldman. “Analysis and Characteristics of Chocked Swirling Nozzle Flows”. In: *AIAA Journal* 43.10 (2005), pp. 2177–2181.

[23] S. R. Gomes, L. Rocco Jr., J. A. F. F. Rocco, and K. Iha. “Gaseous Oxygen Injection Effects in Hybrid Labscal Rocket Motor Operations”. In: *46th AIAA/ASME/SAE/ASEE Joint Propulsion Conference and Exhibit* (2010).

[24] M. Grosse. “Effect of a Diaphragm on Performance and Regression of a Laboratory Scale Hybrid Rocket Motor Using Nitrous Oxide and Paraffin”. In: *45th AIAA/ASME/SAE/ASEE Joint Propulsion Conference and Exhibit* (2009).

[25] G. S. Haag, M. N. Sweeting, and G. Richardson. “Low Cost Propulsion Development for Small Satellites at The Surrey Space Centre”. In: *13th AIAA/USU Conference on Small Satellites* (1999).

[26] S. Hikone, S. Maruyama, T. Isiguro, and I. Nakagawa. “Regression Rate Characteristics and Burning Mechanism of Some Hybrid Rocket Fuels”. In: *46th AIAA/ASME/SAE/ASEE Joint Propulsion Conference and Exhibit* (2010).

[27] C.-T. Hsu. “Swirling Nozzle Flow Equations from Crocco’s Relation”. In: *AIAA Journal* 9.9 (1971), pp. 1866–1868.

[28] C.-T. Hsu and A. D. Dejoode. “Inviscid Swirling Flows Through a Choked Nozzle”. In: *AIAA Journal* 11.11 (1973), pp. 1564–1566.

[29] C. C. Jones, D. D. Myre, and J. S. Cowart. “Performance and Analysis of Vortex Oxidizer Injection in a Hybrid Rocket Motor”. In: *45th AIAA/ASME/SAE/ASEE Joint Propulsion Conference and Exhibit* (2009).

[30] M. A. Karabeyoglu, D. Altman, and B. J. Cantwell. “Combustion of Liquefying Hybrid Propellants: Part 1, General Theory”. In: *Journal of Propulsion and Power* 18.3 (2002), pp. 610–620.

[31] M. A. Karabeyoglu and B. J. Cantwell. “Combustion of Liquefying Hybrid Propellants: Part 2, Stability of Liquid Films”. In: *Journal of Propulsion and Power* 18.3 (2002), pp. 621–630.

[32] M. A. Karabeyoglu, B. J. Cantwell, and G. Zilliac. “Development of Scalable Space-Time Averaged Regression Rate Expressions for Hybrid Rockets”. In: *41th AIAA/ASME/SAE/ASEE Joint Propulsion Conference and Exhibit* (2005).

[33] K. Kitagawa, T. Mitsutani, T. Ro, and S. Yuasa. “Effects of Swirling Liquid Oxygen Flow on Combustion of a Hybrid Rocket Engine”. In: *40th AIAA/ASME/SAE/ASEE Joint Propulsion Conference and Exhibit* (2004).

[34] W. H. Knuth, M. J. Chiaverini, D. J. Gramer, and J. A. Sauer. “Experimental Investigation of a Vortex-Driven High-Regression Rate Hybrid Rocket Engine”. In: *34th AIAA/ASME/SAE/ASEE Joint Propulsion Conference and Exhibit* (1998).

[35] W. H. Knuth, M. J. Chiaverini, D. J. Gramer, J. A. Sauer, R. H. Whitesands, and R. A. Dill. “Preliminary Computational Fluid Dynamics Analysis of the Vortex Hybrid Rocket Chamber and Nozzle Flowfield”. In: *34th AIAA/ASME/SAE/ASEE Joint Propulsion Conference and Exhibit* (1998).

[36] W. H. Knuth, M. J. Chiaverini, J. A. Sauer, and D. J. Gramer. “Solid-Fuel Regression Rate Behavior of Vortex Hybrid Rocket Engines”. In: *Journal of Propulsion and Power* 18.3 (2002), pp. 600–609.

[37] W. H. Knuth, D. J. Gramer, M. J. Chiaverini, and J. A. Sauer. “Development and Testing of a Vortex-Driven, High-Regression Rate Hybrid Rocket Engine”. In: *34th AIAA/ASME/SAE/ASEE Joint Propulsion Conference and Exhibit* (1998).

[38] C. P. Kumar and A. Kumar. “Effect of Swirl on the Regression Rate in Hybrid Rocket Motors”. In: *Aerospace Science and Technology* 29.1 (2013), pp. 92–99.

[39] M. Lazzarin, M. Faenza, F. Barato, N. Bellomo, A. Bettella, D. Pavarin, and M. Grosse. “CFD Simulation of a Hybrid Rocket Motor with Liquid Injection”. In: *47th AIAA/ASME/SAE/ASEE Joint Propulsion Conference and Exhibit* (2011).

[40] C. Lee, Y. Na, Y.-C. Hwang, and S.-T. Lee. “Turbulent Flow in the Helical Grain of Hybrid Rocket Fuel”. In: *42th AIAA/ASME/SAE/ASEE Joint Propulsion Conference and Exhibit* (2006).

[41] C. Lee, Y. Na, and G. Lee. “The Enhancement of Regression Rate of Hybrid Rocket Fuel by Helical Grain Configuration and Swirl Flow”. In: *41th AIAA/ASME/SAE/ASEE Joint Propulsion Conference and Exhibit* (2005).

[42] T.-S. Lee and A. Potapkin. “The Performance of a Hybrid Rocket with Swirling GOx Injection”. In: *11th International Conference on Methods of Aerophysical Research* (2002).

[43] W. S. Lewellen, W. J. Burns, and H. J. Strickland. “Transonic Swirling Flow”. In: *AIAA Journal* 7.7 (1969), pp. 1290–1297.

[44] A. Mager. “Approximate Solution of Isentropic Swirling Flow Through a Nozzle”. In: *ARS Journal* 31.8 (1961), pp. 1140–1148.

[45] J. Majdalani. “Vortex Injection Hybrid Rockets”. In: *Fundamentals of Hybrid Rocket Combustion and Propulsion*. Ed. by M. J. Chiaverini and K. K. Kuo. Vol. 218. Progress in Astronautics and Aeronautics. American Institute of Aeronautics and Astronautics, 2007.

[46] G. A. Marxman. “Boundary-Layer Combustion in Propulsion”. In: *Symposium (International) on Combustion* 11.1 (1967), pp. 269–289.

[47] G. A. Marxman. “Combustion in the Turbulent Boundary Layer on a Vaporizing Surface”. In: *Symposium (International) on Combustion* 10.1 (1965), pp. 1337–1349.

[48] G. A. Marxman and M. Gilbert. “Turbulent Boundary Layer Combustion in the Hybrid Rocket”. In: *Symposium (International) on Combustion* 9.1 (1963), pp. 371–383.

[49] G. A. Marxman, C. E. Wooldridge, and R. J. Muzzy. “Fundamentals of Hybrid Boundary Layer Combustion”. In: *Heterogeneous Combustion*. Ed. by H. G. Wolfhard, I. Glassman, and L. Green Jr. Vol. 15. Progress in Astronautics and Aeronautics. 1964.

[50] M. Masugi, T. Ide, S. Yuasa, T. Sakurai, N. Shiraishi, and T. Shimada. “Visualization of Flames in Combustion Chamber of Swirling-Oxidizer-Flow-Type Hybrid Rocket Engines”. In: *46th AIAA/ASME/SAE/ASEE Joint Propulsion Conference and Exhibit* (2010).

[51] F. R. Menter. “Two-Equation Eddy-Viscosity Turbulence Models for Engineering Applications”. In: *AIAA Journal* 32.8 (1994), pp. 1598–1605.

[52] M. Motoe and T. Shimada. “Head-End Injected Swirling Gas Flow in a Chamber”. In: *45th AIAA/ASME/SAE/ASEE Joint Propulsion Conference and Exhibit* (2009).

[53] M. Motoe and T. Shimada. “Large Eddy Simulation of Swirling Combustion Flow in a Modeled Hybrid Rocket with Wall Fuel Blowing”. In: *49th AIAA/ASME/SAE/ASEE Joint Propulsion Conference and Exhibit* (2013).

[54] M. Motoe and T. Shimada. “Validation of Numerical Simulation of Swirling Turbulent Flow for Hybrid Rocket Research”. In: *47th AIAA/ASME/SAE/ASEE Joint Propulsion Conference and Exhibit* (2011).

[55] D. D. Myre, P. Caton, J. S. Cowart, and C. C. Jones. “Exhaust Gas Analysis of a Vortex Oxidizer Injection Hybrid Rocket Motor”. In: *46th AIAA/ASME/SAE/ASEE Joint Propulsion Conference and Exhibit* (2010).

[56] H. Nagata, N. Aikawa, R. Akiba, I. Kudo, K. Ito, and N. Tanatsugu. “Combustion Characteristics of Propellants for Dry Towel Hybrid Rocket Motor”. In: *48th International Astronautical Congress* (1997).

[57] H. Nagata, S. Hagiwara, T. Totani, and T. Uematsu. “Optimal Fuel Grain Design Method for CAMUI Type Hybrid Rocket”. In: *47th AIAA/ASME/SAE/ASEE Joint Propulsion Conference and Exhibit* (2011).

[58] H. Nagata, K. Okada, T. Sanda, R. Akiba, S. Satori, and I. Kudo. “New Fuel Configurations for Advanced Hybrid Rockets”. In: *49th International Astronautical Congress* (1998).

[59] H. Nagata, K. Okada, T. Sanda, T. Kato, R. Akiba, S. Satori, and I. Kudo. “Combustion Characteristics of Fibrous Fuels for Dry Towel Hybrid Motor”. In: *The Journal of Space Technology and Science* 13.1 (1997), pp. 11–16.

[60] D. Pastone. “Approaches to Low Fuel Regression Rate in Hybrid Rocket Engines”. In: *International Journal of Aerospace Engineering* (2012).

[61] E. E. Rice, D. J. Gramer, C.P. St. Clair, and M. J. Chiaverini. “Mars ISRU CO/O2 Rocket Engine Development and Testing”. In: *7th NASA International Microgravity Combustion Symposium* (2003).

[62] G. A. Risha, B. J. Evans, E. Boyer, and K. K. Kuo. “Metals, Energetic Additives, and Special Binders Used in Solid Fuels for Hybrid Rockets”. In: *Fundamentals of Hybrid Rocket Combustion and Propulsion*. Ed. by M. J. Chiaverini and K. K. Kuo. Vol. 218. Progress in Astronautics and Aeronautics. American Institute of Aeronautics and Astronautics, 2007.

[63] D. Saito, S. Yuasa, K. Hirata, T. Sakurai, and N. Shiraishi. “Combustion Characteristics of Paraffin-Fueled Swirling Oxidizer-Flow-Type Hybrid Rocket Engines”. In: *48th AIAA/ASME/SAE/ASEE Joint Propulsion Conference and Exhibit* (2012).

[64] C. Sezaki, M. Sakamoto, K. Hirata, S. Yuasa, T. Sakurai, and N. Shiraishi. “Measurement of Axial-Direction Fuel Regression Rate of Swirling-Oxidizer-Flow-Type Hybrid Rocket Engines”. In: *46th AIAA/ASME/SAE/ASEE Joint Propulsion Conference and Exhibit* (2010).

[65] L. D. Strand, M. D. Jones, R. L. Ray, and N. S. Cohen. "Characterization of Hybrid Rocket Internal Heat Flux and HTPB Fuel Pyrolysis". In: *41th AIAA/ASME/SAE/ASEE Joint Propulsion Conference and Exhibit* (1994).

[66] G. P. Sutton and O. Biblarz. *Rocket Propulsion Elements*. John Wiley and Sons, 2001.

[67] T. Tamura, S. Yuasa, and K. Yamamoto. "Effects of Swirling Oxidizer Flow on Fuel Regression Rate of Hybrid Rockets". In: *35th AIAA/ASME/SAE/ASEE Joint Propulsion Conference and Exhibit* (1999).

[68] N. Wall. "Characterisaion of Multiple Concentric Vortices in Hybrid Rocket Combustion Chambers". PhD thesis. The University of Sheffield, 2013.

[69] E. J. Wernimont and S. D. Heister. "Progress in Hydrogen Peroxide Oxidized Hybrid Rocket Experiments". In: *AIAA Paper* (1996).

[70] R. Wilkinson, K. Hart, R. Day, and I. Coxhill. "Proof-of-Concept Testing of a Sustained Vortex-Flow Configuration for Hybrid Rocket Motors". In: *46th AIAA/ASME/SAE/ASEE Joint Propulsion Conference and Exhibit* (2010).

[71] S. Yuasa, O. Shimada, T. Imamura, T. Tamura, and K. Yamamoto. "A Technique for Improving the Performance of Hybrid Rocket Engines". In: *35th AIAA/ASME/SAE/ASEE Joint Propulsion Conference and Exhibit* (1999).

[72] S. Yuasa, N. Shiraishi, and K. Hirata. "Controlling Parameters for Fuel Regression Rate of Swirling-Oxidizer-Flow-Type Hybrid Rocket Engine". In: *48th AIAA/ASME/SAE/ASEE Joint Propulsion Conference and Exhibit* (2012).

[73] S. Yuasa, K. Yamamoto, H. Hachiya, and K. Kitagawa. "Development of a Small Sounding Hybrid Rocket with a Swirling-Oxidier-Type Engine". In: *35th AIAA/ASME/SAE/ASEE Joint Propulsion Conference and Exhibit* (1999).